LBL-32871
UC-401

Lawrence Berkeley Laboratory
UNIVERSITY OF CALIFORNIA

CHEMICAL SCIENCES DIVISION

High Resolution Photoelectron Spectroscopy and Femtosecond Intramolecular Dynamics Using Supersonic Molecular Beams

B. Niu
(Ph.D. Thesis)

September 1992

| LOAN COPY |
|Circulates |
|for 4 weeks| Bldg. 50 Library.
LBL-32871
Copy 2

Prepared for the U.S. Department of Energy under Contract Number DE-AC03-76SF00098

DISCLAIMER

This document was prepared as an account of work sponsored by the United States Government. While this document is believed to contain correct information, neither the United States Government nor any agency thereof, nor the Regents of the University of California, nor any of their employees, makes any warranty, express or implied, or assumes any legal responsibility for the accuracy, completeness, or usefulness of any information, apparatus, product, or process disclosed, or represents that its use would not infringe privately owned rights. Reference herein to any specific commercial product, process, or service by its trade name, trademark, manufacturer, or otherwise, does not necessarily constitute or imply its endorsement, recommendation, or favoring by the United States Government or any agency thereof, or the Regents of the University of California. The views and opinions of authors expressed herein do not necessarily state or reflect those of the United States Government or any agency thereof or the Regents of the University of California.

LBL-32871
UC-401

High Resolution Photoelectron Spectroscopy and Femtosecond Intramolecular Dynamics Using Supersonic Molecular Beams

Baohua Niu
(Ph.D. Thesis)

Department of Chemistry
University of California

and

Chemical Sciences Division
Lawrence Berkeley Laboratory
University of California
Berkeley, California 94720

September 1992

This work was supported by the Director, Office of Energy Research, Office of Basic Energy Sciences, Chemical Sciences Division, of the U.S. Department of Energy under Contract No. DE-AC03-76SF00098.

High Resolution Photoelectron Spectroscopy and Femtosecond Intramolecular Dynamics Using Supersonic Molecular Beams

Copyright © 1992

by

Baohua Niu

The U.S. Department of Energy has the right to use this thesis
for any purpose whatsoever including the right to reproduce
all or any part thereof

Table of Contents

Abstract.....iii

Dedications.....v

Acknowledgments.....vi

Chapter One: Introduction.....1

A. Photoelectron Spectroscopy and Molecular Electronic Structures.....1

B. Born-Oppenheimer Approximation and Vibronic Coupling.....8

C. Intramolecular Dynamics and Autocorrelation Function.....14

References.....23

Figure Caption.....26

Figures.....27

Chapter Two: Experiment.....28

A. Description of the **MBPES** Machine.....28

B. Maintaining of the **MBPES** Machine.....32

C. Tuning & Calibrating of the **MBPES** Machine.....33

1. Tuning the **MBPES** Machine.....33

2. Calibrating the **MBPES** Machine.....37

D. Experimental Setups.....39

References.....44

Tables.....45

Figure Caption.....46

Figures.....48

Chapter Three: High Resolution Photoelectron Spectroscopy and Femtosecond

Intramolecular Dynamics of H_2CO^+ and D_2CO^+.....52

A. Introduction.....52

B. Experimental.....54

C. Vibronic Coupling and Isotope Effects on Vibronic Coupling.....56

D. The Autocorrelation Function.....59

E. Results & Discussions.....62

1. The Ground, $\tilde{X}\ 1\ ^2B_2$ state of H_2CO^+ and D_2CO^+.....63

2. The Firste Excited, $\tilde{A}\ ^2B_1$ state of H_2CO^+ and D_2CO^+.....65

3. The Second Excited, $\tilde{B}\ ^2A_1$, state of H_2CO^+ and D_2CO^+.....68

4. The $\tilde{C}\ 2\ ^2B_2$, state of H_2CO^+ and D_2CO^+.....70

F. Summary.....72

References.....74

Tables.....78

Figure Caption.....89

Figures.....93

Chapter Four: High Resolution Photoelectron Spectroscopy and Femtosecond

Intramolecular Dynamics of H_2CCO^+ and D_2CCO^+.....111

A. Introduction.....111

B. Experimental.....113

C. Vibronic Coupling and Isotope Effects on Vibronic Coupling.....115

D. The Autocorrelation Function.....118

E. Results & Discussions.....122

1. The Ground $\tilde{X}$ state of H_2CCO^+ and D_2CCO^+.....122

2. The $\tilde{A}$ state of H_2CCO^+ and D_2CCO^+.....125

3. The and $\tilde{B}$ state of H_2CCO^+ and D_2CCO^+.....128

4. The $\tilde{C}$ and $\tilde{D}$ States of H_2CCO^+ and D_2CCO^+.....130

5. The $\tilde{E}$ State of H_2CCO^+ and D_2CCO^+.....132

F. Summary.....133

References.....135

Tables.....138

Figure Caption.....153

Figures.....157

Chapter five: Conclusions, and the Future of High Resolution Photoelectron Spectroscopy.....176

High Resolution Photoelectron Spectroscopy and Femtosecond Intramolecular Dynamics Using Supersonic Molecular Beams

by

Baohua Niu

Abstract

High resolution helium Iα photoelectron spectroscopy of formaldehyde and ketene, and their deuterated compounds, are reported. The combination of a unique double-pass high resolution electron-energy analyzer and effective rotational cooling of the sample by supersonic expansion enable the spectroscopic characteristics of these molecular cations to be determined to a much higher accuracy than previously available. The vibrational autocorrelation functions are calculated from the high-resolution photoelectron spectra. They have shed considerable new light into the mechanism of the ultrafast intramolecular dynamics of the molecular cations studied.

The present study reveals much more vibrational structural detail in the first electronic excited state of formaldehyde cations. The first electronic excited state of formaldehyde cations may have non-planar equilibrium geometry. Strong isotope effects on vibronic (vibrational) coupling are observed in the second electronic excited state of formaldehyde. Vibrational autocorrelation functions are calculated for all four observed electronic states of formaldehyde. The correlation function of the first electronic excited

state of formaldehyde shows a rather slow decay rate on the femtosecond time scale. The ultrafast decay of the formaldehyde cations in the third electronic excited state implies that dissociation and intramolecular processes are the main decay path ways.

The present spectra of the ground states of ketene cations have more fine structure than previously available. The AIEs of the first and the fifth excited states are determined unambiguously to a much higher accuracy. The doublet-like fine structures present in the first excited state of ketene implies the excitation of a 'soft' mode that was not observed before. The vibrational autocorrelation functions are calculated for four of the six observed electronic states. The dynamics of the ground states of the cations are characterized by a wave packet oscillating with small amplitude around the minimum on the upper PES. The decay dynamics of the first and the fifth excited states of ketene are characterized by ultra-fast intramolecular processes like predissociation.

This Dissertation is Dedicated to the Memories of My Mother: XiouLang Zhang

Acknowledgment

Although this dissertation bears my name, there are many people who have made substantial contributions to the research reported. There are people who have gone out of way to extend their warm helping hand to me when I need them most.

First and foremost, I would like to thank my adviser Professor David A. Shirley for his constant support and encouragement during my Berkeley years of study. Dave, you have taught me much more about science, and how to do good science than you realize. I learned a great deal from his profound knowledge and unparalleled scientific insights. He also improved the scientific soundness of this dissertation considerably. Prof. Yuan T. Lee also deserves special thanks. I first got to know him while he was visiting the Institute of Chemistry in Bejing, 1985. I have benefited tremendously from his incredibly broad knowledge about everything ever since. His encouragement and advice during the most difficult times in my research have put me back on track with confidence many times. Professor Howard Shugart of the physics department at the University of California at Berkeley is thanked, he has carefully read the whole thesis and made many valuable suggestions which improved the integrity of this dissertation considerably.

I spent a very enjoyable year with Professor Mark Johnson's group at Yale University. I have learned a great deal about spectroscopy from Mark. Mark, thank you very much for all the troubles you have taken to help me finding a postdoctoral position and everything else you have done for me. Professor Zheng Gu at Sichuan University, Chengdu, China is my scientific mentor. His encouragement and confidence in me have helped me to be brave enough to come to Berkeley for my graduate studies. My high school teacher Minxi Tan is a true mentor for me. His stimulating teaching style and his devotion to science teaching have aroused my interests in science in general and chemistry

in particular. Without his early encouragement and guidance, I would have gone nowhere near where I am now.

Dr. Laisheng Wang got me started in the MBPES machine. We have enjoyed many late nights, very long hours experiments together. It has been a great learning experience for me from the fruitful cooperation. Dr. James E. Pollard, the original designer and builder of the MBPES machine, has helped me enormously in getting the machine back to its best performance. His insight in electron optics and scientific knowledge have helped me overcome many of the difficulties faced me. Dr. Phil Heimann deserves my deep gratitude in many regards, ranging from discussions about science, writing recommendation letters and playing tennis together. I have also enjoyed many helpful discussions with Dr. Alex Schach, who has answered my uncountable numbers of computing questions. Thank you Alex. Mr. Eric Daymo, an undergraduate doing Summer research in the Shirley group in 1991 helped me tremendously to get the formaldehyde experiment started, deserve special thanks. I wish him all the best in his pursuing of an advance degree in Chemistry.

The Shirley group members are like family members to me, always friendly and ready to help. Especially I want to thank Dr. Zahid Hussain, Dr. L. Terminello, Dr. J. Medhurst, Dr. L.Q. Wang, Dr. Y. Zhen, Dr. Tobias Reich, Dr. P. Thalappil, Z.Q. Huang, E. Hudson, T. Huff, E. Moler, S. Kellar and B. Petersen. I want to thank Ms. Tina Peoples for her efforts in keeping the Shirley group running smoothly. She has read the first and second chapters and contributed to the readability of this dissertation. Dr. Harry (Floyd) Davis, J.S. Zhang of Professor Yuan Lee's group, Roger and Ramon of Professor Moore's group are thanked for their unreserved help when I need them. Roger and Ramon have given me many helps in getting the formaldehyde and ketene generation, purification apparatus to work.

The supporting staffs at Lawrence Berkeley Laboratory and on the campus machine shops are thanked for their superior efforts in helping getting the science done in a timely fashion. Among them Joseph 'Joe' Katz from the electronic engineering department deserves much more credits than himself knowing them. He always comes up with ideas to solve the electronic, computer problems and fixes them very quickly 'to save' money for the group. Ed. Voroni of the machine shop helped me in more ways than possible to list here. From finding a right nut to designing new parts, he has always been kind, supportive and helpful in getting my 'fancy' ideas to realities.

My friends here at Berkeley helped me in one way or another for all these years. Among them Mr. Hyman Zipkin and his wife Dr. Xi-Jun Zipkin have always taken me under their arms. They have given me a home away from home where whenever I feel 'depressed' I could go home and forget everything else. The warm home feeling is indescribable in words every time I visit them. Thank you Hy, and thank you Jean.

My deepest gratitude goes to my wife and colleague, Xiaoying, for her love, support and cooperation in many of the long nights she has shared with me in the laboratory trying to finish the experiments on time. Without you, Xiaoying, this thesis would have been impossible to finish today. This thesis is as much yours as mine. I thank my family and my parents in-law for their constant love and encouragement throughout my long 'school' years.

This work was supported by the Director, Office of Energy Research, Office of Basic Energy Science, Chemical Science Division of the U.S. Department of Energy under the Contract No. DE-AC03-76SF00098.

Chapter One: Introduction

A. Photoelectron Spectroscopy

The discoveries of electrons (**J.J. Thomson**, 1897) and of the photoelectric effect (**H.R. Hertz**, 1887) in the late nineteenth century had profound influence on the development of the quantum theory of matter. It is **Einstein**, in his celebrated note of 1905,[1] who first postulated that light radiation itself consists of a beam of corpuscles, the photons, of energy **hν** (**h** is the Plank constant, **ν** the frequency of light) and velocity **c**, and who gave a satisfactory explanation for the photoelectric effect phenomenon in particular. The other solid confirmation of the photon theory of light radiation is the **Compton** effect (**A. Compton**, 1924), [2] which showed that the photon has a momentum equal to **hν/c**.

Photoelectron Spectroscopy involves the measurement of the kinetic energies E_k^v of the photoelectrons ejected by monoenergetic radiation to study the ionization energies E_I^v; the intensities and the angular distributions of these electrons to elucidate information about the electronic structures of molecules and ions; and the ionization process itself. Since its early development in the 1960's, photoelectron spectroscopy has contributed tremendously to our understanding of the electronic structures of matter and the relationship between electronic structure and chemical activities. [3]

In the photoelectric process, the combination of the conservation of energy (as formulated by **Einstein**) and momentum (as formulated by **Compton**) gives the following relationship:

$$h\nu = E_I^v + E_k^v + E_t \qquad (1.1)$$

Here **hν** is the incident photon energy, E_I^v is the electron binding energy, E_k^v is the photoelectron kinetic energy, E_t is the kinetic energy imparted to the ionized matter. The

superscript v denotes that the energies were referred to the vacuum level energy. Rearranging equation (1.1), incorporating the reference vacuum level energy and other non-ideal effects into one term $\mathbf{I_{const}}$, which stands for the **I**nstrumental **const**ant, we get:

$$\mathbf{E_k}(1 + \frac{\mathbf{m_e}}{\mathbf{m_+}}) = \mathbf{h\nu} - \mathbf{E_I} - \mathbf{I_{const}} \qquad (1.2)$$

Where $\mathbf{m_e}$ stands for the rest mass of electron, $\mathbf{m_+}$ stands for the mass of the ionized matter. For most photoelectron spectroscopy studies, the following results hold true:

$$(\frac{\mathbf{m_e}}{\mathbf{m_+}})\,\mathbf{E_k} << \mathbf{E_k} \;\;\&\;\; (\frac{\mathbf{m_e}}{\mathbf{m_+}})\,\mathbf{E_k} << \mathbf{R}$$

Here **R** stands for the instrumental energy resolution. Thus the kinetic energy and momentum are carried mostly by the photoelectrons. We can thus simplify equation (1.2) into:

$$\mathbf{E_k} = \mathbf{h\nu} - \mathbf{E_I} - \mathbf{I_{const}} \qquad (1.3)$$

The constant $\mathbf{I_{const}}$ can be obtained by calibration of the instrument using rare gases, since the ionization energies (**IE**) of the rare gases are known precisely from optical spectroscopy.

In a one-electron molecular orbital theory, according to an approximation known as **Koopmans**' theorem, [2a] (the applications of **Koopmans**' theorem have been discussed in great detail by Richards [2b]) each ionization energy $(\mathbf{E_I})_j$ is equal nearly in magnitude to a molecular orbital energy, ε_j:

$$(\mathbf{E_I})_j \cong -\,\varepsilon_j$$

By measuring the E_k, we can get a good estimate of $(E_I)_j$. That is the energy levels of the occupied molecular orbitals (typically, a one-electron molecular orbital of the **Hartree-Fock** determinant) of the **neutral** molecules can be obtained approximately in experiments with photoelectron spectroscopy.

Beyond this one-electron information about neutral molecules, however, lies a wealth of information concerning structures, spectroscopy, dynamics of the photoions, as well as the dynamics of photoionization process itself. Since most ions other than diatomic ions do not fluorescence, photoelectron spectroscopy has been the primary source of information concerning ion structures and spectroscopic constants. [3,27]

In molecular photoelectron spectroscopy, four types of information are available: line energy, line intensity, line shape and the clustering of lines into a band shape. The discrete spectroscopic states that are used to assign the photoelectron spectrum are related to the direct photoionization process by:

$$\mathbf{M}\,(X, v'', j'') + \mathbf{h\nu} \;\text{--->}\; \mathbf{M}^{+}\,(\tilde{X}, \tilde{A}, \tilde{B}, \tilde{C}, \cdots v', j') + \mathbf{e}^{-} \qquad (1.4)$$

All experiments described in this dissertation were done using supersonic molecular beams. In a supersonic molecular beam experiment the neutral molecule can be assumed to be in its ground electronic, vibrational, and rotational state. Thus the ionization energy spectrum depicts the discrete final states of the photoions with different electronic ($\tilde{X}$, $\tilde{A}$, $\tilde{B}$, $\tilde{C}$, $\cdots$), vibrational, and rotational excitations. The distribution of the ionic final states is determined through the vertical transitions from the ground electronic, vibrational and rotational state of the neutral molecule to the ionic potential surfaces. Due to the limited resolving power of the currently available photoelectron spectrometer, the rotational excitations could only be resolved for the lightest molecule ion H_2^+.[4]

The photoionization event itself can be regarded as instantaneous, occurring on a

time scale $\lesssim 10^{-17}$ second [5] [this can be estimated by using the following argument: the molecule usually has a dimension of a few Å (3Å), the speed of light is ~ 3.0×10^{18} Å/sec, so the photoionization event must occur on a time scale that is ~ $3 / (3.0 \times 10^{18})$ second, and the photoelectron leaves the ion on a time scale of $\tau \approx \mathbf{h} / \mathbf{E_k}$, for typical $\mathbf{E_k}$ ~ a few electron volts (**eV**), $\tau \approx 10^{-16}$ second]. Molecular vibration and rotation on the other hand occur on a time scale between 10^{-12} to 10^{-14} second. This large difference in time scale has its origin from the large difference in the mass between an outgoing photoelectron and the left behind photoion.

This leads to the **Franck–Condon** [6] Principle: *The electronic transition in a molecule takes place so rapidly in comparison to the vibrational and rotational motion that immediately afterwards, the nuclei still have very nearly the same relative position and velocity as before the transition.* [7] In quantum mechanics language, the **Franck–Condon** Principle states: *The intensity of a vibrational band in an electronically allowed transition is proportional to the absolute square of the overlap integral of the vibrational wavefunctions of the initial and final states.* [8] The vibrational wavefunction overlap integral is called the **Franck–Condon** Factor (**FCF**).

The direct photoionization process thus can only populate the **Franck–Condon** regions of the ionic potential energy surfaces (**PES**), but these regions, usually, extend over several eV, and encompass many vibrational levels of the photoion in a particular electronic state. The shapes of the photoelectron spectrum can provide essential information concerning: the type of orbitals from which the photoelectron is being ejected; the nature of the ionic **PES** populated; and the dynamics of the photoion intramolecular process. This is illustrated in figure 1 for a typical diatomic molecule **AB** in its ground electronic and vibrational state, and $\mathbf{AB^+}$ in its various electronic and vibrational states. The overall band shapes in the corresponding photoelectron spectra are depicted on the left

side of the figure.

PES x represents the ground state of the ion that has the same nuclear configuration as in the neutral ground state. Such a configuration invariance is produced by ejection of an essentially non-bonding electron. The resulting photoelectron spectrum shows a very intense $v' = 0 \leftarrow v'' = 0$ band (this is called the adiabatic ionization energy, **AIE**) followed by a relatively short progression. Not all molecular ions in their ground states are populated by ejection of non-bonding electrons. Nonetheless, it is very common.

PES a represents an ionic **PES** in which the ion has a different nuclear configuration (in this case the internuclear distance **r** is longer in the ionic state than in the neutral ground state, and usually the photoelectron is ejected from a strong bonding molecular orbital). The corresponding photoelectron band shows a long vibrational progression, and the **FCF** maximum (this is the vertical ionization energy **VIE**) appears near the middle of the progression.

In **PES b**, the **Franck - Condon** region extends both above and below the dissociation energy limit of the ion. The photoelectron band consists of a progression that converges into a continuum. The onset of the continuum corresponds to the mass spectrometric appearance energies (potentials) of the dissociating fragments.

The transition from the neutral ground state to the photoion state represented by **PES c** produces an ion in its dissociating region of the **PES**. The photoelectron band observed is a broad featureless one. However the width of the photoelectron band can give information about the slope of the repulsive region of the **PES** of the ion.

The **PES** depicted by curve **d** represents the crossing or close overlapping of a repulsive **PES** and a bound **PES**. If the total wavefunctions of these two approaching curves do not have the same symmetry, the wavefunctions that describe these states become mixed, and they cannot be separated in the **Franck–Condon** region. The photoion is subject to the lifetime limitation of the repulsive state; this causes

predissociation. The resulting photoelectron band shows discrete vibrational structures at the very beginning: that is the character of the bound ionic-state vibration in the region below the crossing energy level. Lifetime broadened vibrational structure, according to the **Heisenberg** Uncertainty **Principle**, [9] appears in the region of the crossing (this also causes the electronic predissociation). Depending on the nature of the crossing point, there are two possibilities above the crossing energy level. If the "upper" repulsive state is a very steep and close-lying one, a broad featureless continuum appears in the region above the crossing energy level that bears the character of the repulsive ionic state potential energy surface. If, on the other hand, the repulsive state is relatively further away from the **Franck–Condon** region, we will again see a resolved vibrational progression which is the continuation of the progression below the crossing energy level.

This example shows that from the photoelectron band shape and simple **Franck–Condon** analysis, we can deduce useful information about the photoions' structure, spectroscopy, and dynamics. The **FCF** calculations, however, can only be carried out to a fairly satisfactory answer for diatomic molecules. For polyatomic molecules, the **Franck–Condon** factor calculations are feasible only when there are no strongly coupled vibrational modes. It's only recently that polyatomic molecule **Franck–Condon** analysis has been carried out for very simple molecules like SO_2^+, NH_3^+. [10] In the case of formaldehyde, even for the ground ionic state, the **Franck–Condon** analysis was not satisfactory. [10] The **FCF** calculations, up to now, have been confined to the harmonic approximation to treat vibrational wavefunctions. [11-13] We know that even for diatomic molecules the harmonic approximation is good only at very low levels of vibrational excitations. We have to rely heavily on the direct experimental determination of these properties in place of the **Franck–Condon** analysis results. In case of strong vibronic coupling, the **FCF** analysis alone can not give the correct assignment for the spectra obtained. The vibronic coupling effects will be covered briefly in section **B** of this chapter.

To interpret the photoelectron spectrum obtained, one can use the selection rules based on the **Born–Oppenheimer** approximation [17] (which enables us to treat the electronic and nuclei parts of molecular motions separately), the dipole approximation (for electronic transition) and the harmonic (for vibrational transition) approximation to rule out those inactive vibrational modes. For the details of the selection rules involved in photoelectron spectroscopy, Reference 8 is recommended. Here, only the vibrational selection rules, which are based on the harmonic approximation and are the most important ones for this dissertation, are discussed briefly.

Since the neutral molecule in a supersonic molecular beam is in its vibrational ground state, which is totally symmetric in the molecular symmetry group. Under the harmonic approximation, only the totally symmetric vibrational modes can have non-zero **Franck–Condon** factors and can be excited to any quanta (even or odd) upon photoionization. Those non-totally symmetric vibrational modes could only be excited with an even number of quanta with non-zero **FCFs**. But in the case of degenerate vibrations, non-totally symmetric modes could also be excited with an odd number of quanta.

Three factors have to be considered in an attempt to assign the vibrational features observed in the photoelectron spectrum. The first is the anharmonicity of the vibration, which can cause strong mixing of different vibrational modes, and for anharmonic vibrations the selection rules based on harmonic approximation do not necessarily hold on all occasions. Anharmonicity also causes vibrational predissociation. The second factor is that upon ionization many molecular ions produced in a particular electronic state may have a different equilibrium geometry than the neutral molecule in its ground state. This causes some non-totally symmetric (in the neutral molecule) vibrational modes to be excited. The modes that can be excited depend strongly on the differences between the molecule and ion equilibrium geometry in the particular electronic states involved. The third is the aforementioned vibronic coupling effects that have been shown to have great influence on

the vibrational. structures obtained from photoelectron spectroscopy. [18-22]

The correlations between molecular electronic structure and molecular geometry have been the subject of many studies ever since the very beginning of modern quantum chemistry. The most successful one was introduced by **R.S. Mulliken** [14] and further developed by **A.D. Walsh** [15] (generally called **Walsh** diagram) that correlates the molecular orbital energy to some geometric changes in the molecule frame. There are modern ***ab initial*** **SCF**(self-consistent-field) calculations that showed the validity of the original **Walsh** diagram. [16] For the details of constructing a **Walsh** diagram and its interpretations, reference 15 and 16 are recommended. This **Walsh** diagram approach is used in Chapter 3 to explain the possibility of the non-planar equilibrium geometry of H_2CO^+ and D_2CO^+ in their ground and first excited electronic states.

B. Born–Oppenheimer (BO) Approximation and Vibronic Coupling

In the preceding section, we mentioned the **Born–Oppenheimer (BO)** approximation [17] which forms the base of our **Franck–Condon** factor analysis and selections rules. The **BO** approximation is also known as the adiabatic approximation.

The **BO** approximation and its limitations can be seen by examining the Schrödinger equation of a diatomic molecule:

$$\left[\frac{1}{m} \sum_i (\nabla^2_{q_i}) + \sum_k \frac{1}{M_k} (\nabla^2_{q_k}) + \frac{8\pi^2}{h^2} (E-V) \right] \Psi = 0 \qquad (1.5)$$

where q_i are the coordinates of the electrons with mass m and q_k are the coordinates of the nuclei with mass M_k. Suppose the total wavefunction can be written as:

$$\Psi = \Psi_e(q_i) \cdot \Psi_{vr}(q_k) \qquad (1.6)$$

Equation (1.6) is the **BO** approximation, where Ψ_e and Ψ_{vr} are the solutions for the equations:

$$\left[\sum_i (\nabla^2_{q_i}) + (\frac{8\pi^2 m}{h^2})(E^{el} - V_e) \right] \Psi_e = 0 \tag{1.7}$$

$$\left[\sum_k \frac{1}{M_k} (\nabla^2_{q_k}) + (\frac{8\pi^2}{h^2}) \cdot (E - E^{el} - V_n) \right] \Psi_{vr} = 0 \tag{1.8}$$

respectively. Equation (1.7) is the Schrödinger equation of the electrons moving in the field of the fixed nuclei frame and having a potential of $V_e(q_i)$. For each different internuclear distance, V_e is different. Therefore both Ψ_e and E^{el} depend on the internuclear distance as a parameter. Equation (1.8) is the Schrödinger equation of the nuclei moving under the action of the potential $E^{el} + V_n$, where V_n is the Coulomb potential of the nuclei.

Let us substitute equation (1.6) into equation (1.5) and use the conditions set by equation (1.7) and (1.8). We can see that equation (1.5) is satisfied only when:

$$\sum_k \left[\frac{1}{M_k} (\frac{\partial \Psi_e \partial \Psi_{vr}}{\partial^2 q_k}) + \Psi_{vr} (\frac{\partial^2}{\partial^2 q_k}) \Psi_e \right] \tag{1.9}$$

is small and can be neglected. That is to say that the variation of Ψ_e with internuclear distance is sufficient slow so that its first and second derivatives can be neglected. We can estimate their magnitude in the following way. Notice that $h\nabla q_k \Psi_e$ is of the same order as $h\nabla q_i \Psi_e$ since the derivatives operate over approximately the same molecular dimensions. $h\nabla q_i \Psi_e$ is just the momentum of the electrons, therefore we have:

$$\frac{\hbar^2}{2M_k} (\frac{\partial^2}{\partial^2 q_k}) \Psi_e \approx \frac{P_e{}^2}{2M_k} = \frac{m}{M} \frac{P_e^2}{2m} = \frac{m}{M} E_e \tag{1.10}$$

Thus, the contribution from (1.9) is of the same magnitude of the electron energy itself times the ratio of electron mass to molecular mass. Even for the lightest diatomic molecule H_2, we have $m/M \approx 10^{-4}$. For most molecules $m/M \lesssim 10^{-5}$ and with typical electron energy in the molecules on the order of ~ 10 eV, this contributes to the electronic energies on the order of $\lesssim 0.1$ meV. Another more physical way of looking at this is to recognize that $\partial\Psi_e/\partial q_k$ just measures the variation of the electronic wave functions with the nuclear displacements. As long as this variation is small compared with the momentum of the electrons, the **BO** approximation expressed by equation (1.6) is valid.

In equation (1.6) Ψ_{vr} is the wave function of a vibrating rotator. To a good approximation it can be expressed as:

$$\Psi_{vr} = \left(\frac{1}{r}\right)\Psi_v \cdot \Psi_r \tag{1.11}$$

where Ψ_v is the pure vibrational wave function that depends only on the changes of internuclear distance r, Ψ_r is the rotational wave function depends only on the orientation of the molecule in space. Thus to a first order of approximation, the total wave function of the molecule is:

$$\Psi = \Psi_e \cdot \left(\frac{1}{r}\right) \cdot \Psi_v \cdot \Psi_r \tag{1.12}$$

This has been shown by Kronig [21] to hold to a good approximation even when the electron spin and magnetic interaction of angular momentum are included.

From the above discussion, we can see that the **BO** or adiabatic approximation represents one of the fundamental starting point of molecular physics and chemistry. It allows the calculation of molecular properties to be divided into two separable parts which

are much easier to deal with than the original Schrödinger equation (1.5).

In the first part, the electronic wavefunctions are solved keeping the atomic nuclei fixed in space using the Schrödinger equation (1.7). The calculations of electronic structures and wavefunctions for fixed nuclei have been developed to a very high degree of sophistication.

In the second part, the nuclear motion, vibration and rotation can be treated on a given electronic **PES** using Schrödinger equation (1.8). The vibrational and rotational motions could be further separated using approximation (1.11). The calculation of vibrational and rotational wavefunctions have been constantly pursued to perfection for almost all the molecular systems since the very beginning of molecular physics and chemistry.

We can also see from the above discussion of the **BO** approximation what are the limitations of this approximation. First, if the variation of Ψ_e with internuclear distance is fast so its first or second derivatives with respect to the internuclear distance in equation (1.9) is large and can not be neglected, the **BO** approximation (1.6) is not valid. This often happens for molecules with degenerate or close-lying electronic states, where very little change in the nuclear configuration causes the energy level to be shifted a lot. Second, if the vibrational and electronic motions of the molecules are strongly coupled, that is to say that the **Vibronic** effects or coupling is strong, we can no longer separate the electronic and nuclear motions, the **BO** approximation is not valid. This happens more often than not for highly excited states of molecules. One important consequence of vibronic coupling is the non adiabatic behavior of the nuclear motion they induce; that is to say that the nuclear motion ceases to be confined to a single **PES**. A lot of very important dynamic processes, such as electronic predissociation and radiationless transition, can only be explained by invoking the vibronic coupling effects.

In general, we can treat the vibronic effect as a perturbations to the **B O**

approximation, the adiabatic Hamiltonian $\mathcal{H}_0$. Although additional perturbations such as vibration–rotation coupling, rotational–electronic coupling (also called **Coriolis** coupling) and **Fermi** resonances might also occur in the molecules we study, they are usually not strong enough to have significant effects on the vibrational structures of the photoelectron spectra obtained. The most prominent effects of vibronic coupling on photoelectron spectroscopy that we have observed are the following:

(i) Vibrational progressions in modes that are not allowed by selection rules base on the **BO** and harmonic approximations.

(ii) Very low vibrational frequencies

(iii) Different vibrational progressions in the same electronic state for the isotope substituted compound

There are many excellent discussions in the literature about vibronic coupling and its effects on spectroscopy. [18-24] Only a very brief discussion based on perturbation theory is given here.[25] We assume that the corrections caused by vibronic coupling are small in the sense that perturbation theory still can be used. The molecular Hamiltonian $\mathcal{H}$ can be expanded in a Taylor series in the nuclear coordinates Q, the normal coordinates of nuclear vibrations, near the equilibrium configuration Q_0:

$$\mathcal{H} = \mathcal{H}(q;Q)_{Q_0} + \sum_{r=1}^{\infty} \left| \frac{1}{r!} \frac{\partial^r \mathcal{H}(q;Q)}{\partial Q^r} \right|_{Q_0} Q^r + \cdots \tag{1.13}$$

with corresponding corrections to the energy

$$\mathbf{E} = \mathbf{E}_0 + \mathbf{E}_1 + \mathbf{E}_2 + \ldots \tag{1.14}$$

and corrections to the electronic wavefunctions

$$\Psi_e = \Psi_e^0 + \Psi_e^1 + \Psi_e^2 + \ldots \tag{1.15}$$

The first term in equation (1.13) is the **BO** approximation Hamiltonian $\mathcal{H}_0$. Vibronic couplings can be classified as **Linear** coupling and **Quadratic** coupling. Linear coupling refers to the term in $\mathcal{H}$ that is proportional to the nuclear vibration normal coordinates Q_r $\mathcal{H}_1 = \frac{\partial \mathcal{H}}{\partial Q_r}$; similarly for Quadratic coupling $\mathcal{H}_2 \propto Q^2$. Linear coupling is also called **Jahn–Teller** (**JT**) coupling if the coupled electronic states are degenerate by symmetry, and **pseudo–Jahn–Teller** (**pJT**) coupling or **Herzberg–Teller** intensity borrowing in all other cases. Quadratic coupling in linear molecules is called **Renner–Teller** coupling. **JT** coupling is further classified as **dynamic**, if the degenerate electronic states keeps its symmetry near the perturbed equilibrium geometry; or **static**, if the coupling is so strong that the molecule equilibrium geometry is changed to a lower symmetry thus lift the degeneracy of the initial electronic states.

Since both the Linear and Quadratic vibronic coupling depends on the mass weighted nuclear displacements (normal coordinates) as parameters, it is expected that the couplings are different for isotope substitute compounds in the same electronic state. One consequence of this effect is that it is possible that different vibrational modes can be excited for different isotope substituted compounds. Theoretical calculations have shown that this effect does appear in the isotope substitute compound. [26] We have observed this effect in the H_2CO^+ and D_2CO^+ in both the first and second excited states.

C. Intramolecular Dynamics and the Autocorrelation Function

The photoelectric process is a dynamic one. Under the **BO** approximation and the **Franck–Condon** principle, we can populate a wide range of the ionic **PES** that was not easy to reach by other means of excitation. The molecular ions created in various ionic states, especially those excited states, undergo interesting dynamic processes: electronic predissociation (ion fragmentation); intramolecular energy redistribution (internal conversion and intramolecular vibrational relaxation); and radiation transition (fluorescence). Very few molecular ions larger than diatomic ions fluorescence,[3,27] indicating that radiationless processes must be the dominant ones in their decay mechanism. The rate and the time scale of these radiationless processes (intramolecular processes) are of great importance in our understanding about the nature and the principles of intramolecular dynamics.

Now with femtosecond lasers relatively easily available, one can, in principle, perform real-time measurements on the details of intramolecular dynamic processes. But, the limited photon energies, fluxes and the inherited band widths $\geqq 0.100$ eV, limited through the **Heisenberg** uncertainty principle, make real-time measurements of energy transfer between discrete molecular ionic states very limited. However, an alternative way does exist which is much more versatile and powerful. It is to perform high-resolution measurements in the energy domain. Through the **Heisenberg** uncertainty principle, energy peak shape can give phenomenological lifetimes for molecular ionic states and the rate of decay of intramolecular dynamics.

As discussed in previous sections, photoelectron spectroscopy is capable of resolving vibrational details of the electronic states of molecular ions. The photoelectron leaves the ion on a time scale of $\tau \lesssim 10^{-15}$ second. Thus for those stable ionic states (with life time $\tau \gtrsim 10^{-12}$ second), the photoelectron experiences essentially a uniform (decaying

with distance) potential as it travels away from the ionization region and gives rise to inhomogeneous line shapes. For those unstable states of the molecular ion (with life time $\tau \leqq 10^{-13}$ second), a non-uniform (fast varying) potential is experienced by the ejected photoelectron, this generates homogeneously (life time) broadened line shapes.

The finite resolution available (after careful deconvolution of the instrument response function) from the photoelectron spectrometer limits the time for decay over which the photoelectron line shapes are sensitive to $\tau \leqq 2 \times 10^{-13}$ seconds (from the **Heisenberg** uncertainty principle: $\Delta E \circ \Delta t \geqq \frac{\hbar}{2}$, $\hbar = 0.6582122$ eV·fs; this translates to an effective resolution $\leqq 3$ meV). Thus, the outgoing photoelectron carries information about the molecular ion intramolecular dynamics on the femtosecond time scale. A detailed line shape analysis can in principle give us information regarding the ultra fast intramolecular dynamic processes of the molecular electronic states populated by the photoionization process.

Dynamic processes, just like kinetic processes, are often studied using rate expressions involving one or several rate constants. But, to measure a rate constant of intramolecular dynamic process on the femtosecond time scale is not the most productive way of getting information about these processes. An alternative formulation, in which they are described in terms of time autocorrelation functions, is also of great interest and provides complementary information to those obtained by rate expressions. The autocorrelation function gives indications on how long some given system properties persists until they are washed out by dynamic averaging processes. They can, in principle, be calculated from a model. But it is also possible and much more convenient to obtain them directly from experiment measurements, as the **Fourier** transform of the spectral profile of either an absorption or emission band. This method has been widely used in various field of molecular spectroscopy, in particular **NMR, IR, Raman,** that have

provided a wealth of information on intermolecular forces. In ultra fast pulse laser techniques, the autocorrelation function is used to measure the quality and stability of the laser system on the femtosecond time scale. This autocorrelation function approach has proved to be very helpful in getting the qualitative pictures of molecular ion intramolecular dynamics on a femtosecond time scale.[28-34]

The autocorrelation function formalism to interpret the electronic spectroscopy and intramolecular dynamics of molecular electronic excited states was first elucidated by **Heller**. [28] He showed that the **Fourier** transform of an electronic absorption band profile *I* (E) was equal to an overlap integral between two nuclear wave functions $\phi(0)$ and $\phi(t)$:

$$\langle\phi(0)|\phi(t)\rangle = \int_{-\infty}^{+\infty} \frac{I(E)}{E} e^{-iEt/\hbar} dE \div \int_{-\infty}^{+\infty} \frac{I(E)}{E} dE) \qquad (1.16)$$

where $\phi(0)$ is the nuclear wave function of the ground state prepared on the **PES** of an upper electronic state by a vertical **Franck–Condon** transition, and $\phi(t)$ is the wave function at time t as it propagates from its initial position on the **PES** of the upper state. The denominator in equation (1.16) ensures that the correlation function is normalized to unity at time t = 0. We define a vibrational correlation function **C** (t) which is equal to the modulus of this overlap integral

$$\mathbf{C}\ (t) = |\langle\phi(0)|\phi(t)\rangle|. \qquad (1.17)$$

and we know that the photoionization cross section $\sigma\ (E) \propto \frac{I(E)}{E}$.

A.L. Lorquet, J.C. Lorquet et al. in a series of papers [29] first demonstrated that the correlation function as shown in equation (1.16) and (1.17) can also be calculated

from a photoelectron band with a similar **Fourier** transform procedure used by **Heller**. A variation on the method was used by **Pollard** [30] et al. to evaluate vibrational correlation function for ethylene ion, and by **Reutt** [31-32] et al. for several molecular ions in the small polyatomic molecules limit (H_2O, D_2O and C_2H_2, C_2D_2). **J.E. Reutt** also has given a fairly detailed derivation of the vibrational correlation functions [33] (which is used extensively in this thesis). Only a very brief derivation is given here.

Make use of the completeness relation to a set of eigenstates $|E\rangle$ of the molecular Hamiltonian $\mathcal{H}$:

$$\int_{-\infty}^{+\infty} |E'\rangle\langle E'|\, dE' = 1, \tag{1.18}$$

and

$$\int_{-\infty}^{+\infty} \delta(E-\mathcal{H})\, |E'\rangle\langle E'|\, dE' = \delta(E-\mathcal{H}) \tag{1.19}$$

Express the **Dirac** δ function into the right side of equation (1.19)

$$\int_{-\infty}^{+\infty} \delta(E-E')|E'\rangle\langle E'|\, dE' = \frac{1}{2\pi} \int_{-\infty}^{+\infty} e^{i(E-\mathcal{H})t/\hbar}\, dt \tag{1.20}$$

and we have:

$$|E\rangle\langle E| = \frac{1}{2\pi} \int_{-\infty}^{+\infty} e^{iEt/\hbar}\, e^{-i\mathcal{H}t/\hbar}\, dt \tag{1.21}$$

Consider an electronic transition, under the **BO** approximation, and make use of the **Franck–Condon** principle. In the dipole approximation, we could determine the transition intensity by its transition moment:

$$I(E) \propto E|R_{if}(E)|^2 = E\left(\overline{M}^{el}_{if}\right)^2 |\langle 0|E\rangle|^2 \tag{1.22}$$

where $\left(\overline{M}^{el}_{if}\right)^2$ is the electronic part of the transition moment (assumed to be a constant here); $|0\rangle$ and $\langle E|$ are now pure vibrational wave functions of the lower and upper electronic states, respectively. Put equation (1.21) into equation (1.22), and we have:

$$\frac{I(E)}{E} \propto \int_{-\infty}^{+\infty} e^{iEt/\hbar} \langle\phi(0)|\, e^{-i\mathcal{H}t/\hbar} |\phi(0)\rangle\, dt \tag{1.23}$$

where $\mathcal{H}$ is the nuclear Hamiltonian of the excited state. When transferred on the **PES** of the upper state, ket $|\phi(0)\rangle$ represents the initial position of the wave packet at time t = 0, and the $e^{-i\mathcal{H}t/\hbar}|\phi(0)\rangle$ represents the wave packet at time t as it propagates on the upper (ionic) **PES.** Then:

$$\frac{I(E)}{E} \propto \int_{-\infty}^{+\infty} e^{iEt/\hbar} \langle\phi(0)|\phi(t)\rangle\, dt \tag{1.24}$$

An inverse **Fourier** transformation and normalization gives us equation (1.16) and (1.17).

$$\langle\phi(0)|\phi(t)\rangle = \int_{-\infty}^{+\infty} \frac{I(E)}{E} e^{-iEt/\hbar}\, dE \div \int_{-\infty}^{+\infty} \frac{I(E)}{E}\, dE) \tag{1.16}$$

$$C\,(t) = |\langle\phi(0)|\phi(t)\rangle|. \tag{1.17}$$

By measuring the photoionization cross section for the electronic state we are interested at a discrete energy, applying the appropriate **Fourier** transform method, we can calculate the correlation function for that electronic state. The correlation function so obtained permits us to gain information about intramolecular dynamics of a wave packet composed of discreet adiabatic (in the **BO** sense) eigenstates as they evolve on the excited state **PES** on the femtosecond time scale.

The vibrationally resolved photoelectron spectroscopic features can in this formalism be interpreted as having their origin from the ultra fast intramolecular dynamics. By the **Heisenberg** uncertainty principle, the broadest feature of the spectrum obtained, the photoelectron bandwidth, gives the time resolution in the correlation function. For a typical photoelectron band width of one electron volt or so, the time resolution is about a few tenths of a femtosecond. The narrowest feature, limited by the instrumental energy resolution, defines the time window over which the autocorrelation function is meaningful. A resolution of 10 meV FWHM gives a time window of 0 ~ 70 femtosecond. But, careful deconvolution of the instrument response function; elimination of rotational and sometimes spin-orbital contributions to the vibrational autocorrelation function; an effective resolution of < 3 meV was achieved. This extends the time window to ~ 200 femtoseconds for those stable states.

To evaluate the vibrational correlation function, we have to determine $\sigma(E)$ vs. E from $\mathbf{I}(E)$ vs. E which we measure in photoelectron spectroscopy, since $\frac{\sigma(E)}{E} \propto . \frac{\mathbf{I}(E)}{E}$. This is accomplished by deconvoluting the instrument response function $\mathbf{I}(E)_{ir}$, which is determined from the photoelectron spectra of a rare gas with ionization potential comparable to the band of interest. The contributions of the finite rotational temperature in a supersonic molecular beam experiment (typically 5 ~ 10 **Kelvin**) and the rotational excitations' contribution to the vibrational correlation function were eliminated by convoluting $\mathbf{I}(E)_{ir}$

with a gaussian function $\mathbf{I}(E)_g$ to generate a rotationally broadened instrument response function. The width of the gaussian function was chosen from the average rotational constant, $\mathbf{B_{avg}}$, of the molecular ion for the particular electronic state (if available), the finite rotational temperature and the rotational selection rules for photoionization.

The vibrational correlation functions were determined by the following procedure. Each photoelectron band was isolated and the empirically determined background plus any constant background was removed. The resulting band was then normalized to give **I**(E), and **Fourier** transformed using a discrete **FFT** [35] procedure. The combined effects of the instrument response function and rotational broadening were then removed. This is achieved by dividing the separate **FFT** of the $\mathbf{I}(E)_{ir}$ (normalized) and $\mathbf{I}(E)_g$ (normalized) into the **FFT** of the **I**(E). The modulus of the quotient is then evaluated, giving the vibrational correlation function. The method is summarized:

$$C^{vib}(t) = |\langle\phi(0)|\phi(t)\rangle| \propto$$

$$\left| \int_{-\infty}^{+\infty} \mathbf{I}(E)\, e^{-iEt/\hbar}\, dE \right| \div$$

$$\left| \int_{-\infty}^{+\infty} \mathbf{I}(E)_{ir}\, e^{-iEt/\hbar}\, dE \times \int_{-\infty}^{+\infty} \mathbf{I}(E)_g\, e^{-iEt/\hbar}\, dE \right| \qquad (1.25)$$

For those states that have spin-orbital splittings, which introduces an oscillatory factor in the vibrational correlation function, additional correction must be made to remove this oscillatory contribution. This effect is removed by dividing the correlation function by $|\cos(\Omega t/2\hbar)|$, as suggested by **Lorquet** et al.. [29b] The value of Ω is selected close to the spin-orbital splitting of the element that makes the most contribution to the splitting.

Very recently, **F. Remacle** et al.,[34] have suggested that there exists a relationship between the vibrational correlation function C(t) and the population decay function **P**(t) for the particular electronic state we are interested. They defined an average population decay curve $\mathbf{P}_{av}(t)$ valid in a particular time period, and $\mathbf{C}_{av}(t)$ the average correlation function. It was pointed out by these authors that for a specific excitation, the exact initial rate of decay (valid up to the dephasing time $\mathbf{T}_1$) is equal to the initial slop of $|C(t)|^2$, and the subsequent time evolution can be obtained by averaging $|C(t)|^2$ over its oscillation. This generates $|C(t)|^2_{av}$ whose area (from $\mathbf{T}_1$ onwards) is directly related to an average decay lifetime. At time $t > \mathbf{T}_1$, to a good approximation, the average decay curve $\mathbf{P}_{av}(t)$ can be derived by multiplying $|C(t)|^2_{av}$ with an appropriate constant. This method is adopted to estimate some of the ionic-states average decay lifetimes.

The vibrational correlation function, described in the preceding paragraphs, is a very sensitive measure of the stability of a vibrational wave packet on a **PES**; through which we can get both qualitative and quantitative information about the decay and dynamics of the ionic excited states **PES**. And we can gain valuable insight into the ultra fast decay mechanism of the molecular ions on highly excited electronic states on the femtosecond time scale.

In this dissertation the helium **I**α photoelectron studies of the spectroscopy and intramolecular dynamics of a series of molecular ions are presented. The systems studied: H_2CO^+,D_2CO^+; H_2CCO^+, D_2CCO^+, have a long history of both experimental and theoretical interests. The electronic spectroscopy of these ions in all of the electronic states accessible by the Helium **I**α radiation, however, is very limited. The unimolecular decomposition of these systems has proven to be very rich. Especially, very little is known and much ambiguity remains concerning the intramolecular dynamics of the electronic excited states of these molecular ions.

One of the major focuses of this dissertation is the effective coupling of supersonic molecular beam sampling and a unique double-pass high resolution electron energy analyzer that enables us to obtain much higher resolution photoelectron spectra than was previously available. Many features of the vibrationally resolved spectra of the ions are elucidated here for the first time, and much refined and previously unknown spectroscopic constants are reported. The observation of strong isotope effects on vibronic coupling further confirmed earlier theoretical calculations that great care must be taken to interpret spectra of isotope substituted molecules. The vibrational correlation formalism, as briefly discussed in this introduction, has been applied to the photoelectron bands. The femtosecond intramolecular dynamics of these molecular ions have been studied experimentally for the first and have provided future theoretical works with much needed experimental data.

The remainder of this dissertation is organized as follows: Chapter Two gives a description of the experimental techniques that are common to all of the work in this dissertation. The Helium Iα photoelectron spectroscopy and the intramolecular dynamics of formaldehyde and ketene as well as their deuterium substituted molecules are presented separately in two subsequent chapters. Chapter Three presents the H_2CO^+ and D_2CO^+ system. The H_2CCO^+ and D_2CCO^+ systems are presented in Chapter Four. In the final chapter, the conclusion and a personal verisimilitude of the future of high resolution photoelectron spectroscopy are discussed.

References:

1. A. Einstein, Ann. Phys. 17, 132 (1905).

2a. T. Koopmans, Physica, 1, 132 (1934).

2b. W.R. Richards, Int. J. Mass Spectr. & Ion. Phen., 2, 419 (1969).

3a. J.P. Maier, *ibid*, 104, 1-22 (1991).

3b. K.P Hube, G. Herzberg, Molecular Spectra and Molecular Structures IV, Constants of Diatomic molecules, Van Norstrand Reinhold Co., (1979).

4. J.E. Pollard, Ph.D. Thesis, Department of Chemistry, The University of California at Berkeley (1982).

5. H.A. Bethe, R. Jackiew, Intermediate Quantum Mechanics, Benjamin Cummings Pub. Co., (1986)

6a. J. Franck, Trans. Faraday Soc., 21, 536 (1925).

6b. E.U. Condon, Phys. Rev., 32, 858 (1928).

7. G. Herzberg, Molecular Spectra and Molecular Structures I, Diatomic Molecules, Van Norstrand Reinhold Co., p 194-203 (1950).

8. J.W. Rabalais, Principles of Ultraviolet Photoelectron Spectroscopy, John Wiley & Sons., NY., p53-54 (1977).

9. A. Messiah, Quantum Mechanics, Vol. I, p320, John Wiley & Sons., New York. (1976).

10. D.C. Moule, in Vibrational Spectra & Structures, ed. by J.R. Durig, Elsevier Sci. Pub. Com., p228-271 (1977).

11a. L.S. Cederbaum, W. Domcke, J. Chem. Phys., 64(2), 603-611 (1975).

11b. W. Domcke, L.S. Cederbaum, *ibid*, p612-625 (1975).

12. K. Takeshita, J. Chem. Phys., 94(11), 7259-7265 (1991).

13. K. Takeshita, *ibid*, 96(2), 1191-1209 (1992).

14. R.S. Mulliken, Rev. Mod. Phys., 14, 204 (1942).

15a. A.D. Walsh, J. Chem. Soc., 2260 (1953).

15b. D.C. Moule, A.D. Walsh, Chem. Rev., 75(1), 67-84 (1975).

16. R.J. Buenker, S.D. Peyerimhoff, Chem. Rev., 74(2), 127-188 (1974).

17a. M. Born, J.R. Oppenheimer, Ann. Phys.(Lepzig), 84, 457-484 (1927).

17b. M. Born, Nachr. Akad. Wiss. Gottingen, Math.-Phys. KL, IIa, P1 (1951).

17c. M. Born, K. Huang, Dynamics of Crystal Lattice, Oxford U. Press, NY., (1954).

18. R. Englman, The Jahn-Teller Effect in Molecules and Crystals, John Wiley & Sons Interscience, New York (1972).

19. G. Fisher, Vibronic Coupling, Academic Press, Orlando (1984).

20. I.B. Bersuker, V.Z. Polinger, Vibronic Interactions in Molecules and Crystals, Springer-Verlag, New York (1989).

21. H. Koppel, W. Domcke, and L.S. Cederbaum, Adv. Chem. Phys., 57, 59 (1984)

22. R.L. Wheatten, G.S. Ezra, and E.R. Grant, Annul. Rev. Phys. Chem., 36, 277 (1985).

23. M. Kasha, Discuss. Faraday Soc., 9, 14 (1950).

24. J.P. Maier, in Kinetics of Ion-Molecule Reactions, ed. by P. Ausluos Plenum, New York, P437 (1979).

25. A. Messiah, Quantum Mechanics, Vol. II, John Wiley & Sons Interscience, New York (1976).

26a. L.S. Cederbaum, and W. Domcke, J. Chem. Phys., 64(2), 603 (1975).

26b. W. Domcke, and L.S. Cederbaum, *ibid*, 64(2), 612 (1975).

27. J.P. Maier ed., Ion and Cluster Ion Spectroscopy and Structure, Elsevier Scientific Publishers B.V. (1989).

28a. E.J. Heller, J. Chem. Phys., 68, 2066 (1978).

28b. E.J. Heller, E.B. Stechel, M.J. Davis, *ibid*, 73(10), 4720 (1980).

28c. E.J. Heller, Acc. Chem. Res., **14**, 368 (1981).

28d. E.J. Heller, R. Sundberg, and D. Tanner, J. Chem. Phys., **76**, 1822 (1982).

29a. B. Leyh-Nihaut, and J.C. Lorquet, ***ibid***, **88(9)**, 5606 (1988).

29b. A.J. Lorquet, J.C. Lorquet, J. Delwiche, and M.J. Hubin-Franskin, ***ibid***, **76(10)**, 4692 (1982).

30. J.E. Pollard, D.J. Trevor, J.E. Reutt, Y.T. Lee, and D.A. Shirley, ***ibid***, **81(12)**, 5302 (1984).

31. J.E. Reutt, L.S. Wang, J.E. Pollard, D.J. Trevor, Y.T. Lee, and D.A. Shirley, ***ibid***, **84(6)**, 3022 (1986).

32. J.E. Reutt, L.S. Wang, Y.T. Lee, D.A. Shirley, ***ibid***, **85(12)**, 6928 (1986).

33. J.E. Reutt, Ph.D. Thesis, Department of Chemistry, The University of California at Berkeley (1986).

34. F. Remacle, M. Desoute-Lecomte, and J.C. Lorquet, J. Chem. Phys., **91(7)**, 4155 (1989).

35. E. Oran Brighan, ***The Fast Fourier Transform*** , Prentice-Hall, Englewood Cliffs, 1974, p164

Figure Captions:

Figure 1. A typical diatomic molecule **AB** in its electronic and vibrational ground state **PES**, and the molecular ion AB^+ created by direct photoionization in its various electronic and vibrational states **PES**. Depicted at the right side of the figure is the photoelectron spectrum of the corresponding **PES**. For details concerning the shape of the photoelectron band, see main text.

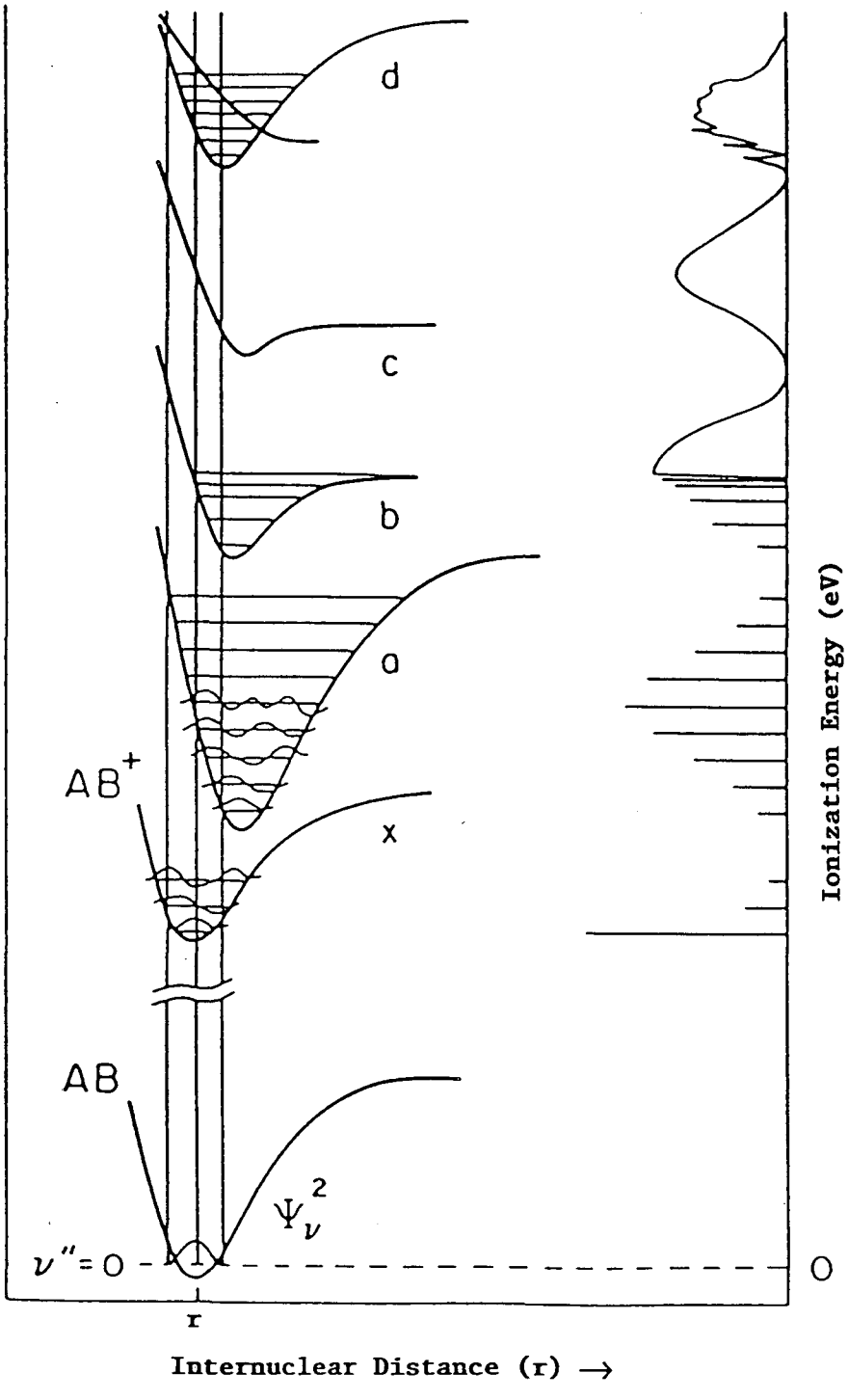
d
c
b
a
x
AB+
AB
Ψν2
ν"=0
0
r
Ionization Energy (eV)
Internuclear Distance (r) →

Figure 1

Chapter Two: Experimental

The apparatus and experimental method common to all chapters of this dissertation will be described in this chapter. Four sections will each describe the apparatus; maintenance of the apparatus; tuning and calibration of the apparatus; and the experimental conditions used for all the experiments reported in this dissertation.

The apparatus that is essential to this dissertation had been documented in great detail by four Ph.D. dissertations from this group.[1-4] The first section of this chapter covers the apparatus very briefly. Maintenance, tuning and calibration of the spectrometer are essential to the success of any experiment. These have not been explained at any length previously. They are detailed in the second and the third section, to facilitate future, more productive use of the apparatus. In the last section, experimental conditions used for all the experiments contained in this dissertation are described together, with detailed procedures to prepare and purify the samples.

A. Description Of The MBPES Machine

The Molecular Beam Photoelectron Spectrometer (MBPES) used for this dissertation had been described in great details in James E. Pollard,[1] Dennis J. Trevor,[2] Janice E. Reutt [3] and Laisheng Wang's Ph.D.[4] theses. It will only be covered briefly here for completeness.

1. Vacuum System and Beam Source Chamber

The MBPES apparatus as shown in Figure 1 is based on a 16-inch diameter stainless steel six-way cross for the main chamber. It is accessible to the supersonic molecular beam source; the high-resolution electrostatic electron-energy analyzer; the quadrupole mass spectrometer; and the helium discharge lamp. These four flange-mounted units are equipped with differential pumping capabilities. The main chamber is pumped by

two LN_2 baffled diffusion pumps (Varian VHS-6) with a combined pumping speed of 1800 liters per second.

The beam source consists of a 70 μm diameter nozzle (which can be changed) and a 0.858 mm diameter, 6.4 mm tall skimmer (the skimmer can be changed), with a normal nozzle-to-skimmer distance of D_{ns} = 6.4 mm (adjustable to maximize beam intensity without compromising resolution), pumped by an unbaffled 4000 liters per second diffusion pump (Varian VHS-10) backed by a 1000 liters per second Roots blower (Edwards EH-1200) and an 80 cfm mechanical pump (Edwards E2M-80). The nozzle assembly can be cooled by a LN_2 filled jacket and heated up to 400 °C by a non-inductively wound Nichrome heating cable. Under typical running conditions (for experiments reported in this dissertation) with a stagnation pressure of 700 torr at 25 °C, the beam source chamber pressure is $< 5 \times 10^{-5}$ torr. The main chamber pressure is $< 2 \times 10^{-6}$ torr which is an absolutely necessary condition to eliminate the problem of photoelectrons being scattered by the background molecules.

2. High Resolution Electrostatic Electron Energy Analyzer

The electron energy analyzer consists of four major components: the electrostatic lenses; the 90° sector analyzer; the hemispherical analyzer and the multichannel detector. The entire analyzer is connected to the main chamber via a 1.79-mm diameter aperture through which the photoelectron travels. The photoelectron first encounters two asymmetric three-element cylindrical electrostatic lenses. The first three-element lens sets the fixed pass energy at which the photoelectrons travel through both the 90° sector analyzer (8.00 eV at present) and the hemispherical analyzer (1.000 eV at present). The second three-element lens performs the actual scan of electron kinetic energies and focuses the photoelectrons at the entrance of the 90° sector analyzer. The 90° sector analyzer was intended to reduce the background. The photoelectrons that emerge from the exit aperture (1.79 mm at present) of the 90° sector analyzer travel through another three-element

asymmetric lens that decelerates the electrons to 1.000 eV and focuses the electrons at the entrance to the hemispherical analyzer. The photoelectrons are then dispersed according to their kinetic energies and detected by the detector, which consists of a pair of 40 mm active diameter MCP in chevron configuration, a resistive anode, and position-encoding electronics.

The analyzer chamber is pumped by two LN_2 baffled diffusion pumps (Varian VHS-4) with a combined pumping speed of 920 liters per second. The differential pumping arrangements of the analyzer chamber ensure that the pressure in the chamber is < 2×10^{-8} torr with the molecular beam running. This differential pumping is absolutely necessary to maintain the highest resolution obtainable, a constant dispersion function of the analyzer, and the protection of the analyzer surfaces and detector assembling.

The resolution obtainable depends strongly on the pass energies of the 90° sector, and the hemispherical analyzers. For experiments described in this dissertation, the pass energies were set at 8.00 eV for the 90° sector, and 1.000 eV for the hemispherical analyzers. Under these conditions, the highest resolution achieved was 9.6 meV (FWHM) as measured by Ar^+ $^2P_{1/2}$, $^2P_{3/2}$ peaks.

3. The Quadrupole Mass Spectrometer (QMS)

The quadrupole mass spectrometer (Extranuclear Laboratory) has been used extensively to perform molecular beam diagnosis. The QMS consists of a quadrupole mass filter, ion optics, RF electronics, and a detector consisting of a spiraltron multiplier and a current amplifier.

The QMS is connected to the main chamber via a 6.4 mm aperture through which the ions are transmitted. The QMS housing is differentially pumped with a 500 liters per second turbomolecular pump and typically maintains pressure of < 5×10^{-8} torr with the molecular beam running.

The current setups of the QMS and the electron energy analyzer are not suitable for photoelectron-photoion coincidence experiments. For photoelectron spectra described in this dissertation, the QMS was not operated. But it was used to do molecular beam diagnosis and to optimize the molecular beam conditions used for these experiments.

4. The Photon Source

A windowless, differentially pumped cold cathode rare gas DC discharge lamp was used for all the experiments in this dissertation. The lamp operating conditions are optimized to produce the helium **I**α (584.3340 Å, 21.21734 eV) resonance line. At typical operating conditions of 1.0 Torr helium and 180 mA discharge current, the lamp produces a photon line width of < 2 meV (estimated) and a photon fluxes around 10^{13} photons per second as measured by a home-built copper photodiode. The radiation distribution of the lamp, as measured by the photoelectron spectra of Argon, was found to be 97.2% helium **I**α (584.3340Å, 21.21804 eV), 2.3% helium **I**β (537.0296Å, 23.08470 eV), 0.4% helium **I**γ (522.2128Å, 23.74209 eV), and < 0.1% of higher resonance lines. Under most circumstances, the contributions from radiation lines other than helium **I**α could be neglected. But they must be taken into account when in doubt about peak assignments.

In principle, the rare-gas discharge radiations of argon, neon, krypton and xenon can also be used. The natural linewidths of the principal **I**α lines are narrower, and the discharge can be achieved at much lower lamp pressures than for helium. This reduces the pressure-broadening contributions to the photon linewidth, but the radiation produced from higher resonance lines is much greater. Unless monochromatization without substantial loss of the photon flux can be performed, these rare-gas radiation lines have very limited application. They were not used for any of the experiments in this dissertation.

B. Maintenance of the MBPES Machine

In this section, the maintenance of the **MBPES** machine is discussed. Since this topic has not been covered in any length by previous publications, every detail is given, to help future researchers who will use the **MBPES** machine.

The **MBPES** machine, when operated under normal conditions, requires very little maintenance if any at all. The major concern is to keep the machine in its best working condition that depends strongly on the cleanness of the main chamber and the analyzer chamber, on the stability of the electronics and power supplies that power and control the voltages for all the lenses and the analyzers. It is preferable if possible to keep the system under vacuum and keep the analyzer chamber pressure at $< 2 \times 10^{-8}$ torr at all times. The power supplies and electronics are left on always to avoid troubles of "warming" up and other interruptions. To minimize power-line-voltage fluctuations during normal operations, the **MBPES** machine has its own isolation transformer on its main power lines which supplies isolated power to the **MBPES** electronics system. An isolated 'clean' grounding point is used for all grounding. The mechanical pumps of the **MBPES** machine are powered from a different power source. The last two conditions are essential in a 'noisy' environment like its current location.

Routine maintenance was done by first purging the system vacuum with dry Argon or dry N_2 from the analyzer chamber slowly, then opening up the system from the beam source flange; and disengaging the beam source chamber from the main chamber. It is advisable to clean the main chamber (the μ-metal) with "Kimwipe" papers soaked with acetone first; followed by "Kimwipe" papers soaked with alcohol; and finally to wipe the surfaces dry of any solvent traces (do not try to use a heat gun to dry the surfaces). It is usually a good idea to cover up the aperture of the analyzer chamber that extends into the main chamber, to avoid any possible contamination of the analyzer chamber during routine cleaning of the main chamber.

The beam source chamber is usually contaminated with diffusion pump fluid, since the diffusion pump used to evacuate the beam source does not have any kind of baffle. This is the major contaminating source under most operating conditions. It has to be cleaned after continuing use for about a month or whenever you suspect that the beam source is too dirty.

It is cleaned by first wiping out most of the pump fluid found in the beam source chamber and beam reducer; followed by removing the nozzle skimmer assembly; sonicating the nozzle aperture and the skimmer with acetone first and then alcohol. The nozzle aperture and the skimmer are then placed in an electric oven heated to around 150 °C for twenty minutes before re-assembling. Before connecting the beam source chamber to the main chamber, check the VHS-10 diffusion pump fluid level, add additional pump fluid if necessary to maintain full pumping speed.

C. Tuning and Calibration of the MBPES Machine

1. Tuning of the MBPES Machine

Tuning up the **MBPES** machine will be necessary whenever the resolution achievable is degraded. At this writing, the causes of this 'degradation' are still not fully understood, but it does seem to correlate with the following conditions: voltages drift of the lens elements and analyzers; the changing of the surface conditions in the main chamber and analyzer chamber usually accompanied by changes in the kinetic energy offset values; changing operating conditions of the lamp; deterioration of the μ-metal magnetic shielding properties. A detailed tuning-up procedure will be described in this section.

a. Overview

Tuning up the **MBPES** machine usually involves checking the conditions of the system cleanliness; the functioning of the lamp; the adjustments on the voltages of various lenses and analyzers to achieve the best resolution. This can be accomplished by running

an about 20 torr Argon beam and changing the V_k (kinetic energy of the photoelectrons) settings to place the Ar^+ $^2P_{1/2}$ or $^2P_{3/2}$ peak at the center of the left or right half of the detector. Do a normal mode scan, make adjustments and check the changes in resolution and transmission.

It is always good practice to keep the **MBPES** machine system as clean as possible by maintaining a good vacuum in the main chamber (with no molecular beam running, its base pressure is $< 8.0 \times 10^{-8}$ torr) and the analyzer chamber (with no molecular beam running, its base pressure after a good bakeout (at 100 °C for 48 hours) is $< 1.0 \times 10^{-8}$ torr. Since contamination from the beam source is unavoidable under prolonged operation, it's highly recommended that the beam source chamber and main chamber be cleaned periodically. While cleaning the main chamber, check the residual magnetic field inside the chamber with a gaussmeter. It should give the following readings: vertical ~ 50 mGauss, north-south ~ 15 mGauss, and east-west ~ 10 mGauss at the center of the main chamber (near the ionization region).

b. Cleaning and Reconditioning of the Lamp

With clean beam source and main chambers, the next step is to make sure that the lamp is functioning properly. This can be done by operating the lamp at different conditions and check for changes in resolution. This is very sensitive especially at lower lamp pressures. If the lamp is functioning properly, at 1.5 torr Helium and 200 mA discharge current, the resolution is 1 meV (as measured with Ar^+ $^2P_{3/2}$ peak, it's about 11.6 meV) worse than at 1.0 torr Helium and 180 mA discharge current (10.4 meV), and at 0.5 torr Helium and 160 mA discharge current (9.6 meV) the resolution is ~ 1 meV better than at 1.0 torr and 180 mA. If changes in lamp operation conditions are not correlated with changes in resolution, the lamp needs cleaning and reconditioning.

Cleaning and reconditioning of the lamp can be done by removing the lamp housing from the top of the main chamber first. Second, remove the collimating quartz capillary

from the lamp body. This must be done by following 'clean room' procedure that requires one to wear surgical gloves to prevent 'oil, grease' contamination of the capillary. Third, remove the discharge capillary from the lamp body, and changing to a new capillary. Fourth, remove the Tantalum linings of the cathode and changing to new tantalum sheet linings. The reverse order should be followed to reassembling the lamp. Before install the lamp back on top of the main chamber, check the electric continuity between the tip of the quartz collimating capillary (it's usually coated with Aquadag graphite) and the lamp body. This will eliminate any possible "charging-up effect" in the quartz capillary.

c. Tuning up of the Electronics: V_3 and V_6 Lenses

With a clean beam source chamber and main chamber, and a properly functioning lamp, the next step is the time-consuming 'tuning up' of the electronics, especially all the lens voltage settings. From experience, the most sensitive ones are the V_3 curve and V_6 voltage settings. It is a good practice to record all the previously used settings before attempting to tune any of those voltages.

The V_3 voltages were determined from a series of calibration gases (Ar, Kr, Xe, N_2, O_2, CO, CO_2).[1] The voltages obtained were fitted to a polynomial function and programmed into the computer. The quality of the curve obtained strongly affects the transmission property of the whole system and the best achievable resolution. It is usually optimized by checking at several different V_k values using Ar, Kr, and Xe, adjusting the V_3 value manually until you get the best resolution and transmission, then reprograming the computer to correct for any changes.

The V_6 voltage setting is crucial to the highest resolution achievable, since it is the focusing voltage for the 8:1 three-element asymmetric lens. Its value deviates substantially from the theoretically calculated value. There are two 'sharp' focus values: one is a higher voltage usually around 8.000 ± 4.000 volts, and the other is a lower voltage usually around 1.000 ± 0.500volt (all these voltages were referenced to V_k, the kinetic energy of the

photoelectrons). You should only change the V value 0.1000 volt or less at one time, and check for the resolution at each V setting.

d. Tuning up the 90° Sector Analyzer and the Hemispherical Analyzer

The 90° sector analyzer is also called the prefilter which describes its function very nicely. It not only cuts down the background electrons, but also focuses the electrons that pass through it to the correct position on the following 8:1 three-element asymmetric lens. Its focusing property affects the 8:1 lens very strongly. The V^1_{in}-V^1_{out} value (that is the voltage difference between the inner and outer 90° sector) is correlated with V_3 and V_6 values. After adjusting V_3 and V_6 values, it is usually necessary to adjust the V^1_{in}-V^1_{out} value.

Under most circumstances, the values of V^1_{in}-V^1_{out} are very close to their theoretical ones. It should only be adjusted after everything else has been optimized. It should not be adjusted more than 0.050 eV at one time. You should check the resolution and transmission at each setting, and use the setting that gives the best resolution without compromising too much on transmission.

The hemispherical analyzer needs very little tuning. What you need to do is check all the voltage values against the theoretical ones. Since power supplies drift over time, it is advisable that before you start any measurements, all the voltage settings for the hemispherical analyzer be checked and be tuned to their theoretical values (this includes V^0_{in}, V^0_{in}-V^0_{out}, $V_{fte}(i)$ (i=1,6), here $V_{fte}(i)$ are the six field termination electrodes). Since the power supply for the hemispherical analyzer is very stable, only very fine tuning needs to be performed, and a sufficiently long time should be allowed for the power supply to be stabilized before any new tuning. From experience, the adjustment step size should be < 2.0 meV. You should have at least 5 to 10 minutes between each adjustment.

e. Tuning the Step Size of the Digitizer

The step size of the digitizer must match the dispersion of the hemispherical

analyzer as explained in great detail by James E. Pollard.[1] The dispersion function of the analyzer is a function of not only the pass energy used, but also the surface conditions of the analyzer. The surface conditions of the analyzer are not easily characterized. Its relationship to the dispersion of the analyzer is not known precisely at this writing. Qualitatively speaking, with a fresh molybdenum coating on the hemispherical analyzer surfaces, the dispersion is best at the very beginning. As time goes by, it degrades gradually. Depend on the operating conditions, the degradation rate varies. It is highly recommended that the dispersion of the analyzer be checked before any measurements are made.

This can be done by running a ~ 20 torr of Ar beam. Manually adjust V_k to put the Ar^+ $^2P_{1/2}$ or $^2P_{3/2}$ peak center on the high V_k side of the detector, and do a normal scan. Increase V_k value by ~ 25 meV, do another normal scan, and so on. Then calculate the dispersion of the analyzer by this formula : $D = (V_{k(fin)} - V_{k(ini)}) / (Ch_{ini} - Ch_{fin})$. This gives the dispersion of the analyzer in units of meV per channel. Then go to the digitizer memory control electronics chassis, adjust the gain for the pass energy chosen, match the digitizer step size with the dispersion of the analyzer. This is done by running the program called DACLD. Choose DAC Channel # 1, give initial value 0, read the $V_k(0)$; and final value 500, read $V_k(500)$. $V_k(500) = V_k(0) + 500 \times D$. This should be matched to better than ± 0.1 meV to avoid any loss of resolution during the dithering scan.

2. Calibration of the MBPES Machine

The calibration of the **MBPES** machine was usually carried out every time before an experiment started, and between scans of each experiment. This is done by running noble gases with their ionization potential known precisely, and other molecules with their ionization potential known to be close to the molecules being studied.

One of the major advantages of the **MBPES** machine over traditional gas-phase **PES** machines is the longtime stability of its calibration. For experiments running

noncondensing, or condensing and conducting but non-corrosive gases, the calibration can be very stable. The drift of kinetic energy is less than 0.5 meV per hour. This drift is limited mainly by the stability of the power supply of the lenses and analyzers. For experiments running condensing, nonconducting and corrosive gases, the calibration is less stable. The drift of kinetic energy is about 1 meV per hour This larger drift is caused largely by contact potential effects, which occur when the surfaces surrounding the ionization region are modified by the gases.

The second aspect of the calibration of the **MBPES** machine concerns the linearity of the kinetic energy scale. This has been shown to be very good. Deviations from linearity scale are less than 1meV per 2 eV scan, as measured by the energy difference between N_2^+ $\tilde{X}\,^2\Sigma_g^+$ (v=0) state and $\tilde{B}\,^2\Sigma_u^+$ (v=0) state, which is 3.16981 eV from optical emission spectra [13], and at higher kinetic energy by measuring the difference between Ar^+ (15.75975 eV) and Xe^+ (12.13000 eV) ionization potentials (these values have been accurately determined from optical spectroscopy [14]). The MBPES machine maitains linearity of ±1 meV over this entire energy range. Its fundamental limit, it seems, is the resolution of the 12 bit digital to analog converter which drives the V_k steps, and the stability of all the power supplies. For most experiments, this is more than sufficient to assure that the linearity is not going to be the limiting factor.

Table 1 contains the most frequently used calibration gases and their ionization potentials. All electron kinetic energies are based on ionization using the helium **Iα** (548.3440 Å[15] 171129.148 cm^{-1},[14] 21.21732 eV, using 1986 recommended values, 1eV = 8065.5408 cm^{-1}, [16]) radiation line.

D. Experimental Setups and Conditions

In this section, the experimental conditions common to all experiments reported in this dissertation are presented. The setups used to prepare monomer H_2CO, D_2CO; H_2CCO, D_2CCO and their purification are presented with little explanation, since they were well documented in the literature.[6,7]

1.Procedures to Prepare Pure Monomer H_2CO and D_2CO

The apparatus used to prepare pure monomer H_2CO and D_2CO from their polymeric form (paraformaldehyde 99.5% pure, paraformaldehyde-d_6 99.9% D-atom, from MSD Isotopes) is shown in Figure 3., following the literature [6] closely with minor modifications. We used a larger diameter (20 mm) quartz tube made packed-three-U separator (350 mm long) to purify the monomer. The whole apparatus was set up inside a 100 LFT per minute walk-in fume hood.

It's well known that trace amounts of water catalytically polymerizes monomer formaldehyde into its polymer form. This problem was treated by the following procedures. The apparatus was sealed, and the whole system was pump down to ~ 3×10^{-6} torr using a LN_2-baffled 100 liter-per-second diffusion pump (with DC705 diffusion pump fluid) backed by a two-stage rotary-vane oil-sealed mechanical pump. Then the valve on top of the sample tube was opened to pump off the gases trapped in the sample tube; the tube was heated slightly with a DC704 fluid bath to 100 °C for ~ 30 minutes to drive most of the water out. The system vacuum leveled off at ~ 1×10^{-5} torr. The valve was then closed; the whole system except for the sample tube was baked at ~ 200 °C overnight (this would also remove oxygen on the glass surface)). The system vacuum levels off to ~ 8×10^{-7} torr at the end of the bake out.

While the system was still hot, the valve to the sample tube was opened (while pumping all the time). The sample was heated to 70 °C with the DC704 fluid bath heated by a temperature-controlled electric heating plate. The bottom part of the packed U

separator was cooled down to - 78 °C with a dry ice/acetone slush, while the top 1/3 of the packed-three-U separator was kept at ~ 120 °C by resistive heating with Nichrome wire wound around it and controlled by a Variac. The collector was then cooled down to LN_2 temperature to collect the purified monomer formaldehyde. Any noncondensable gases were pumped away. During the whole preparation process, the vacuum was maintained at ~ 5×10^{-6} torr. The formaldehyde prepared this way was stored at LN_2 temperature while pumping until **MBPES** experiments started.

Essentially the same procedure was followed to prepare pure monomer D_2CO, except at the very beginning. Due to the much higher cost of D_2CO polymer, the sample was degassed and dehydrated at room temperature (instead of 100 °C) for about two hours without heating. The system vacuum was about 5×10^{-6} torr after this degassing.

For both H_2CO and D_2CO, the preparation process took about 48 hours (not including the bakeout time) to get about 20 grams of pure monomer. The monomers prepared this way seemed to be very stable when stored at LN_2 temperature, with no sign of polymerization or decomposition.

2. Procedures to Prepare and Purify H_2CCO and D_2CCO

The apparatus used to prepare H_2CCO and D_2CCO from pyrolysis of acetic anhydride and acetic anhydride-d_6 was similar to the ones used in Prof. C. B. Moore's group with minor modifications, Figure 4. The differences are a longer pyrolysis quartz tube ~ 25 cm and a larger cold-finger trap.[7]

The system was first pumped down to a vacuum of ~ 3×10^{-6} torr using the same pumping system as in formaldehyde preparation. Then the sample was degassed using several freeze-thaw cycles. The valve on top of the sample vial was closed after this. The system was then baked out at ~ 200 °C overnight to reach a base vacuum ~ 6×10^{-7} torr at the end of the bakeout.

The quartz pyrolysis tube was heated to ~ 550 °C (measured with a thermocouple) with Nichrome wire wound around it and controlled by a Variac. The cold finger trap was cooled down to - 78 °C with a dry ice/acetone slush. Collector #1 was cooled down to LN_2 temperature to collect the product while collector #2 was at ~ 100 °C. Now, the valve to the sample vial was opened. During the whole process, the system vacuum was maintained at ~ 5×10^{-6} torr. After enough ketene had been collected (~ 40 grams in 48 hours) in collector #1, the valve between the cold finger and collector #1 was closed first, the sample vial valve was closed next and the heating turned off on the pyrolysis tube.

The ketene prepared was then vacuum distilled once from a LN_2/hexane slush (with temperature ~ -96 °C) in collector #1 to LN_2 temperature in collector #2, and stored in collector #2 at LN_2 temperature under dark with pumping on until the **MBPES** experiments started. The ketene prepared in this way was very stable; free of CO_2, and showed no sign of decomposition when stored at LN_2 temperature under dark. D_2CCO was prepared and stored by exactly the same procedure under the same conditions.

3. Experimental Conditions for H_2CO and D_2CO Photoelectron Spectroscopy

The Photoelectron spectra of H_2CO and D_2CO were taken under similar conditions. The monomer H_2CO or D_2CO was kept at dry ice/acetone slush temperature. Its vapor pressures were about 35 torr and 30 torr, respectively, when measured with a Baratron (MKS model 122AA-2000). About 300 torr of ultra-pure He (Matheson 99.9999 %) was first passed through an U tube maintained at LN_2 temperature to remove trace amount of water, then bubbled through H_2CO or D_2CO, making the total pressure ~ 350 torr. The gas line was first cleaned by heating up to 200 °C for ~ 2 hours with the pump on. Then 300 torr of dry helium was run for ~ 2 hours. Immediately after an Ar calibration run, the photoelectron spectra of H_2CO and D_2CO were taken. It has been shown that as long as the partial pressure of H_2CO or D_2CO was less than 40 torr, no polymerization happens.[8]

The photoelectron spectra of H_2CO and D_2CO were each taken in four separate scans. Each scan lasted about two hours, and each scan was followed by an Ar calibration scan. The kinetic energy scale shift was less than 1 meV from scan to scan as calibrated with Ar. To enhance statistics, all scans were repeated three times. For each compound, a total of sixteen scan were done.

The mixture of He/H_2CO and He/D_2CO with total pressure ~ 350 torr was expanded through a 70 μm converging type molybdenum nozzle, skimmed by a 0.858 mm diameter 6.4 mm tall stainless steel skimmer with D_{ns} = 6.4 mm. The beam source chamber pressure was 5×10^{-5} Torr. The main chamber pressure was 3×10^{-6} torr. The analyzer chamber pressure was at 1.9×10^{-8} torr during the scans. The resolution was 10.4 meV **FWHM** as measured with Ar $^2P_{1/2}$, $^2P_{3/2}$ and Xe $^2P_{1/2}$, $^2P_{3/2}$. Under these conditions, no polymer or clusters of formaldehyde were found by using the **QMS**. The rotational temperature was < 10 K as shown by laser induced fluorescence **(LIF)** measurements under similar conditions.[5]

4. Experimental Conditions of H_2CCO and D_2CCO Photoelectron Spectroscopy.

The experimental conditions of H_2CCO and D_2CCO were very similar to those used for H_2CO and D_2CO with the exception that the samples were kept at Hexane/LN_2 slush temperature (- 96 °C, vapor pressure 50 and 45 torr) instead of dry ice temperature (- 78 °C, vapor pressure 100 torr) to minimize possible dissociation of ketene. It was later confirmed by photoelectron spectra taken at dry ice/acetone slush temperature that ketene prepared and stored in the procedures described in this section was free of CO_2 dissociation products.

The photoelectron spectra of H_2CCO and D_2CCO were each taken by five separate scans. Each scan lasted about 2 hours, followed by an Ar calibration scan. The kinetic energy scale shift was < 1 meV from scan to scan as calibrated with Ar. To enhance

statistics, all scans were repeated three time. Thus for each compound a total of 20 scans were done.

The mixture of He/H_2CCO and He/D_2CCO with a total pressure ~ 300 torr was expanded through a 70 μm nozzle and skimmed by a 0.858 mm diameter 6.4 mm tall stainless steel skimmer with D_{ns} = 6.4 mm. The beam source chamber pressure was 3×10^{-5} torr; the main chamber pressure was 2×10^{-6} torr and the analyzer chamber pressure was 1.8×10^{-8} torr during the scans. The resolution was 11.6 meV FWHM as measured with Ar $^2P_{3/2}$.

Under these conditions, no dimer or higher clusters of ketene were found by using the **QMS**. The rotational temperature was estimated to be < 10 K. This was confirmed by **LIF** experiments carried out under similar conditions.[9-12]

References:

1. James E. Pollard, Ph.D. Thesis, Department of Chemistry, The University of California at Berkeley (1982).
2. Dennis J. Trevor, Ph.D. Thesis, Department of Chemistry, The University of California at Berkeley (1980).
3. Janice E. Reutt, Ph.D. Thesis, Department of Chemistry, The University of California at Berkeley (1986).
4. Laisheng Wang, Ph.D. Thesis, Department of Chemistry, The University of California at Berkeley (1990).
5. W. E. Polik, Ph.D. Thesis, Department of Chemistry, The University of California at Berkeley (1988).
6. R. Spence, W. Wild; J. Chem. Soc., **338** (1935); **506**(1935).
7. G.J. Fisher, A.F. MacLean, A.W. Schwizer; J. Org. Chem., **18**, 1055(1953)
8. Dr. Roger Van Zee, private communication.
9. I-C Chen, and C.B. Moore, J. Phys. Chem., **94**, 263 (1990)
10. I-C Chen, and C.B. Moore, J. Phys. Chem., 94, 269 (1990)
11. E.R. Lovejoy, S.K. Kim, and C.B. Moore, Science, **256**, 1541 (1992)
12. I-Chia Chen, W.H. Green, Jr., and C. B. Moore, J. Chem. Phys., **89(1)**, 314 (1988)
13. A. Lofthus, and P.H. Krupenie, J. Phys. Chem. Ref. Data, **6**, 113 (1977)
14. Atomic Energy Levels, Vol. I, II, III, ed. by C. E. Moore, (National Bureau of Standards, Washington D.C., 1958).
15. J. Eland, **Photoelectron Spectroscopy**, 2nd ed, Butterworths, p32(1984).
16. E. R. Cohen, and B. N. Taylor, **The 1986 Adjustment of the Fundamental Physical Constants**, report of the CODATA Task Group on Fundamental Constants, CODATA Bulletin 63, Pergamon, Elmsford, NY(1986).

Table 1. Calibration Gases & their Ionization Energies

Calibration Gas	Ionic State	Electron Kinetic Energy (eV)	Ionization Potential (eV)
CH_3I	$^2E_{3/2}$	11.6800	9.5380
CH_3I	$^2E_{1/2}$	11.053	10.1640
Xe	$^2P_{3/2}$	9.0880	12.1300
Xe	$^2P_{1/2}$	7.7820	13.4360
Kr	$^2P_{3/2}$	7.2190	13.9990
Kr	$^2P_{1/2}$	6.5530	14.6650
Hg	$^2D_{5/2}$	6.3780	14.8400
Ar	$^2P_{3/2}$	5.4590	15.7598
Ar	$^2P_{1/2}$	5.2810	15.9370
Hg	$^2D_{3/2}$	4.5140	16.7040
N_2	$^2\Sigma_u^+$	2.4670	18.7510
CO_2	$^2\Sigma_g^+$	1.8236	19.3944
CO	$^2\Sigma_u^+$	1.4980	19.7200
O_2	$^2\Sigma_g^-$	0.9200	20.3580

Figure Captions:

Figure 1 Figure 1 is a schematic top view of the apparatus: (1) beam source, (2) beam catcher (not installed), (3) pass energy selector lens, (4) field lens, (5) kinetic energy scan lens, (6) deflectors, (7) 90° spherical sector preanalyzer, (8) differential pumping wall, (9) 8:1 decelerator lens, (10) hemispherical analyzer, (11) multichannel detector, (12) ion extraction lenses, (13) quadrupole mass filter, (14) differential pumping for various part of the apparatus. The photon source is located above the plane of the drawing. Not shown are two layers of μ-metal magnetic shielding that line the main chamber and surrounding electrostatic lenses, three layers of μ -metal magnetic shielding that line the analyzer chamber, and a grounding plate (with a one inch hole) directly opposite the molecular beam on the far side of the ion optics.

Figure 2 Figure 2 shows the high-resolution electron-energy analyzer, electrostatic lenses, and the multichannel detector in great detail with all the voltage designations, without the μ-metal magnetic shielding in place. F.T.E. stands for Field Termination Electrodes, MCP stands for Microchannel Plates, X_1 and X_2 are the **R**esistive **A**node **E**ncode (**RAE**) outputs.

Figure 3 Figure 3 shows the schematic setups used to prepare monomer formaldehyde and deuterated formaldehyde from paraformaldehyde and d_6-paraformaldehyde. (1) sample vial, (2) ground glass joint with Teflon sleeve sealing, (3) viton seal high vacuum glass valves, (4) packed-three-U separator, (5) monomer collector, (6) to LN_2 trapped diffusion pump. Not shown are the Nichrome wires wound around the connection from the sample vial to and the top 1/3 of the packed-three-U separator, and the

Dewars for the packed-three-U separator (dry ice/acetone slush temperature) and the monomer collector (LN_2 temperature). For operating conditions, see main text.

Figure 4 Figure 4 shows the schematic setups used to prepare and purify ketene and deuterated ketene from acetic anhydride and acetic anhydride-d_6. (1) sample vial, (2) ground glass joint with Teflon sleeve sealing, (3) viton seal high vacuum glass valve, (4) quartz pyrolysis tube, (5) cold finger to collect acetic acid, the by-product, (6) collector # 1, (7) collector # 2, (8) Nichrome heating wire, (9) to LN_2 trapped diffusion pump. Not shown are Dewars used to maintain LN_2 temperature during preparation for collectors # 1 & 2, and a thermocouple used to measure the pyrolysis temperature. For operation conditions, see main text.

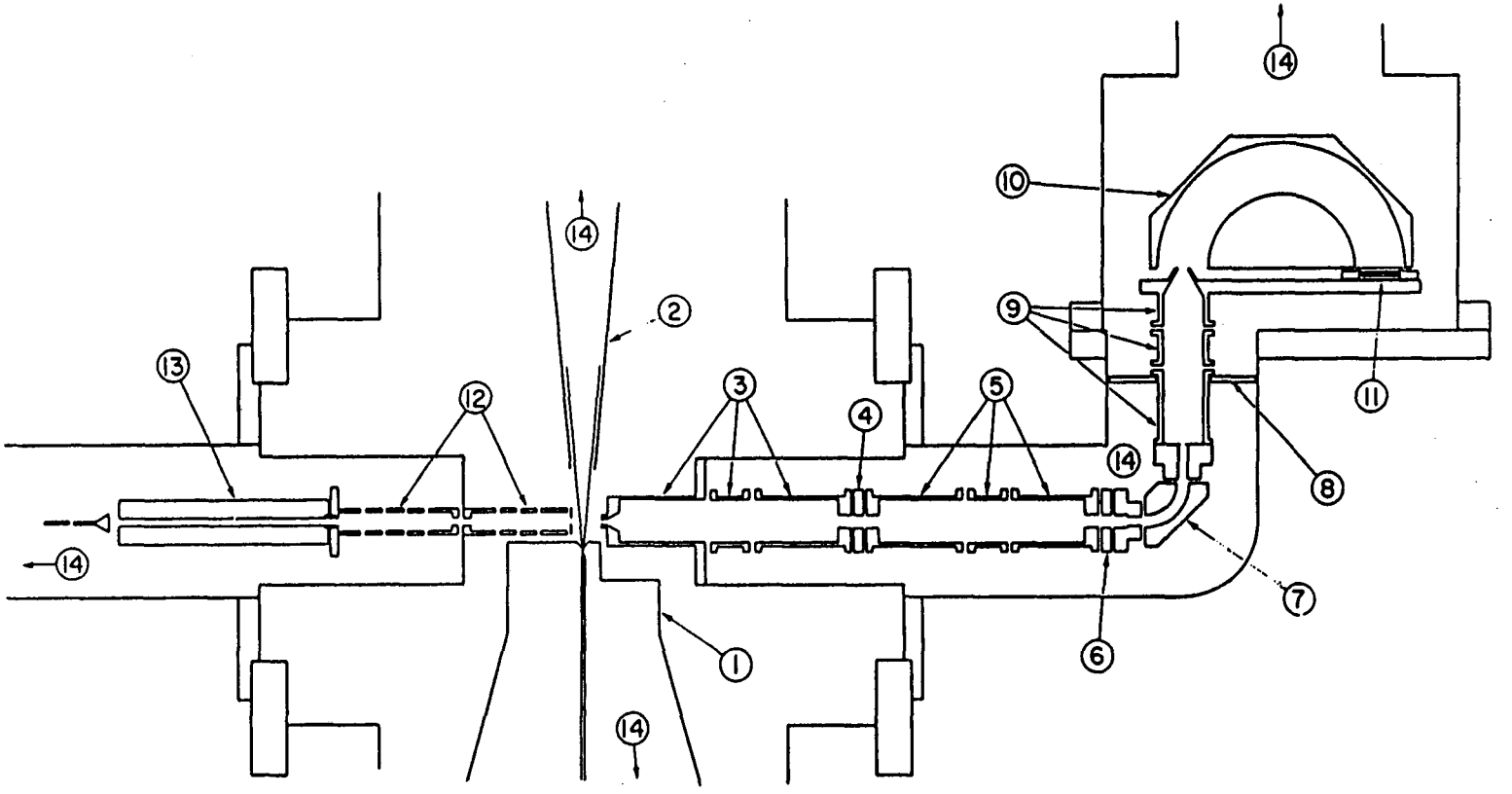

Figure 1

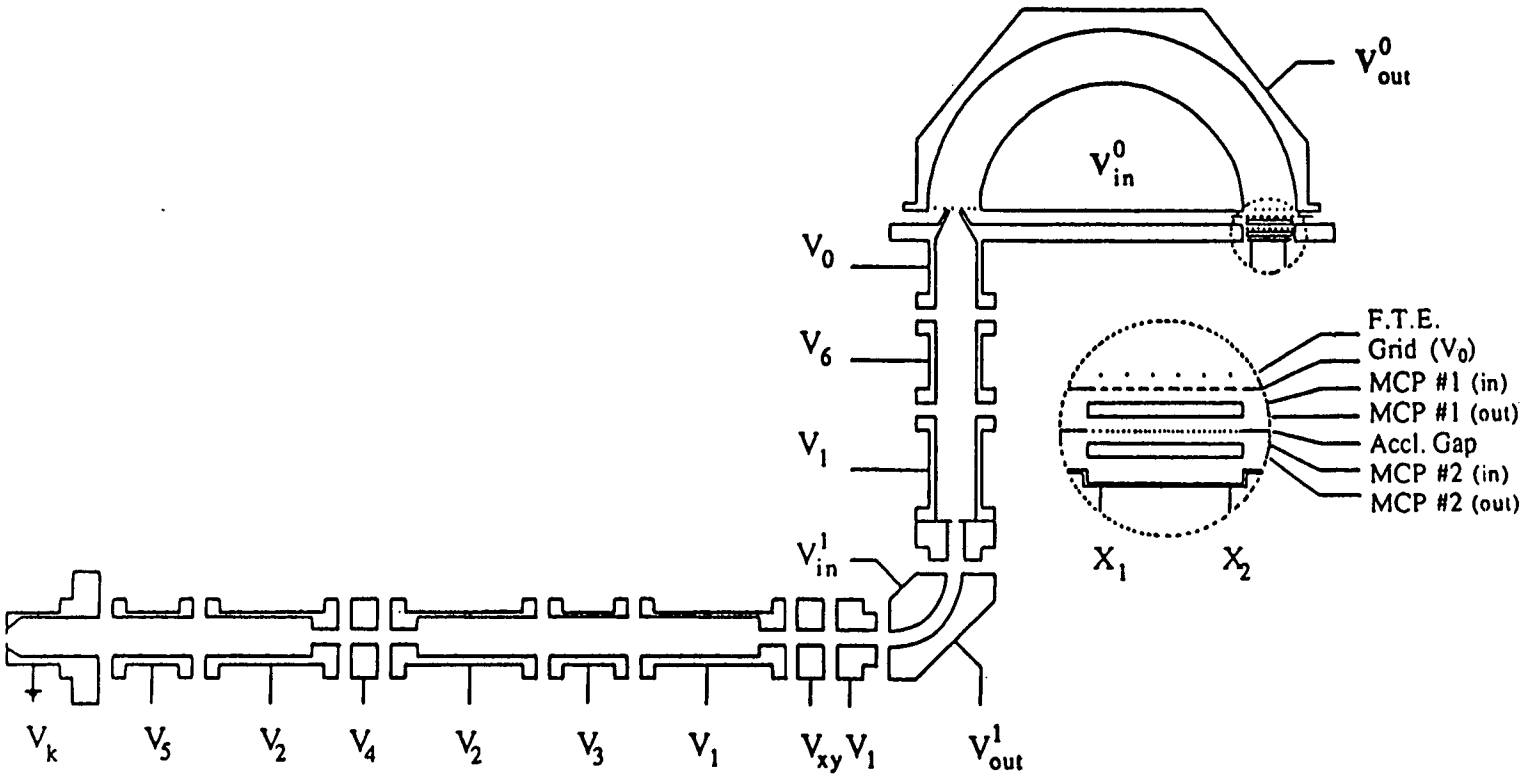
V^0_{out}
V^0_{in}
V_0
V_6
V_1
V^1_{in}
F.T.E.
Grid (V_0)
MCP #1 (in)
MCP #1 (out)
Accl. Gap
MCP #2 (in)
MCP #2 (out)
X_1
X_2
V_k
V_5
V_2
V_4
V_2
V_3
V_1
V_{xy}
V_1
V^1_{out}

Figure 2

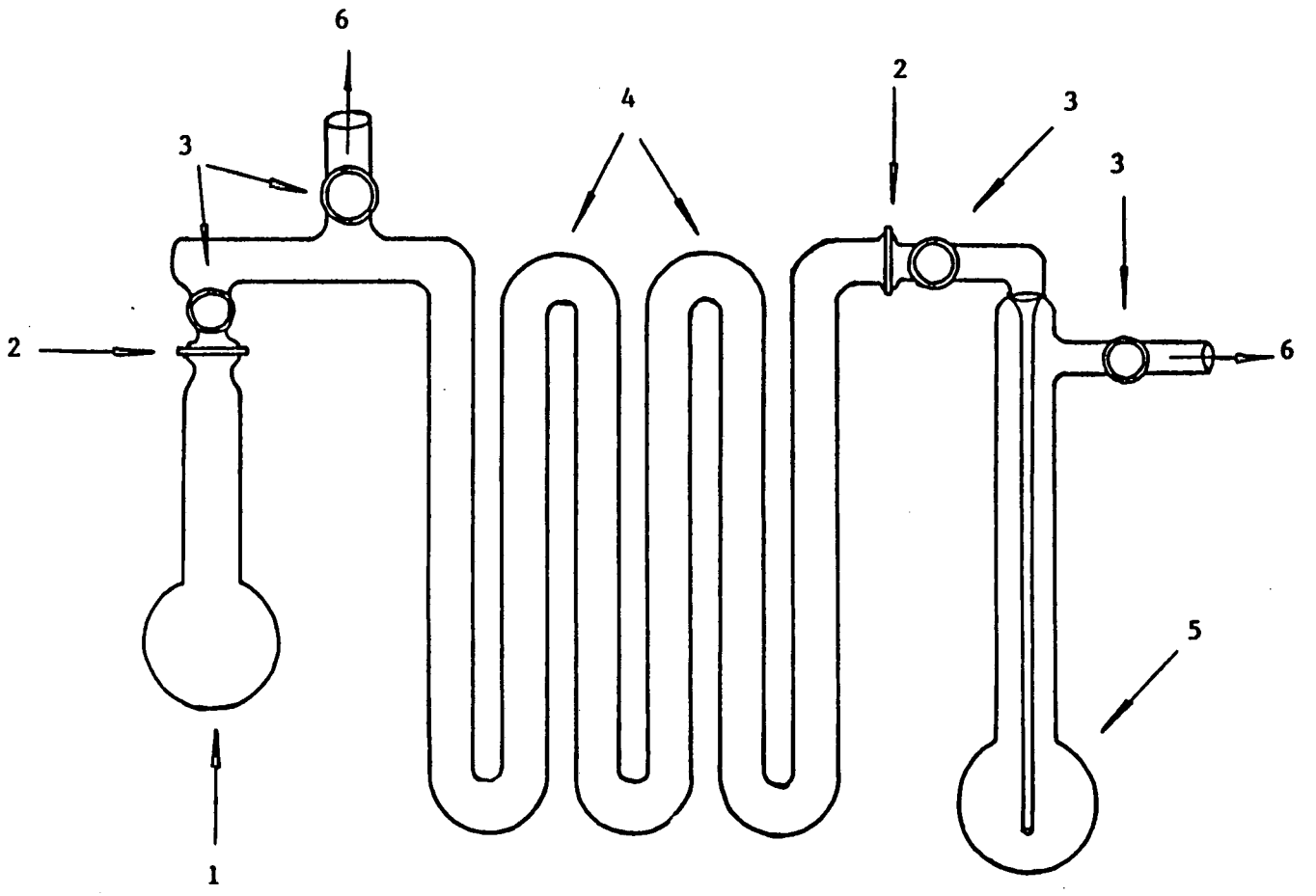

Figure 3

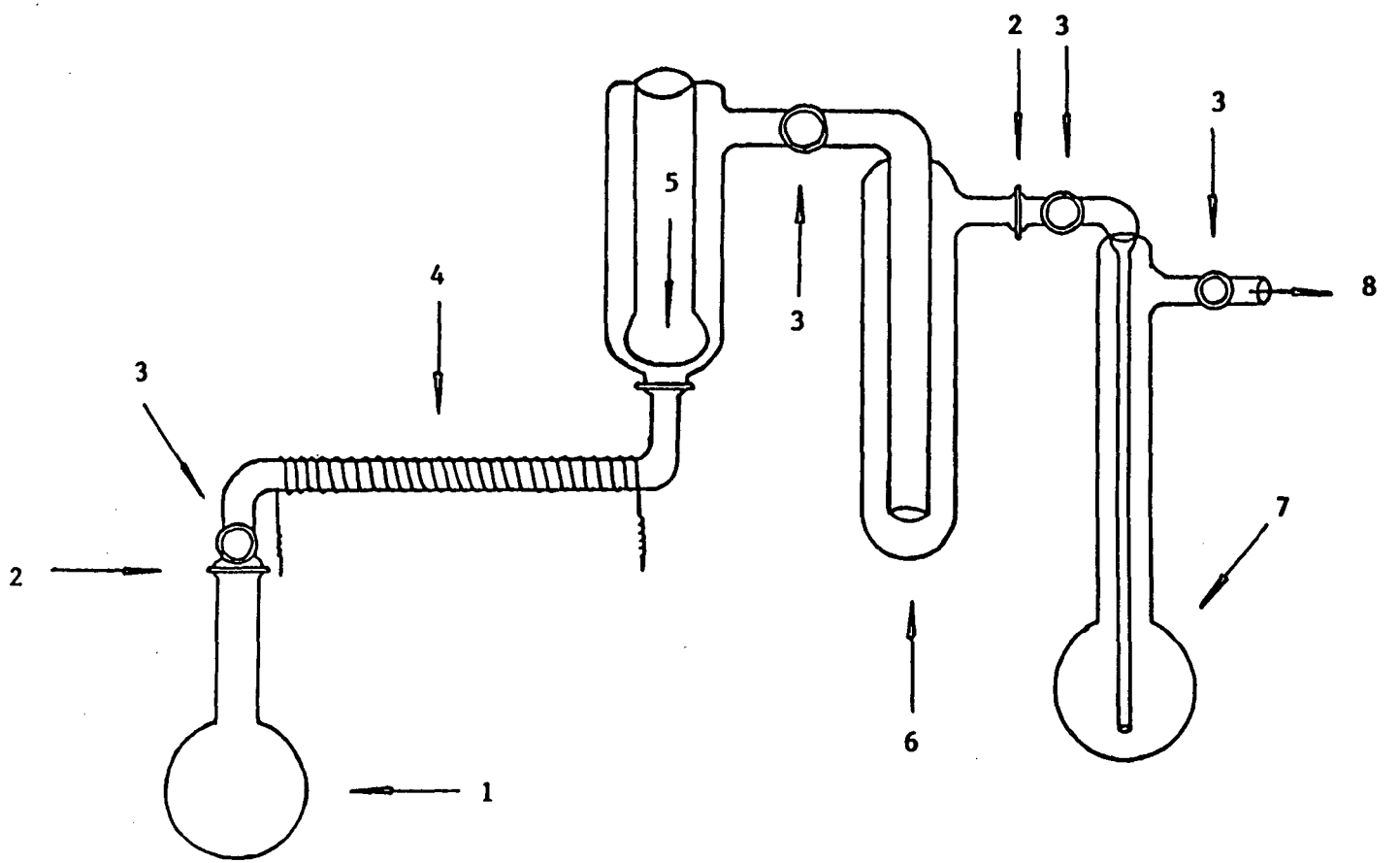

Figure 4

Chapter Three High Resolution Photoelectron Spectroscopy and Femtosecond Intramolecular Dynamics of H_2CO^+ and D_2CO^+

A. Introduction

The photoelectron spectra of H_2CO and D_2CO have been the subject of extensive theoretical and experiment studies.[1-10] Most of the theoretical studies have based on the earlier experimental studies by Turner et al.[1], and by Baker et al. [2] The assignment of the four outer most valence states' adiabatic ionization potentials by Turner et al. has been the subject of some theoretical calculations, especially on the ordering of the third and fourth ionic states. The vibrational fine structures observed in these low-resolution works have been studied extensively by theoretical calculations. [3-10] Although the vibrational fine structures seemed well resolved and relatively simple in most of the electronic states, their interpretation, however, has caused considerable difficulties. [1,2,11,12] Cederbaum [8] and coworkers used a many-body approach to the vibrational structures in formaldehyde, and cautioned that the vibrational coupling could be very different for different isotopic species. There were some disagreements between the theoretical and experimental results regarding the vibrational assignments. [13]

The stability and the decay pathways, and the dynamics of the formaldehyde ions formed by photoionization in various ionic states have also been studied both theoretically and experimentally. [14-17] In a photoionization study by Guyon et al., [14] they suggested that the decay of the first excited state $\tilde{A}\,^2B_1$ state produces the HCO^+ and CO^+ fragments. By using the correlation diagrams, they ascribed the production of the CO^+ ion to the electronic predissociation of the $\tilde{A}\,^2B_1$ state by an upper repulsive $^2A_1$ state leading to the $CO^+\,(^2\Sigma^+) + H_2\,(^1\Sigma_g^+)$ asymptote at 14.1 eV. They proposed that the $\tilde{A}\,^2B_1$ state was predissociated by the ground $\tilde{X}\,^2B_2$ State, whose lowest asymptote leads to $HCO^+\,(^1\Sigma^+)$ +

H (^2S) fragments. An ***ab initio*** calculation study by Pires et al., [18] gave some justification and explanations about the exact decay mechanism in the experimental observations by invoking a particular type of intersections between the potential energy surfaces: conical intersections. The fragmentation of the H_2CO^+ in $\tilde{A}\ ^2B_1$ state has also been studied by coincidence experiments [15-19]. It was determined that at $v = 6$, the formaldehyde ion in the $\tilde{A}\ ^2B_1$ state starts to fragment and yields $CO^+ + H_2$, and at $v = 7$, deuterated formaldehyde ion in the $\tilde{A}\ ^2B_1$ starts to fragment and yields $CO^+ + D_2$. [15]

In this work, we report the high resolution (FWHM 11 meV) helium **I**α photoelectron spectra of H_2CO and D_2CO. Improved resolution and effective cooling of the sample by the supersonic expansion enabled us to determine the adiabatic ionization potentials for the states ionizable by the helium **I**α line (21.21804 eV) to a much higher accuracy, and to give new interpretations on the vibrational structures observed in all ionic states. The results agree fairly well with available theoretical calculations. The observations that in the ground and first excited states of the H_2CO^+ and D_2CO^+ odd quanta of non-totally symmetric mode (ν_4) was excited, showed the possibility that the molecular ions in these electronic states might have non-planar equilibrium geometry. This was not discussed in any of the previously experimental and theoretical works. This was argued qualitatively by using the method first developed by R.S. Mulliken [20] and later by A.D. Walsh, [21,22] known as the Walsh diagram. Using the autocorrelation function formalism first discussed by Heller [23-26] for electronic photoabsorption and emission, and late by Lorquet et al. [27-29], and by Ruščić [28b] for photoelectron spectroscopy, modified by Pollard et al. [30] and Reutt et al., [31,32] the femtosecond ultra fast intramolecular dynamics of the formaldehyde cation in its various ionic states is discussed.

The details of the experiments are described in section B of this chapter. The vibronic coupling and isotope effects on vibronic couplings are discussed briefly in section

C. A description and the method for calculating the autocorrelation functions are presented in section D. Spectroscopic results and the dynamic interpretations based on the vibrational autocorrelation functions are discussed for each of the electronic states of H_2CO^+ and D_2CO^+ in section E. The major conclusions are summarized in section F.

B. Experiment

The molecular beam photoelectron spectrometer used for this study has been described in great detail by Pollard et al. [34] and by Reutt et al. [35] Briefly, it consists of a differentially pumped supersonic molecular beam source for the introduction of the sample into the main chamber where ionization takes place; a differentially pumped windowless helium discharge lamp optimized to produce only the helium Iα resonance line with minor contamination from higher resonance lines; a differentially pumped quadrupole mass spectrometer (QMS) to characterize the beam composition; a differentially pumped high resolution electron energy analyzer consisting of a 90° spherical sector prefilter, a 180° hemispherical analyzer equipped with a multichannel detector, and associated electron optics; and a dedicated microcomputer for data acquisition and control. The electrons are collected at a 90° angle with respect to the incident photon beam and the supersonic molecular, beam and the intensity is uncorrected for angular distribution effects. Formaldehyde ß values for helium Iα photons are not available, although there are angle-resolved photoelectron studies [33] on formaldehyde in the photon energy range 10 - 30 eV using synchrotron radiation, which gave the ß values for the $\tilde{X}\ ^2B_2$, $\tilde{A}\ ^2B_1$, $\tilde{C}\ ^2A_1$, and $\tilde{D}\ ^2B_2$ states at photon energy around 21 eV: 0.5, 0.5, 0.2, 0.3, respectively.

Approximately 300 torr of ultra high purity helium (99.9999 %, Matheson) was first passed through a U tube maintained at LN_2 to remove trace amount of water in the carrier gas line, then bubbled through liquid monomer H_2CO or D_2CO maintained at acetone/dry ice slush temperature (- 78 °C) with vapor pressures about 35 torr and 30 Torr

as measured with an **MKS** model 122AA-2000 Baratron. The monomer H_2CO or D_2CO was prepared following a literature procedure [36] by thermocracking paraformaldehyde and fully deuterated paraformaldehyde (**MSD** Isotopes, 99.9% D-atom) at approximately 120 °C, fractioning (at - 78 °C), trapping the monomer (at LN_2 temperature), and storing under dark at LN_2 temperature before use.

The He/H_2CO or He/D_2CO mixture with a total pressure of approximately 350 Torr was expanded through a 70 μm diameter converging molybdenum nozzle held at room temperature, skimmed by a 0.858 mm diameter, 6.4 mm tall conical stainless steel skimmer, D_{ns} = 6.4 mm. The beam source chamber pressure was 6×10^{-5} torr, and the main chamber pressure was 3×10^{-6} torr during the experimental measurements. All gas inlet lines were minimized and extensively baked (200 °C) under vacuum (10^{-7} torr) to remove trace amounts of water which is known to catalytically polymerize formaldehyde. Beam compositions were checked by the quadrupole mass spectrometer. No polymers of H_2CO or D_2CO were found under these experimental conditions. The rotational temperature in the beams was estimated to be <10 K as shown by **LIF** measurements under similar conditions. [37]

The complete photoelectron spectrum of each isotopic species was obtained as four sequential scans of the electron kinetic energy. Each scan was preceded and immediately followed by an argon calibration scan. To enhance statistics, four complete spectra of H_2CO were scanned and summed. Thus the reported photoelectron bands each represent the summation of four scans. Individual scans were made within a time period of less than two hours. The presented D_2CO photoelectron bands were the summation of four such scans as well. Restricting the length of each scan limits the total drift in the electron kinetic energy scale to ≤ 1 meV. The linearity of the kinetic energy scale was determined by obtaining the N_2^+ photoelectron spectrum and comparing the N_2^+ $\tilde{X}\,^2\Sigma_g^+$ v=0 and $\tilde{B}\,^2\Sigma_u^+$ v=0 splitting with the accurate literature value of 3.16981 eV available from N_2^+ optical emission

spectroscopy. [38] At higher kinetic energies, the linearity of the energy scale was checked by the photoelectron spectra of argon and xenon. The ionization potential of these rare gases (I.P. Ar $^2P_{3/2}$ = 15.75975 eV, and Xe $^2P_{3/2}$ = 12.13000 eV) have been precisely determined from optical spectroscopy.[39] The linearity of the molecular beam spectrometer is within ±1.0 meV over this entire energy range. The combination of the drift and the linearity of the energy scale errors limits the accuracy at which the absolute ionization potential may be reported to ± 3.0 meV. Other spectroscopic constants, however, are obtained as line splittings and may be reported to a much higher accuracy of ± 0.5 meV.

C. Vibronic Coupling and Isotope Effects on Vibronic Coupling

In photoelectron spectroscopy, the vibronic coupling effect , that is the interaction of the electronic and nuclear (vibrational) motion, is often invoked to explain the observations that there are vibrational progressions in modes that are not allowed by the selection rules based on the **Born-Oppenheimer** approximation; [40] that the observed vibrational frequencies are very low; and that odd quanta of non totally symmetric vibrations get excited. There are other couplings and resonance effects that can also cause similar effects, like vibrational-rotation coupling, rotation-electronic couplings and **Fermi** resonances. In general, these effects are much smaller than the vibronic coupling effect and are much easier to identify.

The vibronic coupling effects are usually treated as perturbations to the **Born-Oppenheimer** approximation, that is the adiabatic, Hamiltonian $\mathcal{H}_0$. [41] We can expand the molecular Hamiltonian $\mathcal{H}(q;Q)$, which is a function of the electron q and the nuclear Q coordinates, with a Taylor series in the normal coordinates of vibrational Q near the equilibrium configuration Q_0:

$$\mathcal{H} = \mathcal{H}(q;Q)_{Q_0} + \sum_{r=1}^{\infty} \left| \frac{1}{r!} \frac{\partial^r \mathcal{H}(q;Q)}{\partial Q^r} \right|_{Q_0} Q^r + \cdots \tag{3.1}$$

The first term in equation (3.1), $\mathcal{H}(q;Q)_{Q_0}$, is called the zero-order Hamiltonian, that is the **Born-Oppenheimer** adiabatic Hamiltonian, and is usually expressed as $\mathcal{H}_0$. Applying the total Hamiltonian $\mathcal{H}$ to the molecular wave function Ψ yields:

$$<\Psi|\mathcal{H}|\Psi> = E_0 + E_1 + E_2 + \ldots \tag{3.2}$$

Where E_0 is the non-perturbed energy, and E_1, E_2 are the perturbation energies resulting from the linear and quadratic expansion terms in equation (3.1) respectively. The coupling of two wave functions Ψ_k and Ψ_j can be expressed according to the matrix elements:

$$<\Psi_k|\mathcal{H}|\Psi_j> \tag{3.3}$$

which can be expanded with the Hamiltonian $\mathcal{H}$ of equation (3.1),

$$<\Psi_k|\mathcal{H}|\Psi_j> = <\Psi_k|\mathcal{H}_0|\Psi_j> + \sum_r Q_r \langle\Psi_k\left|\frac{\partial\mathcal{H}}{\partial Q_r}\right|\Psi_j\rangle +$$

$$+\frac{1}{2!}\sum_r Q_r^2 \langle\Psi_k\left|\frac{\partial^2\mathcal{H}}{\partial^2 Q_r^2}\right|\Psi_j\rangle + \frac{1}{2!}\sum_{rs} Q_r Q_s \langle\Psi_k\left|\frac{\partial^2\mathcal{H}}{\partial Q_r \partial Q_s}\right|\Psi_j\rangle + \ldots \tag{3.4}$$

The first term in equation (3.4) is always zero by the orthogonality relationship. Thus the necessary condition for the vibronic coupling effects to perturb the electronic states involved is that at least one term in the equation (3.4) has a nonzero value that is not too small compared with the zero-order electronic states' energy separations.

The total Hamiltonian $\mathcal{H}$ of equation (3.1) always possesses the full symmetry (Γ_1) of the molecular point group. This is also true for $\mathcal{H}_0$, the Hamiltonian for the zeroth-order unperturbed molecule. For the coupling operators in equation (3.4): $\partial\mathcal{H}/\partial Q_r$ transforms as the irreducible representation of the normal coordinate Q_r, $\Gamma(Q_r)$; $\partial^2\mathcal{H}/\partial^2 Q_r$

always has at least one component that transforms as Γ_1, the full symmetry of the molecular point group; and $\partial^2\mathcal{H}/\partial Q_r\partial Q_s$ transforms as $\Gamma(Q_r)\otimes\Gamma(Q_s)$. The linear coupling integral in equation (3.4) will be finite if the product of the representations of all species in the integral contains the totally symmetric representation, Γ_1, that is:

$$\Gamma(\Psi_k)\otimes\Gamma(\Psi_j)\otimes\Gamma(\partial\mathcal{H}/\partial Q_r) \subset \Gamma_1. \tag{3.5}$$

This will enable the Q_r normal vibrational mode to couple and mix the Ψ_k and Ψ_j electronic states. If Ψ_k and Ψ_j are degenerated states, then Q_r is the asymmetric vibrational mode that will remove the degeneracy. We can discuss the two quadratic terms in equation (3.4) similarly. The linear terms are usually much larger than the quadratic terms, and the quadratic terms are normally neglected when the linear terms are nonzero. In a polyatomic molecule, there could be more than one normal mode Q_r that satisfy the condition of equation (3.5). Those normal modes that satisfy equation (3.5) are called vibronically active modes. When there are more than one mode that are vibronically active, multimode vibronic coupling effects will occur In general, these are more complicated to deal with. Multimode vibronic coupling effects and their influence on spectroscopy have been reviewed in detail by Köppel et al. [42]

It can be seen from equation (3.4) that both the linear and quadratic vibronic couplings depend on the normal coordinates that are mass-dependent. It is expected that the couplings will be different for isotope-substituted compounds in the same electronic state. One important consequence of this effect is that it is possible for different vibrational modes to be excited to a different extent for isotope-substituted compounds. Theoretical calculations have shown that these effects appear in the isotope-substituted compounds. [36] The H_2CO^+ and D_2CO^+ photoelectron spectra in their first and second excited states do show this kind of behavior, and they will be discussed further in section E of this chapter.

D. The Correlation Function

The autocorrelation function formalism description of the intramolecular dynamic process gives complementary information to time-dependent measurements. Lorquet et al. [27-29] first demonstrated how this can be done for photoelectron bands using the formalism of Heller. [23-26] A variation on the method of Lorquet et al. was used by Pollard et al., [30] and by Reutt et al. [31,32] to study the dynamic characteristics of intramolecular processes using supersonic molecular beam photoelectron spectroscopy. Ruščić [28b] has also given the analytical form of the vibrational autocorrelation function for photoelectron bands under the harmonic approximation for vibrational motions.

Very recently, Remacle et al. [29] have suggested that there exists a relationship between the vibrational autocorrelation function **C**(t) and the population decay function **P**(t) of a particular electronic state. They defined an average population decay curve $\mathbf{P}_{av}(t)$ valid in a particular time period, and $\mathbf{C}_{av}(t)$, the average correlation function, obtained from C(t). It was pointed out by the authors that for a specific excitation, the exact initial rate of decay of $\mathbf{P}_{av}(t)$ (valid up to the dephasing time T_1) is equal to the initial rate of decay of $|C(t)|^2$, and the subsequent time evolution of $\mathbf{P}_{av}(t)$ can be obtained by averaging $|C(t)|^2$ over its oscillation to give $|C_{av}(t)|^2$. To a good approximation, the average population decay curve $\mathbf{P}_{av}(t)$ can be obtained by multiplying $|C_{av}(t)|^2$ with an appropriate constant; i.e., the slopes of the two curves are the same.

The autocorrelation function can be expressed as

$$C(t) = |\langle\phi(0)|\phi(t)\rangle|. \tag{3.6}$$

Here $\phi(0)$ is the initial nuclear wavefunction, and $\phi(t)$ is the time evolution of this wavefunction on the excited state potential energy surface. C(t) represents the probability amplitude that at time t the system remains in the initially prepared state. It must be noted

that the correlation function is the measure of the time evolution of the initial wave packet on the excited state potential energy surface and not a measure of the excited state population. But as mentioned in the preceding paragraph, the initial decay rate of **C**(t), through $|\mathbf{C}(t)|^2$, is the same as the average population $\mathbf{P}_{av}(t)$ initial decay rate. It is dominated by the dephasing of the initial wave packet due to the different shape of the excited-state potential energy surface. Only at times greater than a vibrational period will radiationless decay processes appear in the correlation function time evolution. The derivation of the autocorrelation function **C**(t) from photoelectron spectroscopy experimental data has been reported; only the principal points will be outlined here. The form of photoionization cross section under the strict **Franck-Condon** approximation [40] can be expressed as

$$\sigma(E) \propto \left| |M_{el}(Q,E)|^2 |\langle \Psi'' | \Psi' \rangle|^2 \right| \tag{3.7}$$

Here $\mathbf{M}_{el}(Q, E)$ is the pure electronic transition moment, a function of the nuclear coordinates Q and electron kinetic energy E, and Ψ'' and Ψ' are the initial- and final-state vibrational wave functions. The electronic transition moment varies slowly over the photoelectron band. In lieu of any arbitrary approximation, a constant value was used in calculating the correlation functions reported here.

Applying the completeness on a set of eigenstate Ψ'' of the molecular Hamiltonian and invoking the analytical form of the Dirac δ function, it has been shown [28a] that the cross section of photoionization becomes

$$\sigma(E) \propto \frac{1}{2\pi} \int_{-\infty}^{+\infty} e^{iEt/\hbar} \langle \Psi'' | e^{-i\mathcal{H}t/\hbar} | \Psi'' \rangle \, dt \tag{3.8}$$

Here $\mathcal{H}$ is the molecular Hamiltonian, Ψ'' is identified as the initial nuclear wave function $\phi(0)$, and $e^{-i\mathcal{H}t/\hbar}|\Psi''\rangle$ is the nuclear wave function at time t: $\phi(t)$. This gives

$$\sigma(E) \propto \frac{1}{2\pi} \int_{-\infty}^{+\infty} e^{iEt/\hbar} \langle\phi(0)|\phi(t)\rangle \, dt \tag{3.9}$$

and the correlation function can be obtained by a **Fourier** transformation of the cross section

$$C(t) = |\langle\phi(0)|\phi(t)\rangle| \propto \frac{1}{2\pi} \int_{-\infty}^{+\infty} \sigma(E)\, e^{-iEt/\hbar} \, dt \tag{3.10}$$

It can be seen from this equation that the correlation function can be obtained from the **Fourier** transform of the photoelectron partial cross section $\sigma(E)$. This can be accomplished by deconvoluting the instrument response function $\mathbf{I}(E)_{ir}$, which we determine from the photoelectron spectrum of a rare gas at a kinetic energy comparable to the band of interest, from the quantity $\mathbf{I}(E)$, intensity vs. energy, which we measure in photoelectron spectroscopy. The contributions of the finite rotational temperature in a supersonic molecular beam experiment (typically ~ 5-10 Kelvin) and the rotational excitations contribution to the correlation function were removed by convoluting $\mathbf{I}(E)_{ir}$ with a gaussian function $\mathbf{I}(E)_g$ to generate a rotationally broadened instrument response function. The width of the gaussian function was chosen from the average rotational constant , $\mathbf{B}_{avg}$, of the molecular ion for the particular electronic state (if available), the finite rotational temperature, and the rotational selection rules for photoionization. Ruščić has taken a different approach to account for all the corrections. However, both methods give essentially the same results in the time window of interest.

The procedure for calculating the correlation function of $\tilde{X}$, $\tilde{A}$, $\tilde{B}$, and $\tilde{C}$ states of formaldehyde and d_2-formaldehyde is the following. First, the band of interest was isolated (in the case of B and C states, they were digitally separated to remove the overlapping of these two bands), and the empirically determined background, plus any constant background, was then removed. The resulting band was then normalized (area = 1) and **Fourier** transformed using a discrete **FFT** algorithm. [43] The instrument response function was similarly normalized and convoluted with a Gaussian of 6.5 meV (FWHM). The resulting function was **Fourier** transformed and divided into that of the data. Finally, the modulus of the previous result was calculated, which gave the correlation function. The procedure can be summarized by the following equation:

$$C^{vib}(t) = |\langle\phi(0)|\phi(t)\rangle| = \left| \int_{-\infty}^{+\infty} \mathbf{I}(E)\, e^{-iEt/\hbar}\, dE \right| \div \left| \int_{-\infty}^{+\infty} \mathbf{I}(E)_{ir}\, e^{-iEt/\hbar}\, dE \;\mathrm{X}\; \int_{-\infty}^{+\infty} \mathbf{I}(E)_{g}\, e^{-iEt/\hbar}\, dE \right| \qquad (3.11)$$

Then $|C(t)|^2$ was calculated, and $|C_{av}(t)|^2$ was evaluated by fit $|C(t)|^2$ with an exponential curve of the form Ae^{-ikt} for both the initial drop and the subsequent decaying after the first 'vibrational' period.

E. Results and Discussions

The full spectra of H_2CO and D_2CO obtained by combining four separate scans with a resolution of 11 meV FWHM (as measured with Ar) are shown in Figure 1, and Figure 2, respectively. Table I summarizes the measured spectroscopic constants together with results reported in the literature. [47,48]

1. First Band, $\tilde{X}\ 1^2B_2$ state

The ground states of both H_2CO^+ and D_2CO^+ have well-resolved vibrational fine structures, as shown separately in Figure 3 and Figure 4. Observed spectroscopic results are presented in Table II. In the present work, effective rotationally cooling enables all of the observed vibrational levels to be determined with improved accuracy and the mean energies of these transitions were determined by the following least-squares fitting procedure. The adiabatic transitions (or the most intense feature) were first determined by fitting these features to Gaussians. The adiabatic peaks were then isolated and used as empirical functions to fit the successive vibrational levels. This procedure allows the values of peak splittings to be determined to an accuracy of $\leq \pm$ 0.0005 eV. The mean transition energies located through this procedure are listed for each of the bands observed. The vibrational levels for each normal mode were then least-squares fitted to the standard energy level expression of a **Morse** oscillator [46a,46b]

$$G_i^0(v) = \omega_i^0 v - \omega_i^0 x_i^0 v^2 \qquad (3.12)$$

with the zero point energy being set to zero, ω_i^0 and $\omega_i^0 x_i^0$ are related to ω_i and $\omega_i x_i$ in the following ways: $\omega_i = \omega_i^0 + \omega_i^0 x_i^0$ and $\omega_i^0 x_i^0 = \omega_i x_i$. Here ω_i is the fundamental vibration frequency in cm^{-1} and $\omega_i x_i$ is the quadratic anharmonicity constant for the ith normal vibrational mode.

From the results, we conclude not only that all three totally symmetric vibrational modes were excited, but that agrees with the theoretical calculations by Domcke et al., [8] not with the results of the calculations by Takeshita [13], but also that the non-totally symmetric mode ν_4 was excited. The excitation of odd quanta of the ν_4 mode is an indication that the molecular ion might have an equilibrium geometry other than planar. This can be argued

qualitatively using the Walsh diagram approach and compared very favorably with the electronic absorption spectrum correspond to the transition of $\tilde{A}\ ^1A_2 \leftarrow \tilde{X}\ ^1A_1$ in the UV absorption spectrum. In the photoelectron spectrum, this corresponds to the removal of an electron from the b_2 (n_O) orbital, thus reducing the stabilization energy gained by having two electrons in the planar form. This also reduced the repulsion between the hydrogen atoms and the oxygen atom. There are MO calculations [13,44] indicating that in the $\tilde{X}\ ^2B_2$ state of the H_2CO^+, the HCO angle decreases slightly (~ 5°) from the neutral molecular $\tilde{X}\ ^1A_1$ state. From their ***ab initio*** calculation results [45], Buenker and Peyerimhoff concluded that molecules with 10 and 11 valence electrons are less strongly planar compared to those with 12 upon removal of electrons from the n species that are the non-bonding orbitals. But we expect the deviation from the planar equilibrium geometry to be very small.

The vibrational progressions in the observed spectra confirmed the earlier ***ab initio*** calculations with a many body approach by W. Domcke et al., [8] but disagree with the ***ab initio*** calculations by Takeshita [13] concerning the excitation of the ν_1 mode. The anharmonicity would be too big for ν_2 if we assign the feature that appeared at 11.2086 eV to be the $\nu_2 = 2$ peak, according to Takeshita. It is noteworthy that different vibrational modes get excited to different extents between formaldehyde and deuterated formaldehyde. This gave some indications that the ionic ground state potential energy surfaces could be quite different for these isotopic compounds even if the neutral ground state potential energy surfaces might not be much different.

The vibrational autocorrelation function calculated using the formalism and procedure described in section D for the $\tilde{X}\ 1^2B_2$ states of H_2CO^+ and D_2CO^+ are presented in Figure 5 and Figure 6, respectively. The complex beat pattern of the $|C(t)|^2$ curve is the result of four different vibrational modes, after the initial drop, all having different phase and probably all having different phase space distances to travel as well. But the overall

monotonic decay trend in these $|C_{av}(t)|^2$ curves does indicate that the $\tilde{X}\ 1^2B_2$ state is in a stable configuration in the **Franck-Condon** region accessible by the photoionization event. It should be noticed that there were no deep minimums in the correlation functions, which are charateristics of a wave packet prepared through a predominately adiabatic transition. The initially prepared wave packet is mostly localized around the minimum of the upper potential energy surfaces, and weakly oscillates around this region, retaining substantial correlation at all times. The absence of the return of major oscillation strength can be attributed to the excitation of many modes which all having different phases after the initial drop and all having different phase spaces to travel.

2. Second Band, $\tilde{A}\ ^2B_1$ State

The second bands of H_2CO^+ and D_2CO^+ are shown in Figure 7 and Figure 8, separately. The vibrational progressions observed are summarized in Table III. Here the small $N_2^+\ \tilde{X}$ peak presented in the D_2CO^+ spectra, resulting from the main chamber background, makes the absolute IEs reportable to an accuracy of ±1.0 meV which is limited by the energy scale drift during the scans. It ought to be noted that the vibrational couplings are different for H_2CO^+ and D_2CO^+. In H_2CO^+, the major vibrational excitation is the ν_2 mode together with several quanta of ν_3 excited as well. In D_2CO^+, on the other hand, the major vibrational excitation is the ν_2 mode, but the coupling is different between vibrational modes: here it is the ν_1 mode that gets excited along with the major excitation of the ν_2 mode. These agree fairly well with the theoretical calculations by Domcke et al. [8] when many-body effects are included, and did not agree with the ***ab initio*** calculations by Takeshita with a Roothaan's restricted **Hartree-Fork** approach. In Domcke et al.'s calculation for both isotopic species, the coupling of the ν_2 modes are very strong. They are 2.792 and 2.611 for H_2CO^+ and D_2CO^+, respectively. The coupling of ν_3 (0.270) is much stronger than that of ν_1 (0.036) in H_2CO^+, while in D_2CO^+ the coupling of ν_1

(0.414) is much stronger than that of ν_3 (0.011). Also, the length of the vibrational progressions is slightly different, H_2CO^+ has a slightly shorter progression than D_2CO^+ (in the case of D_2CO^+, the $\tilde{A}$ state vibrational progression would extend to $\nu_2 = 10$ if it were not obscured by the $N_2^+ \tilde{X}$ state peak). This is an indication that the ionic potential energy surfaces are slightly different for the isotopic compounds.

The difference in vibrational excitations has its origin in the different vibronic coupling coefficients (also called vibrational couplings by Domcke et al. [8]) for the isotopic compounds as discussed in section C of this chapter. As pointed by Domcke et al. [8] in their ***ab initio*** many-body approach calculations, the vibrational coupling can be very different for isotopic compounds, since the coupling coefficients are mass-dependent (the kinematic matrix, that transforms from normal to internal coordinates, of D_2CO differs considerably from that of H_2CO). It is expected that different vibrational modes will be excited to different extent for isotopic molecules. This also indicates that parts of the ionic potential energy surfaces of the $\tilde{A}\,^2B_1$ state accessible by the photoionization excitation for H_2CO^+ and D_2CO^+ are different, especially along different normal coordinates.

The strong excitation of the ν_2 mode is an indication that a strongly bonding electron is being ejected. This agrees with previous experimental and theoretical results. But the appearances of the odd ν_4 mode with very weak intensity, just as in the ionic ground state, is an indication that the molecular ions might have a nonplanar equilibrium geometry in the $\tilde{A}\,^2B_1$ state. This could be especially important in D_2CO^+, where the $\nu_4 =$ 1, 2 peaks are comparably stronger than in H_2CO^+. Just as in their ionic ground states, the deviation from the planar equilibrium geometry in the $\tilde{A}\,^2B_1$ state is expected to be very small.

The vibrational autocorrelation functions for the $\tilde{A}\,^2B_1$ state of H_2CO^+ and D_2CO^+ after corrections for the instrument response function and rotational broadening are shown

in Figure 9 and Figure 10. The overall shapes of the correlation function for H_2CO^+ and D_2CO^+ is very similar, showing only one major progression with a period of about 28.5 fs, which is the vibrational period of the ν_2 mode. But differences are to be noted as well. In the case of H_2CO^+, the correlation function retains its major oscillation up to about 170 fs. Beyond that, the wave packet spreads out and multiple peaks appear in the correlation function. In D_2CO^+, the correlation function retains its major oscillation up to almost 300 fs. The correlation strength in C(t) is also much smaller in $H_2CO^+ \sim 0.58$, compared with $D_2CO^+ \sim 0.74$. Also, the peaks in the D_2CO^+ correlation function are much sharper than those in the H_2CO^+ correlation function. The observed differences in the appearance of the correlation function gave us some indications about the differences in the ionic potential energy surfaces between H_2CO^+ and D_2CO^+. First, the anharmonicity, which is known to cause the spreading of the correlation function peaks, must be smaller in D_2CO^+ than in H_2CO^+ along the Q_2 normal coordinates. In fact the anharmonicity constants are 10.0 cm^{-1} and 5.7 cm^{-1} for H_2CO^+ and D_2CO^+, respectively. Second, D_2CO^+ in the $\tilde{A}\,^2B_1$ state is more tightly bonded than H_2CO^+: the correlation function of D_2CO^+ retains a higher degree of correlation in longer times, and this could also imply that the initial wave packet of D_2CO^+ spans a relatively smaller portion of the phase space on the upper potential energy surface.

The modulations of the correlation function were caused by two sources. The first one is the small spin-orbital splittings in this band, since it is a π bonding orbital electron that was ejected. The FWHM for peaks in this band was close to 12.5 meV, which implies that the spin-orbital splitting is $\leq$ 2 meV. The second is the excitation of additional vibrational modes other than ν_2 in both H_2CO^+ and D_2CO^+. This gives the doublet- and multiplet-like structures in the photoelectron spectra that produce a beat pattern that modulates the correlation function. After removing these two effects by the method of

Lorquet,[28a] that involved dividing the C(t) obtained with $|\cos\Omega t/2\hbar|$, the values of Ω were chosen to give an overall monotonic decay C(t) by carefully removing the singular points in the cosine functions. The corrected vibrational autocorrelation functions of the $\tilde{A}\,^2B_1$ state of H_2CO^+ and D_2CO^+ are shown at the bottom of Figure 9 and Figure 10 in forms of $|C(t)|^2$. The $|C_{av}(t)|^2$ fittings of the $|C(t)|^2$ were also included there.

It can be seen from Figure 9 and Figure 10 that the overall decay behavior of H_2CO^+ and D_2CO^+ in the $\tilde{A}\,^2B_1$ state is very similar, but the isotope effect does manifest itself in that D_2CO^+ has a relatively much slower decay rate after the initial dephasing than H_2CO^+, and the initial dephasing rates are different as well. As pointed by Ruščić[28b], this initial (before the first half vibrational period) dephasing rate depends very sensitively on the differences between the ionic state and the neutral ground state equilibrium geometries. This is yet another possible indication that in the $\tilde{A}\,^2B_1$ state of H_2CO^+ and D_2CO^+, the equilibrium geometries might be slightly different from the planar ones. The wave packet is displaced substantially from the minimum of the upper potential energy surface which is consistant with the observed long vibrational progressions, and indicating a strong bonding electron being ejected. The wave packet oscillated with large amplitude on the upper potential energy surface which accounts for the deep minimums in the correlation functions. The time window, over which we could deduce useful information on the intramolecular dynamics was limited by the finite resolution achievable. As shown in this state after removal of all the possible broadening effects, the time window was about 200 to 300 fs wide. This corresponds to an effective resolution of $\leq$ 3 meV, which is to be compared with the estimated helium Iα resonance line width produced by the lamp, to be $\leq$ 2 meV.

3. Third Band, $\tilde{B}\,^2A_1$ State

The third bands of H_2CO^+ and D_2CO^+ are shown in Figure 11 and Figure 12. The

vibrational progressions observed are summarized in Table IV. The presence of the small Ar^+ peaks in the H_2CO^+ band, resulting from the main chamber background from frequent calibration runs, makes the absolute IEs for this band reportable to an accuracy of ±1.0meV, as discussed in the discussion of the $\tilde{A}\ ^2B_1$ band of D_2CO^+. As we have pointed out in the discussion of the $\tilde{A}\ ^2B_1$ band, the vibrational couplings are different for different isotopic compounds. In previous experimental and theoretical studies, it was concluded that the simplicity of this band in H_2CO^+ was due to the accident degeneracy of the ν_2 and ν_3 normal vibrational modes. The removal of this degeneracy in D_2CO^+ was used as evidence for this interpretation.

The ν_2 vibrational frequency is 1304.5 cm^{-1} for H_2CO^+ and 1311.1 cm^{-1} for D_2CO^+ as obtained for this state from the present study. The ν_3 vibrational frequency, as determined from this band of D_2CO^+, is 957.4 cm^{-1}, for H_2CO^+ is 1304.5 cm^{-1} (assuming here $\nu_3 = \nu_2$). This reduction upon deuteration seems reasonable when compared with the neutral $\tilde{X}\ ^1A_1$ ground state of H_2CO^+ and D_2CO^+ with ν_3 = 1500.2 cm^{-1}, and 1105.7 cm^{-1} respectively. The FWHM in the spectra shown for H_2CO^+ and D_2CO^+ is about 12 meV, which is very close to the measured instrumental resolution. Unless ν_2 and ν_3 were truly degenerate to within 1 meV or less, we would have seen the broadening of the peaks in H_2CO^+. Upon close examination, it is the other way around, however, the peaks in D_2CO^+ are slightly broader than those in H_2CO^+. Theoretical calculations [8] indicate that in the $\tilde{B}\ ^2A_1$ state of H_2CO^+, the coupling of ν_3 (0.301) is much weaker than that of ν_2 (1.156). In D_2CO^+, the coupling of ν_3 is slightly larger (0.855) than that of ν_2 (0.765) when many body effects are included, according to these authors. It is possible that the coupling of ν_3 in the $\tilde{B}\ ^2A_1$ state of H_2CO^+ is so weak that we are actually seeing only the progression of the ν_2 vibration. While in the $\tilde{B}\ ^2A_1$ state of D_2CO^+ both ν_3 and ν_2 are coupled strongly, both vibrational progressions are seen. We thus tentatively assigned the vibrational progressions in the $\tilde{B}\ ^2A_1$ state of H_2CO^+ to the ν_2 mode only. The present

assignment and the observed **AIEs, VIEs** and vibrational progressions definitely support the assignment of Brundle et al. [12] and all theoretical calculations [3-13] available that this band is the $\tilde{B}\,^2A_1$ state of formaldehyde.

The vibrational correlation functions for the $\tilde{B}\,^2A_1$ state of H_2CO^+ and D_2CO^+, calculated by digitally remove the $\tilde{C}\,2^2B_2$ bands' contributions, are shown in Figure 13 and Figure 14. It can be seen from Figure 13 that for H_2CO^+, there is only one major progression, with a period of ~ 40 fs. The anharmonicity starts to spread the correlation function around t = 100 fs. The slow decay of the correlation function indicates that this state is in a very stable configuration regarding deformations along the Q_2 normal coordinate. In the case of D_2CO^+, it can be seen that this state is in a very stable configuration regarding deformations along both the Q_2 and the Q_3 normal coordinates. The overall rate of decay as shown by the $|C_{av}(t)|^2$ of both isotopic compounds, is very similar qualitatively. Quantitatively speaking, in this electronic state D_2CO^+ is more stable than H_2CO^+. In D_2CO^+, the excitation of both the ν_2 and ν_3 mode gives rise to the doublet- and multiplet-like structures in the photoelectron spectrum. These doublet and multiplet structures in the energy domain, when **Fourier** transformed give rise to the beat pattern observed in the correlation function, as discussed in previous section, and was not corrected for this band. It is to be noted here that the initial rates of decay for H_2CO^+ and D_2CO^+ in this state are very different, indicating, again, possibly very different potential energy surfaces for H_2CO^+ and D_2CO^+ in the $\tilde{B}\,^2A_1$ state. The deep valleys in the correlation functions, as discussed in previous section of the $\tilde{A}\,^2B_1$ state correlation function, indicate a substantially displaced wave packet from the upper potential energy minimums.

4. Fourth Band, $\tilde{C}\,2^2B_2$ State

The fourth band of H_2CO^+ was shown in Figure 11, together with the $\tilde{B}\,^2A_1$ state.

The $\tilde{C}\ 2^2B_2$ state of D_2CO^+ is shown separately in Figure 15. Even with sufficient supersonic cooling in the present high resolution study, the complexity of this band for both H_2CO^+ and D_2CO^+ cannot be fully untangled. The vibrational assignment could only be regarded as tentative, especially in the case of D_2CO^+. As pointed out by Turner et al. in their original studies, this complexity might have been caused by the crossing of another repulsive state with the $\tilde{C}\ 2^2B_2$ state. Theoretical calculations do indicate that the density of the electronic states increase rapidly with the energy. In the energy range 16.4-17 eV (where the fourth band appears in the photoelectron spectrum) above the ground state of the neutral molecule, four electronic states are present and their potential energy surfaces intersect. [18] In H_2CO^+, the major progressions are assigned to the excitations of ν_1 and ν_3 modes, based largely on the many-body calculations by Domcke et al. [8] The adiabatic ionization potential was tentatively assigned as **AIE** = 16.2395 eV. In D_2CO^+, the major progressions are much weaker compared with the corresponding ones in H_2CO^+, and were assigned to ν_1, ν_2, and ν_3 modes. The adiabatic ionization potential, however, can only be estimated to be $\leq 16.435 \pm 0.02$ eV.

The vibrational correlation functions for the $\tilde{C}\ 2^2B_2$ state of H_2CO^+ and D_2CO^+ are presented in Figure 16 and Figure 17, respectively. The major feature of the correlation functions for this band is the extremely fast loss of correlation strength as manifested by the correlation functions obtained. Beyond the initial drop of the correlation function at ~ 5 fs, there are no recognizable major oscillations that are above noise level. This and the appearance of the broad photoelectron bands indicate that the molecular ions created by the photoionization event in this state undergo very fast intramolecular dynamic processes. The wave packet never regains its initial shape and returns to its initial position on the potential energy surfaces. Even the initial drop in the correlation function is much faster when compared with other bands of these molecular ions. This, in the spirit of Ruščić,

indicates that the ionic state equilibrium geometry is substantially different from not only the ground state equilibrium geometry of the neutral molecule, but also other ionic electronic states as well. Isotope effect showed up strongly here, the correlation strength of H_2CO^+ drops much faster than that of D_2CO^+

F. Conclusion

Rotationally cold photoelectron spectra of H_2CO and D_2CO with much improved resolution have allowed each of the four ionic electronic states accessible by the helium Iα radiation to be characterized in great detail. The assignment of the third and fourth ionic states to the $\tilde{B}\ ^2A_1$ and $\tilde{C}\ 2^2B_2$ states confirms the results of Brundle et al., and all theoretical calculations available. For the $\tilde{X}\ 1^2B_2$ and the $\tilde{A}\ ^2B_1$ state, the excitation of odd quanta of the non totally symmetric vibrational mode (ν_4) indicates the possibilities of non planar equilibrium geometries for these two states. Strong isotope effects were observed in the vibronic couplings in the $\tilde{A}\ ^2B_1$ and $\tilde{B}\ ^2A_1$ states. This indicates that for isotopic compounds the details of the ionic potential energy surfaces for the same electronic state can be very different. Rotationally resolved spectroscopic studies on H_2CO^+ and D_2CO^+ in its various ionic states will be very desirable to confirm the equilibrium geometries of these molecules in these ionic states.

Vibrational correlation functions were derived for all four electronic states. The variations between the isotopic species' correlation functions were attributed primarily to the differences in the details of the potential energy surfaces and in the phase space spanned by the initially formed wave packets. This isotope effect on vibronic coupling is especially evident in the case of the first and second excited states of formaldehyde, where completely different vibrational progressions were observed in the same electronic state of different isotopic compounds. Ultra fast intramolecular decay mechanisms were evident for the $\tilde{C}$ 2^2B_2 state of each isotopic ions. The decaying of this state occurred in a time scale of less

than one period of C-H stretching vibrational, supporting the relaxation pathway by predissociation through crossing by close lying and intersecting electronic states in that energy range. Further theoretical treatment on this state will be particularly important to understand the details of the ultra fast intramolecular dynamics evident in this investigation.

References:

1. A. D. Baker, C. Baker, C. R. Brundle, and D. W. Turner, Int. J. Mass Spectrom. Ion Phys., 1, 285(1968)
2. D. W. Turner, A. D. Baker, and C. R. Brundle, Molecular Photoelectron Spectroscopy, John Wiley & Sons, London, p135-137(1970)
3. W. V. Niessen, G. Bieri, and L. Åsbrink, J. Elect. Spect. Relat. Phenom. 21, 175(1980)
4. K. Kimura, S. Katsumata, Y. Achiba, T. Yamazak, and S. Iwata, Handbook of HeI Photoelectron Spectra of Fundamental Organic Molecules, Halsted, New York, (1981)
5. D. P. Chong, F. G. Herring, and D. Mcwilliams, J. Chem. Phys., 61, 958(1974)
6. L. S. Cederbaum, G. Hohlneicher, and W. V. Niessen, Mol. Phys., 26, 1405(1973)
7. L. S. Cederbaum, and W. Domcke, J. Chem. Phys., 64(2), 603(1976)
8. D. Domcke, and L. S. Cederbaum, *ibid*, 64(2), 612(1976)
9. J. F. Blanke, and J. Overend, in Vibrational Spectra and Structure, Vol. 7, p270-315(1978), ed. by J. R. Durig, Elsevier Sci. Pub. Com., New York

10a. D. C. Moule, Vibrational Spectra and Structure, Vol. 6, p228-271(1977), ed. by J. R. Durig, Elsevier Sci. Pub. Com., New York.

10b. I. W. Levin, and R. A. R. Pearce, in Vibrational Spectra and Structure, Vol. 4, ed. by J. R. Durig, Elsevier Sci. Pub. Com., New York, p102(1975).

11. C. R. Brundle, and D. W. Turner, Chem. Comm., 341(1967)
12. C. R. Brundle, M. B. Robin, N. A. Kuebler, and H. Basch, J. Am. Chem. Soc., 94, 1451(1972)
13. K. Takeshita, J. Chem. Phys., 94(11), 7259(1991)
14. P. M. Guyon, W. A. Chupka, J. Berkowitz, *ibid*, 64, 1419(1976)

15. R. Bombach, J. Dannacher, J-P Stadelmann, and J. Vogt, Chem. Phys. Lett., 76(3), 429(1980)

16. S. V. Andreyev, V. S. Antonov, I. N. Knyazev, and V. S. Letokhov, Chem. Phys. Lett., 45(1), 166(1977).

17. R. Bombach, J. Dannacher, J-P Stadelmann, and J. Vogt, Int. J. Mass Spectrom. Ion Phys., 40, 275(1981).

18. M. Van Pires, C. Galloy, and J. C. Lorquet, J. Chem. Phys., 69, 3242(1978).

19. S. T. Hood, A. Hamnett, and C. E. Brion, Chem. Phys. Lett., 41(3), 428(1976).

20. R. S. Mulliken, Rev. Mod. Phys., 14, 204(1942).

21a. A. D. Walsh, J. Chem. Soc., 2260(1953).

21b. D. C. Moule, A. D. Walsh, Chem. Rev., 75(1), 67-84(1975).

22. R.J. Buenker, S.D. Peyerimhoff, Chem. Rev., 74(2), 127-188 (1974).

23 E. J. Heller, J. Chem. Phys., 68, 2066(1978).

24. E. J. Heller, E. B. Stechel, M. J. Davis, *ibid*, 73(10), 4720(1980).

25. E. J. Heller, Acc. Chem. Res., 14, 368(1981).

26. E. J. Heller, R. Sundberg, and D. Tanner, J. Chem.. Phys., 76, 1822(1982).

27. B. Layh-Nihaut, and J. C. Lorquet, *ibid*, 88(9), 5606(1988).

28a. A. J. Lorquet, J. C. Lorquet, J. Delwiche, and M. J. Hubin-Franskin, *ibid*, 76(10), 4692(1982).

28b. B. Ruščić, *ibid*, 85(7), 3776(1986).

29. F. Remacle, M. Desoute-Leconmte, and J. C. Lorquet, *ibid*, 91(7), 4155(1989).

30. J. E. Pollard, D. J. Trevor, J. E. Reutt, Y. T. Lee, and D. A. Shirley, *ibid*, 81(2) 5302(1984).

31. J. E. Reutt, L. S. Wang, J. E. Pollard, D. J. Trevor, Y. T. Lee, and D. A. Shirley, *ibid*, 84(6), 3022(1986).

32. J. E. Reutt, L. S. Wang, Y. T. Lee, D. A. Shirley, *ibid*, 85(12), 6928(1986).

33. P. R. Keller, J. W. Taylor, F. A. Grimm, and T. A. Carlson, Chem. Phys., **90**, 147-153(1984).

34a. J. E. Pollard, D. J. Trevor, Y. T. Lee, and D. A. Shirley, Rev. Sci. Instrum., **52**, p1837 (1981).

34b. J. E. Pollard, Ph.D. Thesis, Department of Chemistry, The University of California at Berkeley (1982).

35. J. E. Reutt, Ph.D. Thesis, Department of Chemistry, The University of California at Berkeley (1986).

36a. R. Spencer, and W. Wild, **J. Chem. Soc.**, London, 338-340(1935).

36b. R. Spence, and W. Wild, **J. Chem. Soc.**, London, 506-509(1935).

37. W. E Polik, Ph.D. Thesis, Department of Chemistry, The University of California at Berkeley (1988)

38. A. Lofthus, and P.H. Krupenie, J. Phys. Chem. Ref. Data, **6**, 113 (1977)

39. Atomic Energy Levels, Vol. I, II, III, ed. by C. E. Moore, (National Bureau of Standards, Washington D.C., 1958).

40a. M. Born, J.R. Oppenheimer, Ann. Phys.(Lepzig), **84**, 457-484 (1927).

40b. M. Born, Nachr. Akad. Wiss. Gottingen, Math.-Phys. **KL**, IIa, P1 (1951).

40c. M. Born, K. Huang, Dynamics of Crystal Lattice, Oxford U. Press, NY., (1954).

41. J. W. Rabalais, **Principles of Ultraviolet Photoelectron Spectroscopy**, John Wiley & Sons, New York (1979)

42. H. Köppel, W. Domcke, and L. S. Cederbaum, **Adv. Chem. Phys.**, Vol. LVII, p59-246(1984)

43. E. Oran Brighan, The Fast Fourier Transform, (Prentice-Hall, Englewood Cliffs), p164(1974).

44. R. J. Buenker, and S. D. Peyerimhoff, Chem. Rev., **7(2)**, 127-188(1974)

45. R. J. Buenker, and S. D. Peyerimhoff, J. Chem. Phys., **53**, 1368(1970)

46a. J. I Steinfeld, **An Introduction to Modern Molecular Spectroscopy**, 2nd ed., The **MIT** Press, Cambridge, MA(1985) p133.

46b. G. Herzberg, **Molecular Spectra & Molecular Structure**, **I. Spectra of Diatomic Molecules**, Van Norstrand Reinhold Com., New York, p93(1950).

47. D. E. Reisner, R. W. Field, J. L. Kinsey, and H-L Dai, J. Chem. Phys., **80(12)**, 5968-5978(1984).

48. D. J. Clouthier, and D. A. Ramsay in **Ann. Rev. Phys. Chem.**, **34**, p31-58(1983).

TABLE I. Ionizarion Potenitails & Vibrational Frequencies Observed

Ionic States	AIE[a] (eV)	ν_1 (cm^{-1})	ν_2 (cm^{-1})	ν_3 (cm^{-1})	ν_4 (cm^{-1})
H_2CO^f, $\tilde{X}\ ^1A_1$		2782.5	1746.0	1500.2	1167.3
H_2CO^+, $\tilde{X}\ 1^2B_2$	10.8887(4)	2580.2 (4.3)	1674.8(4.3)	1210.2(4.3)	777.1(4.3)
$\tilde{A}\ ^2B_1$	14.1024(2)		1250.5(4.3)	1487.7 (4.3)	262.8[c](4.3)
$\tilde{B}\ ^2A_1$	15.8375(3)		1304.5(4.3)	1304 (4.3)	
$\tilde{C}\ 2^2B_2$	16.2395(3)	1894.9[d]		1411.7[d]	
D_2CO^f, $\tilde{X}\ ^1A_1$		2055.8	1701.6	1105.7	938.0
D_2CO^+, $\tilde{X}\ 1^2B_2$	10.9076(4)	1948.2 (4.3)	1656.7 (4.3)	919.9 (4.3)	648.1(4.3)
$\tilde{A}\ ^2B_1$	14.0999(5)	1064.5 (4.3)	1281.6 (4.3)		776.6[e](4.3)
$\tilde{B}\ ^2A_1$	15.8425(2)		1311.1 (4.3)	957.3 (4.3)	
$\tilde{C}\ 2^2B_2$	16.4350(200)[b]	1604.4[d] (4.3)	943.4.4[d] (4.3)	818.7[d] (4.3)	

(a) The absolute AIEs are accurate to ±3 meV as discussed in the main text. Other spectroscopic quantities, however, were obtained as line splittings, and can thus be reported to a much higher accuracy ±0.5 meV (4.3 cm^{-1}). (b) This value is only the best estimate. (c) The value of ν_4 = 1, 0 splitting. (d) These values are estimates only. (e) The average value of ν_4 = 2, 1, 0 splittings. (f) From Ref. 47,48. Numbers in parenthese indicate the uncertainties in the last digit.

TABLE II. Vibrational Levels of the $\tilde{X}\ 1^2B_2$ State

H_2CO^+		D_2CO^+	
IE[a] (eV)	$\nu_1\nu_2\nu_3\nu_4$	IE[a] (eV)	$\nu_1\nu_2\nu_3\nu_4$
10.8887(3)	0000	10.9076(3)	0000
10.9834(5)	0001	11.1456(7)	1000
11.0748(6)	0002	11.3765(3)	2000
11.0380(8)	0010	11.1116(8)	0100
11.1858(4)	0020	11.3128(2)	0200
11.0940(2)	0100	11.0178(5)	0010
11.2946(5)	0200	11.1203(2)	0020
11.2086(3)	1000	10.9887(4)	0001
11.2483(8)	0110	11.0729(3)	0002
		11.1584(6)	0003

H_2CO^+		D_2CO^+	
$\nu_n(n=1\text{-}4)(cm^{-1})$	$\omega_e x_e(cm^{-1})$	$\nu_n(n=1\text{-}4)(cm^{-1})$	$\omega_e x_e(cm^{-1})$
2580.2(4.3)		1948.2(4.3)	28.6(4.3)
1674.8(4.3)	19.0(4.3)	1656.7(4.3)	11.3(4.3)
1210.2(4.3)	6.1(4.3)	919.9(4.3)	31.1(4.3)
777.1(4.3)	13.3(4.3)	648.1(4.3)	8.9(4.3)

(a) The absolute IEs are accurate to ±3.0 meV as discussed in the main text. Other spectroscopic constants, however, were obtained as line splittings, can thus be reported to a much higher accuracy ±0.5 meV(4.3 cm^{-1}).

TABLE III. Vibrational Levels of the $\tilde{A}\,^2B_1$ State

IE[a] H_2CO^+ (eV)	Vibrational Progressions ($\nu_1\nu_2\nu_3\nu_4$)		
14.1024(2)		0000	
14.1280(3)			0001
14.2839(5)		0010	
14.4724(5)		0020	
14.6536(9)		0030	
14.2560(2)	0100		
14.4072(8)	0200		
14.5562(3)	0300		
14.7028(4)	0400		
14.8471(3)	0500		
14.9867(6)	0600		
15.1264(2)	0700		
15.2660(2)	0800		
15.3963(4)	0900		
14.2839(5)		0010	
14.4375(4)		0110	
14.5888(1)		0210	
14.7354(2)		0310	
14.8820(3)		0410	
15.0239(9)		0510	
15.1659(5)		0610	
15.3032(5)		0710	

Table III. continued

15.4382(3)		0810	
14.4724(5)	0020		
14.6213(9)	0120		
14.7726(6)	0220		
14.9192(7)	0320		
15.0658(8)	0420		
15.2031(8)	0520		
15.3474(7)	0620		
14.6536(9)		0030	
14.8073(9)		0130	
14.9519(2)		0230	
15.0918(6)		0330	
ν_2 = 1250.5 (4.3) cm^{-1}		$\omega_e x_e$ = 10.0 (4.3) cm^{-1}	
ν_3 = 1487.7 (4.3) cm^{-1}		$\omega_e x_e$ = 0.6 (4.3) cm^{-1}	

a. See table II. footnotes, also see main text

IE[a] D_2CO^+ (eV)	Vibrational Progressions ($\nu_1\nu_2\nu_3\nu_4$)		
14.0999(5)		0000	
14.1366(4)			0001
14.2925(2)			0002
14.2283(6)	1000		
14.3659(4)	2000		
14.4874(8)	3000		
14.6204(8)	4000		
14.2604(6)		0100	

Table III. continued

14.4163(9)		0200
14.5723(2)		0030
14.7282(5)		0040
14.8750(2)		0050
15.0309(4)		0060
15.1763(1)		0070
15.3282(1)		0080
15.4755(9)		0090
14.2283(6)	1000	
14.3865(8)	1100	
14.5425(1)	1200	
14.6984(4)	1300	
14.8497(8)	1400	
15.0034(2)	1500	
15.1473(4)	1600	
15.2982(4)	1700	
15.4456(2)	1800	
14.2283(6)		2000
14.3659(84		2100
14.5149(9)		2200
14.6686(3)		2300
14.8199(7)		2400
14.9736(1)		2500
15.1207(9)		2600

Table III. continued

15.2694(2)		2700
15.4156(4)		2800
14.4874(8)	3000	
14.6411(2)	3100	
14.7924(6)	3200	
14.9438(2)	3300	
15.0959(2)	3400	
15.2407(8)	3500	
15.3881(6)	3600	
15.5330(4)	3700	
14.6204(8)		4000
14.7718(2)		4100
14.9185(1)		4200
15.0749(3)		4300
15.2233(2)		4400
15.3656(8)		4500
15.5055(6)		4600
ν_1 = 1064.5 (4.3) cm^{-1}		$\omega_e x_e$ = 10.0 (4.3) cm^{-1}
ν_2 = 1281.6 (4.3) cm^{-1}		$\omega_e x_e$ = 5.7 (4.3) cm^{-1}

a. The accuracy of the IEs are ±1.0 meV for this state only: see main text for discussions.

TABLE IV. Vibrational Levels of the $\tilde{B}\,^2A_1$ State

IE[a] of H_2CO^+ (eV)	Vibrational Progressions ($\nu_1\nu_2\nu_3$)		
15.8375(2)		000	
15.9963(1)	010		
16.1541(1)	020		
16.3079(5)	030		
16.4593(2)	040		
16.6071(1)	050		
16.7506(6)	060		
ν_2 = 1304.5 (4.3) cm^{-1}		$\omega_e x_e$ = 12.6 (4.3) cm^{-1}	

(a) The accuracy of the IEs reported here are ±1.0 meV: see main text for discussions.

IE[a] of D_2CO^+ (eV)	Vibrational Progressions ($\nu_1\nu_2\nu_3$)		
15.8425(2)		000	
15.9631(8)	001		
16.0823(7)	002		
16.1986(1)	003		
16.3111(9)	004		
16.4229(3)	005		
16.5422(4)	006		
16.6558(8)	007		
16.0029(1)			010
16.1603(5)			020
16.3111(9)			030
16.4649(5)			040
16.6062(1)			050

TABLE IV. continued

16.7497(6)		060
15.9631(8)	001	
16.1235(7)	011	
16.2740(5)	021	
16.4240(5)	031	
16.5826(7)	041	
16.7324(6)	051	
16.08237		002
16.2412(8)		012
16.3972(6)		022
16.5502(9)		032
16.6954(2)		042
16.19861	003	
16.3575(3)	013	
16.5127(7)	023	
ν_2 = 1311.1 (4.3) cm^{-1}		$\omega_e x_e$ = 15.3 (4.3) cm^{-1}
ν_3 = 957.3 (4.3) cm^{-1}		$\omega_e x_e$ = 3.4 (4.3) cm^{-1}

a. See table II. footnotes.

TABLE V. Vibrational Levels of the $\tilde{C}\ 2^2B_2$ State

IE[a] of H_2CO^+ (eV)	Vibrational Progressions ($\nu_1\nu_2\nu_3$)		
16.2395(3)		000	
16.4811(5)	100		
16.7065(3)	200		
16.9304(2)	300		
17.1581(2)	400		
17.3832(1)	500		
17.6041(3)	600		
17.8163(5)	700		
16.4130(2)			001
16.5833(8)			002
16.7506(6)			003
16.5316(1)	010		
16.792(8)	110		
17.0449(5)	210		
17.2958(7)	310		
17.5304(2)	410		
17.7450(5)	510		
16.63914			020
16.8145(2)			021
16.9825(1)			022
17.1428(4)			023
17.3123(5)			024
17.4631(5)			025

TABLE V. continued

17.6180(4)	026
17.7760(3)	027
ν_1 = 1894.9 (4.3) cm^{-1}	$\omega_e x_e$ = 11.3 (4.3) cm^{-1}
ν_2 = ? cm^{-1}	$\omega_e x_e$ = ? cm^{-1}
ν_3 = 1411.7 (4.3) cm^{-1}	$\omega_e x_e$ = 12.5 (4.3) cm^{-1}

a. See table II. footnotes, also see main text for discussions.

IE[a] D_2CO^+ (eV)	Vibrational Progressions ($\nu_3\nu_2\nu_3$)
16.4350(200)	000 (?)
16.5036(5)	001
16.6973(4)	101
16.8863(2)	201
17.0799(9)	301
17.2524(2)	401
17.4272(1)	501
17.5972(7)	601
16.6341(6)	100
16.7310(9)	110
16.8680(2)	120
16.9938(3)	130
17.1300(6)	140
17.2621(4)	150
17.3873(8)	160
17.5216(9)	170
16.8381(5)	020

TABLE V. continued

16.9181(5)	021
17.0322(9)	022
17.1525(8)	023
17.2621(4)	024
17.3732(2)	025
17.4909(8)	026
17.6086(7)	027

ν_1 = 1604.4 (4.3) cm^{-1}	$\omega_e x_e$ = 22.3 (4.3) cm^{-1}
ν_2 = 943.4 (4.3) cm^{-1}	$\omega_e x_e$ = -12.7 (4.3) cm^{-1}
ν_3 = 818.7 (4.3) cm^{-1}	$\omega_e x_e$ = -11.8 (4.3) cm^{-1}

a. See footnote of table II., also see main text for discussions.

Figure Captions:

Figure 1. The full spectrum of formaldehyde with a resolution of 11 meV FWHM, the result of four sequential scans each lasting about two hours. Each scan was repeated four times to enhance statistics. The designation of the ionic states assumes that the ions have C_{2V} symmetry.

Figure 2. The full spectrum of D_2 formaldehyde with a resolution of 11 meV FWHM, the result of four sequential scans each lasting about two hours. Each scan was repeated four times to enhance statistics. The designation of the ionic states assumes that the ions have C_{2V} symmetry.

Figure 3. The photoelectron spectrum of the $\tilde{X}\ 1^2B_2$ state of the H_2CO^+, with a resolution of 11 meV FWHM. The vibrational progressions are labeled according to the C_{2V} geometry and 2_0^1 stands for the transition of

$$M^+ (\nu_2 = 1) + e^- \leftarrow M (\nu_2 = 0) + \hbar\, \omega$$

following standard spectroscopic notations.

Figure 4. The photoelectron spectrum of the $\tilde{X}\ 1^2B_2$ state of the D_2CO^+, with a resolution of 11 meV FWHM. The vibrational progressions are labeled under the C_{2V} geometry , and notations are the same as in the $\tilde{X}\ 1^2B_2$ state of H_2CO^+.

Figure 5. The vibrational autocorrelation function of the $\tilde{X}\ 1^2B_2$ state of H_2CO^+ after all the corrections have been made. The complex beat paten of the correlation function was the result of excitation of three totally symmetric vibrations, and possibly of the out-of-plane bending vibration as well. The overall slow decay of the correlation function, however, indicates that the

molecular ions are in a fairly stable configuration.

Figure 6. The vibrational correlation function for the $\tilde{X}\ 1^2B_2$ state of D_2CO^+ after all the corrections have been made. The main features of the correlation function are the same as those in the $\tilde{X}\ 1^2B_2$ state of H_2CO^+.

Figure 7. The photoelectron spectrum of the $\tilde{A}\ ^2B_1$ state of H_2CO^+ with a resolution of 11 meV FWHM. The vibrational progressions are assigned assuming the molecular ions have C_{2V} equilibrium geometry. Notations are the same as in Figure 3. Rotational cooling combined with the high resolution obtained by this study, enabled the multiplet vibrational fine structures to be fully resolved here for the first time.

Figure 8. The photoelectron spectrum of the $\tilde{A}\ ^2B_1$ state of D_2CO^+ with a resolution of 11 meV FWHM. The vibrational progressions are assigned assuming the molecular ions have C_{2V} equilibrium geometry. Notations are the same as in Figure 3. Note that the vibrational progressions are different than those of H_2CO^+.

Figure 9. The vibrational autocorrelation function calculated for the $\tilde{A}\ ^2B_1$ state of H_2CO^+ . Note the beat pattern caused by multimode excitation and a small spin-orbit splitting for this state. Shown at the bottom, is the correlation function after corrections have been made. The monotonic decay of the correlation function indicates a stable configuration in the **Franck-Condon** region.

Figure 10. The same as in Figure 9, for the $\tilde{A}\ ^2B_1$ state of D_2CO^+ . Note the isotope effects at play in the correlation function. The correlation function of D_2CO^+

decays much slower than H_2CO^+.

Figure 11. The photoelectron spectrum of the $\tilde{B}\,^2A_1$ and $\tilde{C}\,2^2B_2$ states of H_2CO^+ with a resolution of 11 meV FWHM. Note the FWHM of the peaks in this band are only about 12 meV, indicating very effective rotational relaxation in the supersonic expansion. The features clearly show that there is only one vibrational progression in the $\tilde{B}\,^2A_1$ state

Figure 12. The photoelectron spectrum of the $\tilde{B}\,^2A_1$ state of D_2CO^+ with a resolution of 11 meV FWHM. Note the FWHM of the peaks in this band are only about 12 meV, indicating very effective rotational relaxation in the supersonic expansion. The features observed clearly show that there are at least two vibrational modes excited.

Figure 13. The vibrational correlation function calculated for the $\tilde{B}\,^2A_1$ state of H_2CO^+ after all corrections were made. The correlation function clearly shows that there is only one vibrational mode excited. The slow decay of the correlation function and the ability of the correlation function to remain large for a sufficient long time indicates again, that the ionic state is very stable with respect to deformations along the Q_2 normal coordinate.

Figure 14. The vibrational correlation function calculated for the $\tilde{B}\,^2A_1$ state of D_2CO^+ after corrections for rotation and instrumental response function. Note the slow modulations on the correlation function which was caused by the excitation of more than one vibrational mode. The complexity of this beat pattern makes correction not feasible, and it was not attempted. However, the slowly decay pattern of the correlation function is still visible.

Figure 15. The photoelectron spectrum of the $\tilde{C}\ 2^2B_2$ state of D_2CO^+ with a resolution of 11 meV FWHM. Even with very effective rotational cooling and current high resolution measurements, the complexity of this band still eludes our analysis. The band structure observed is the characteristic of a repulsive state.

Figure 16. The vibrational correlation function calculated for the $\tilde{C}\ 2^2B_2$ state of H_2CO^+ after all corrections were made. The main feature of the correlation function is the extremely fast decay and loss of correlation, indicating ultra fast intramolecular dynamics processes.

Figure 17. The vibrational correlation function calculated for the $\tilde{C}\ 2^2B_2$ state of D_2CO^+ after all corrections were made. The main feature of the correlation function is the extremely fast decay and loss of correlation. Just as in most other states studied here, the isotope effect does show up in the decay of the correlation function.

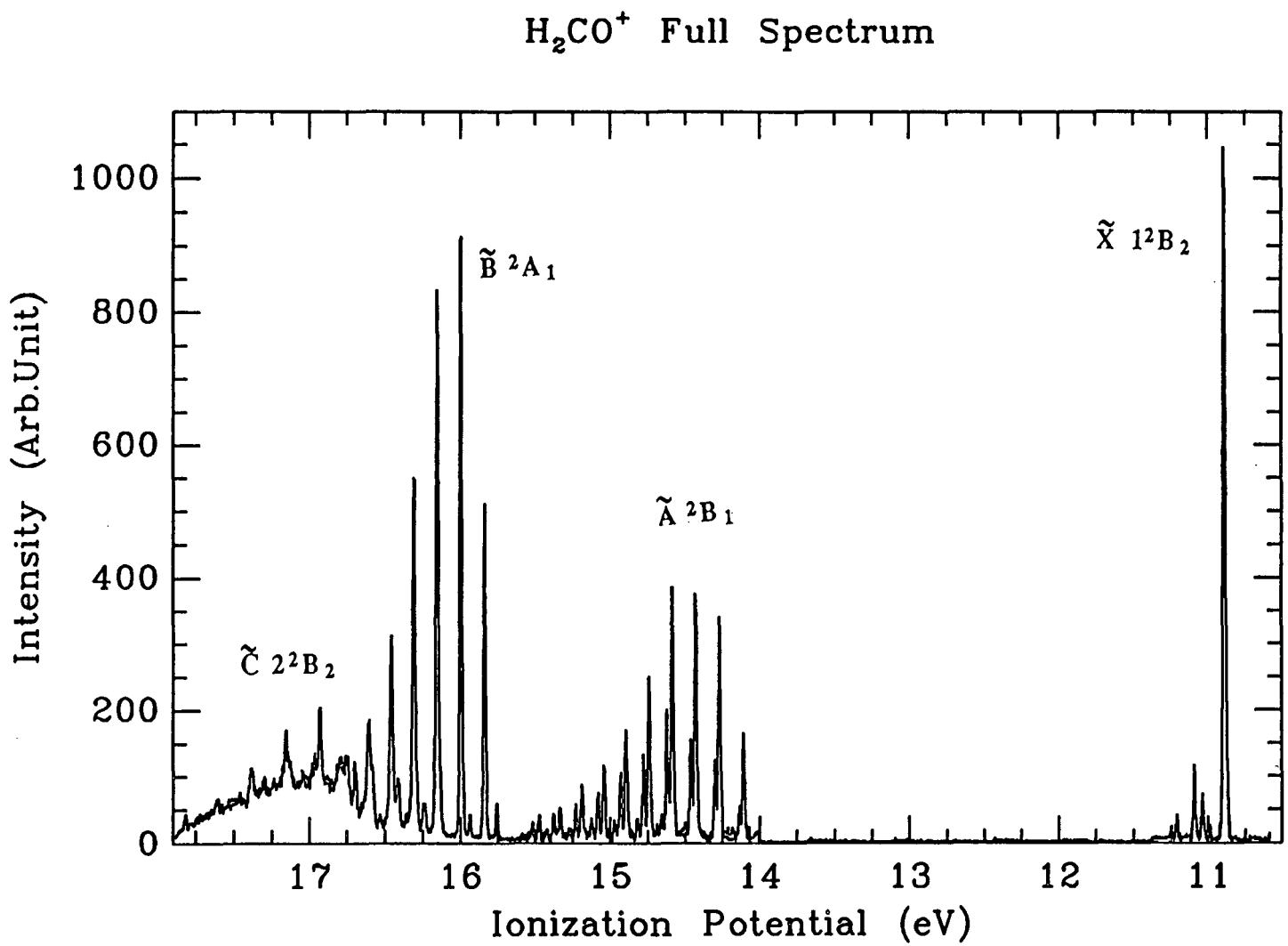
H_2CO^+ Full Spectrum
Intensity (Arb.Unit)
1000
800
600
400
200
0
17
16
15
14
13
12
11
Ionization Potential (eV)
$\tilde{C}\ 2^2B_2$
$\tilde{B}\ ^2A_1$
$\tilde{A}\ ^2B_1$
$\tilde{X}\ 1^2B_2$

Figure 1

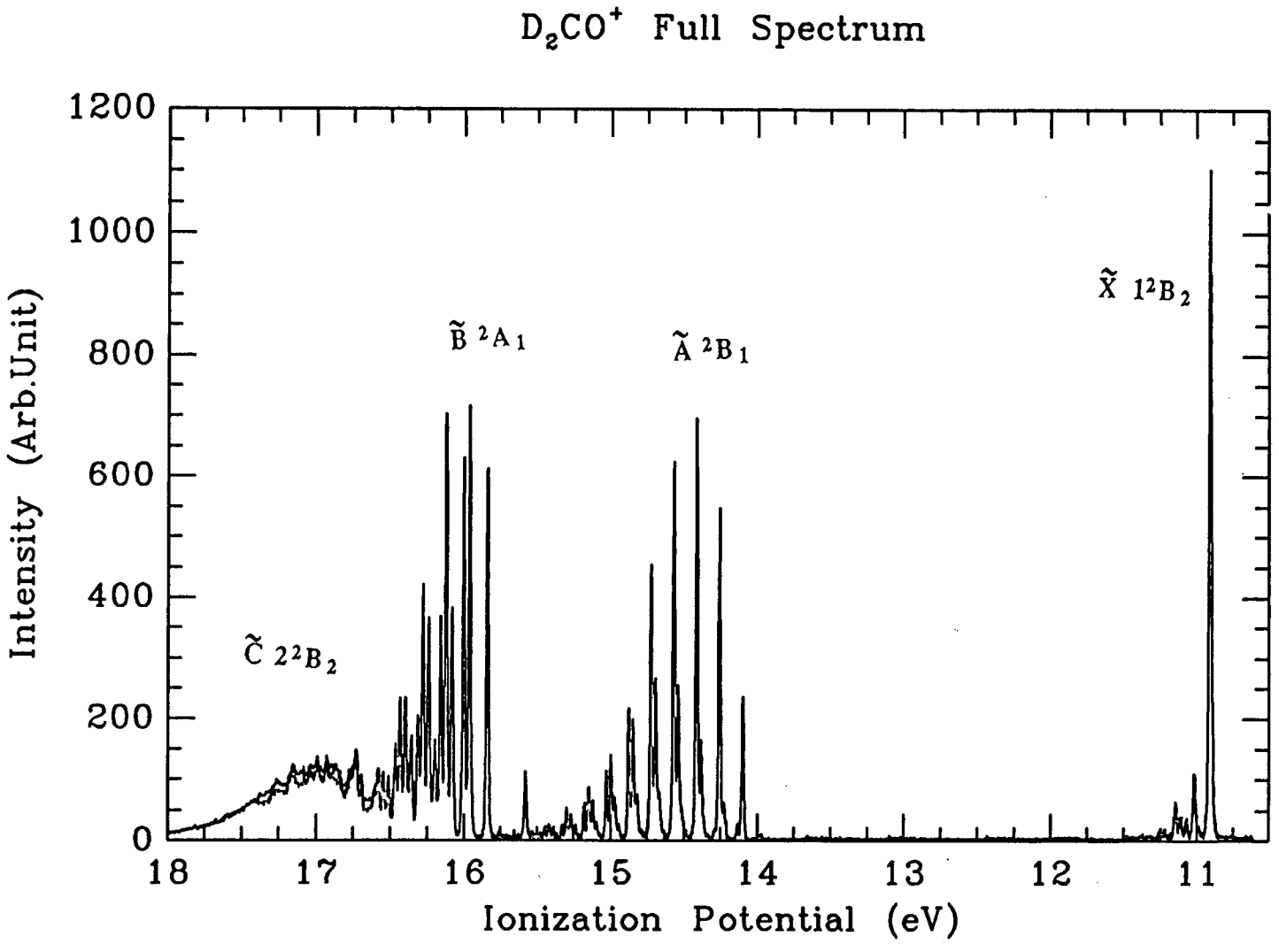
D_2CO^+ Full Spectrum
Intensity (Arb.Unit)
1200
1000
800
600
400
200
0
18
17
16
15
14
13
12
11
Ionization Potential (eV)
$\tilde{C}\ 2^2B_2$
$\tilde{B}\ ^2A_1$
$\tilde{A}\ ^2B_1$
$\tilde{X}\ 1^2B_2$

Figure 2

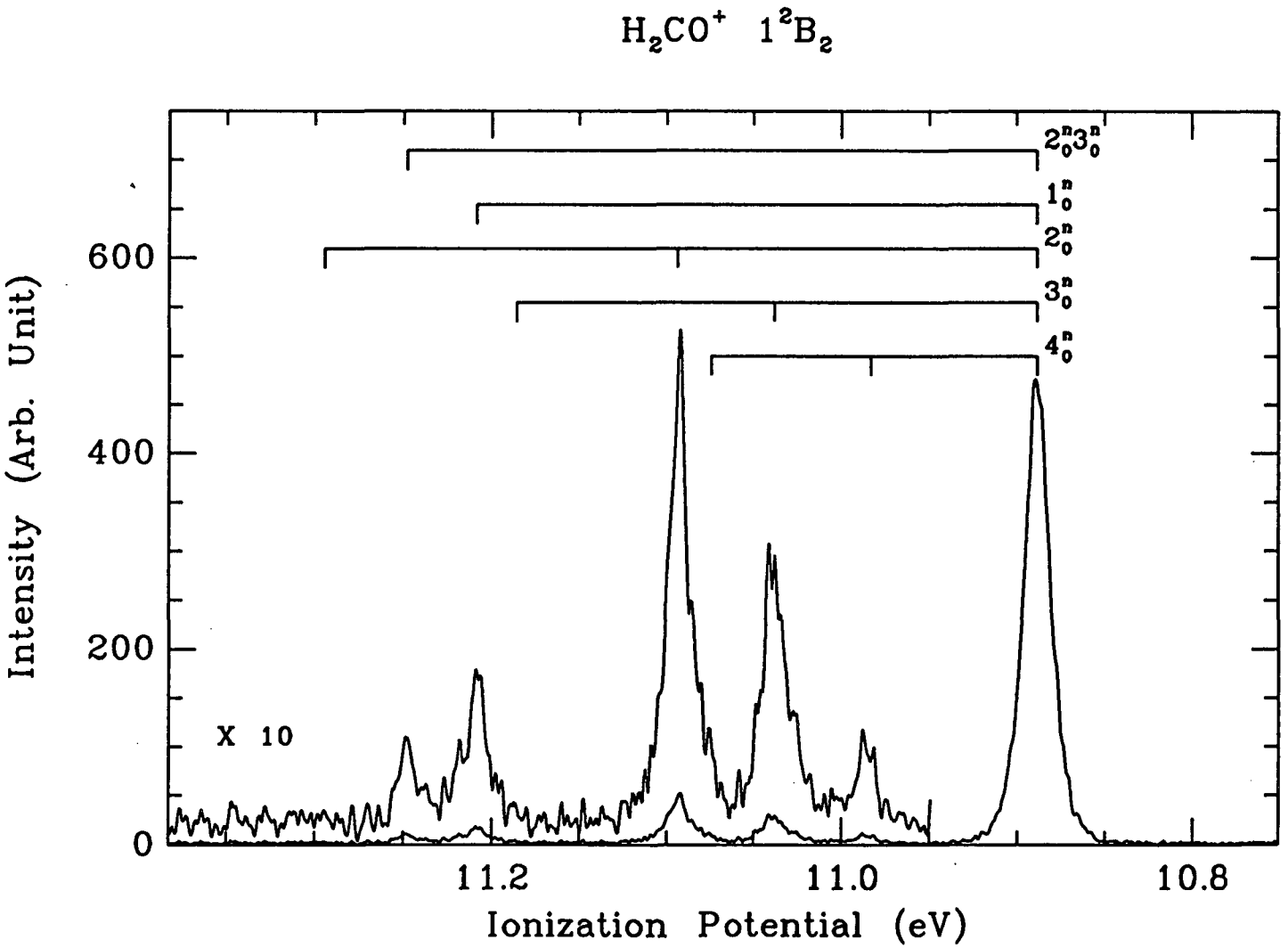
H_2CO^+ 1^2B_2
$2_0^n3_0^n$
1_0^n
2_0^n
3_0^n
4_0^n
600
400
200
0
Intensity (Arb. Unit)
X 10
11.2
11.0
10.8
Ionization Potential (eV)

Figure 3

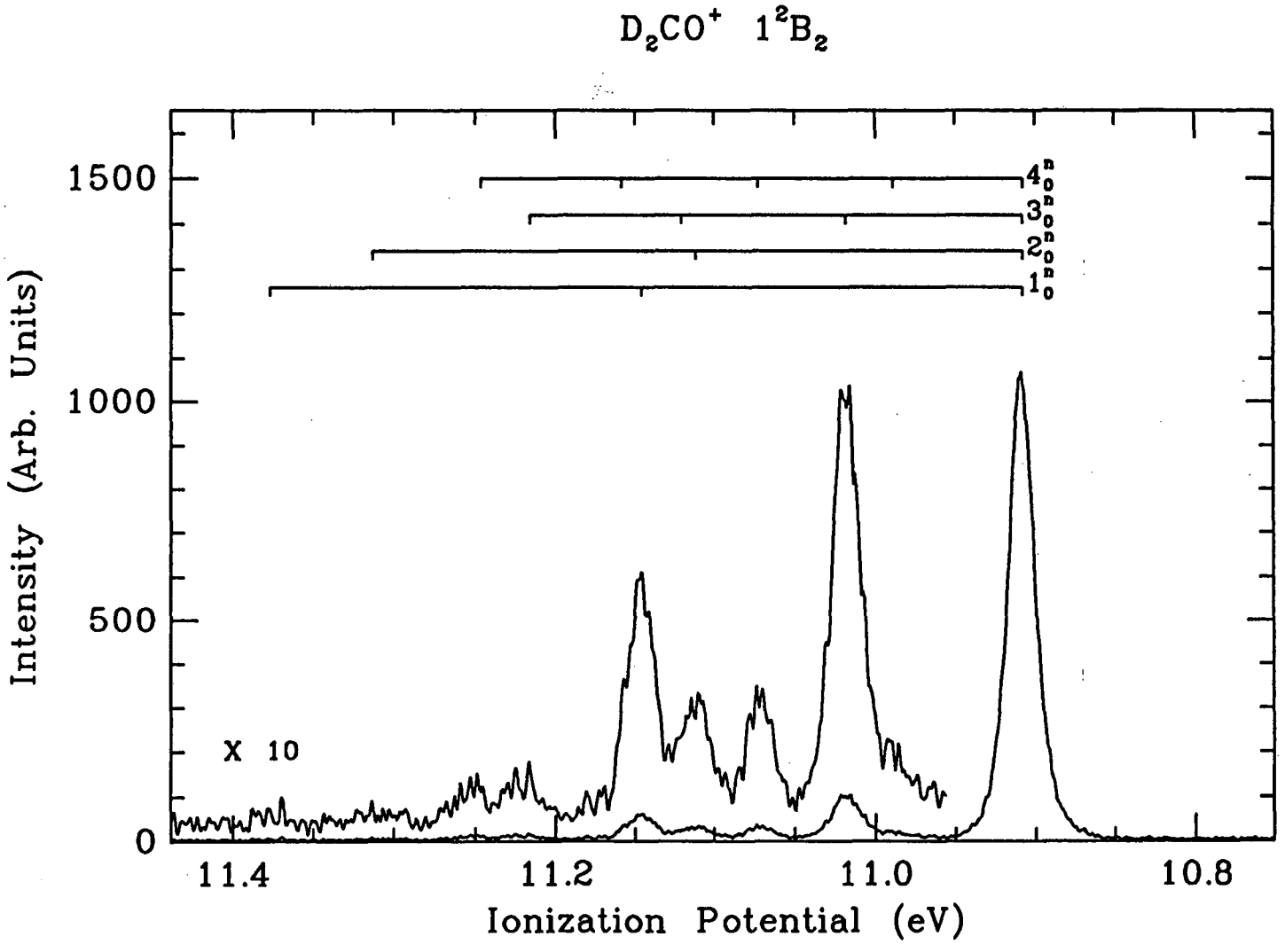
D2CO+ 1²B2
1500
1000
500
0
Intensity (Arb. Units)
X 10
4b0
3b0
2b0
1b0
11.4
11.2
11.0
10.8
Ionization Potential (eV)

Figure 4

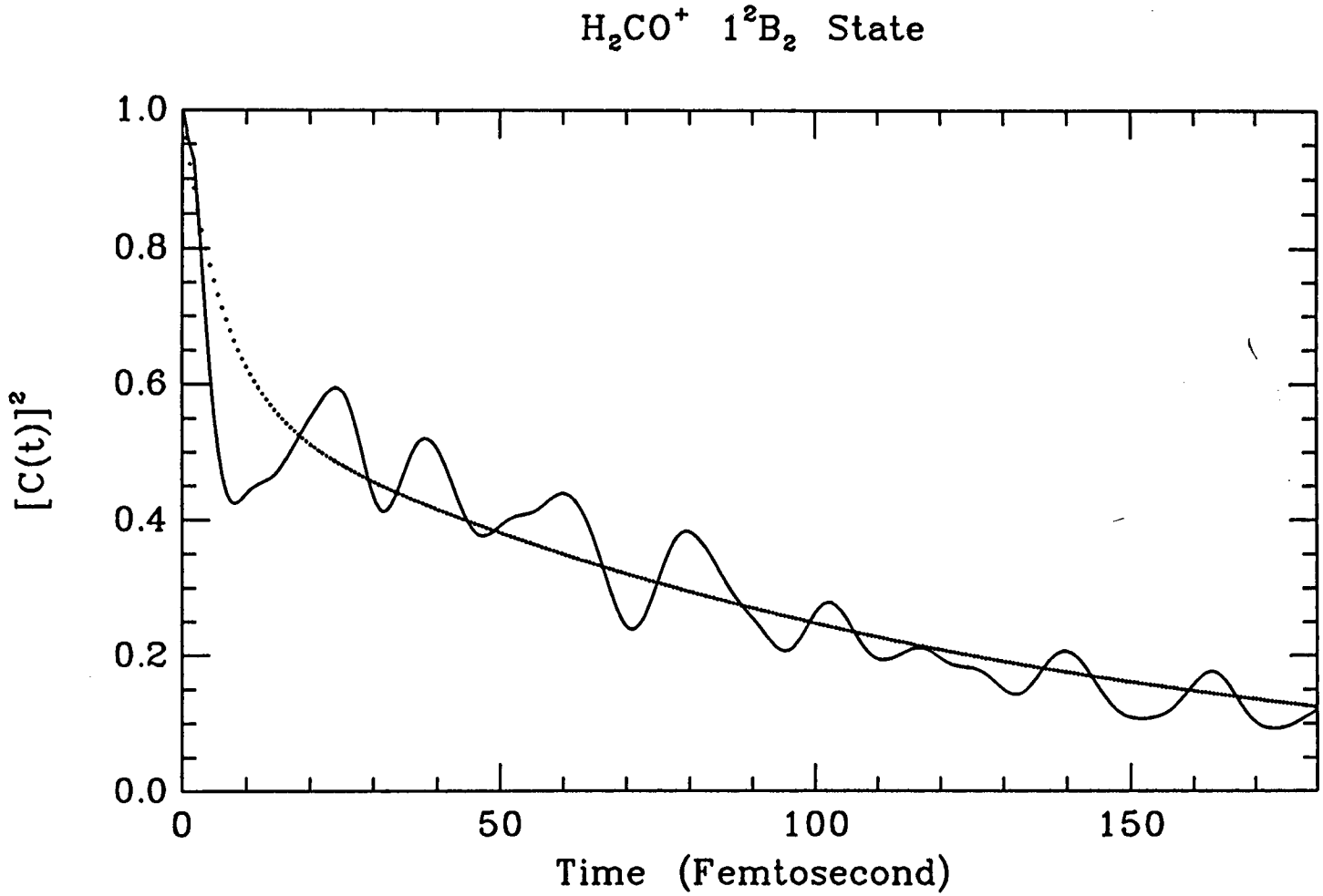
H_2CO^+ 1^2B_2 State
1.0
0.8
0.6
0.4
0.2
0.0
$[C(t)]^2$
0
50
100
150
Time (Femtosecond)

Figure 5

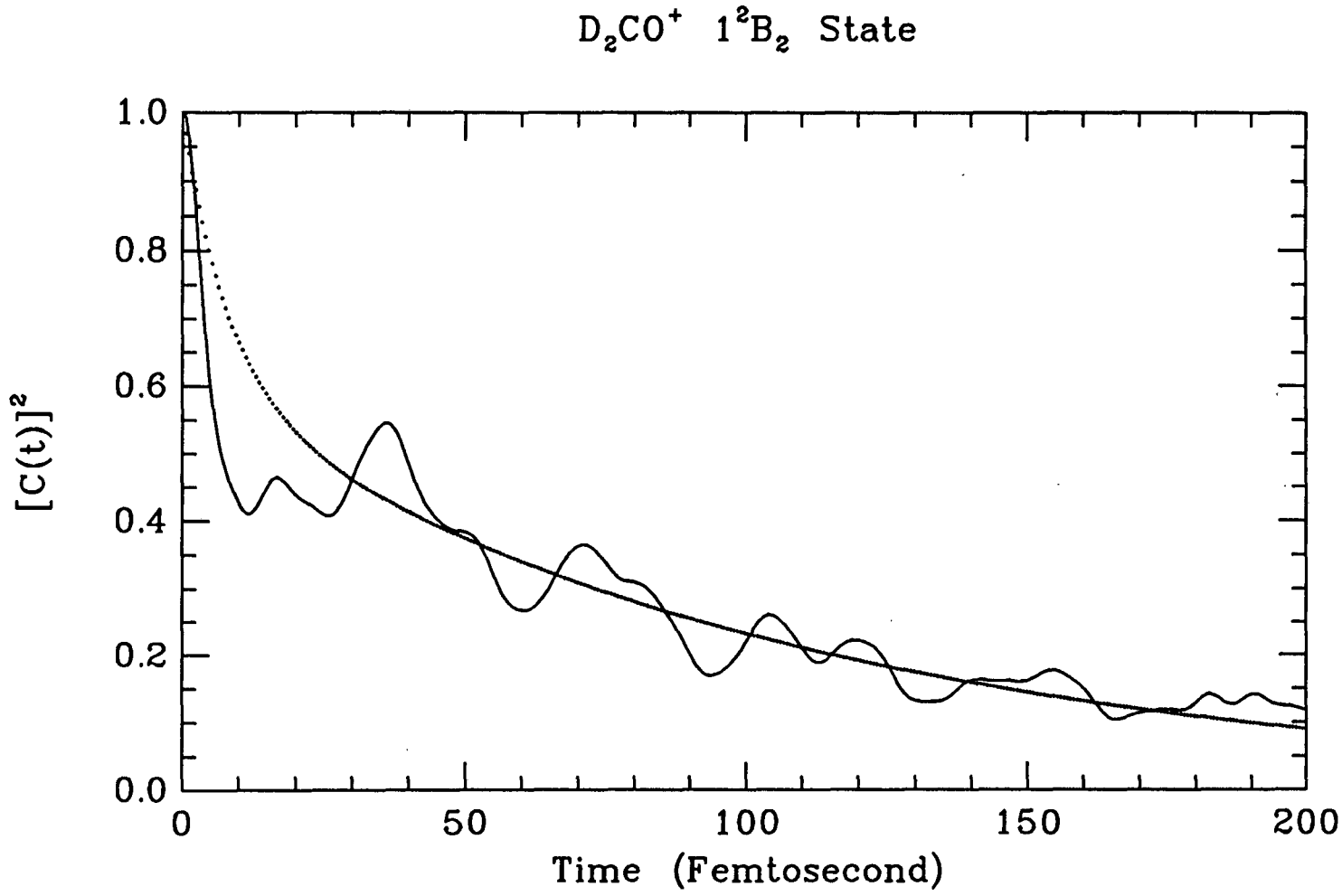
D_2CO^+ 1^2B_2 State
1.0
0.8
0.6
0.4
0.2
0.0
$[C(t)]^2$
0
50
100
150
200
Time (Femtosecond)

Figure 6

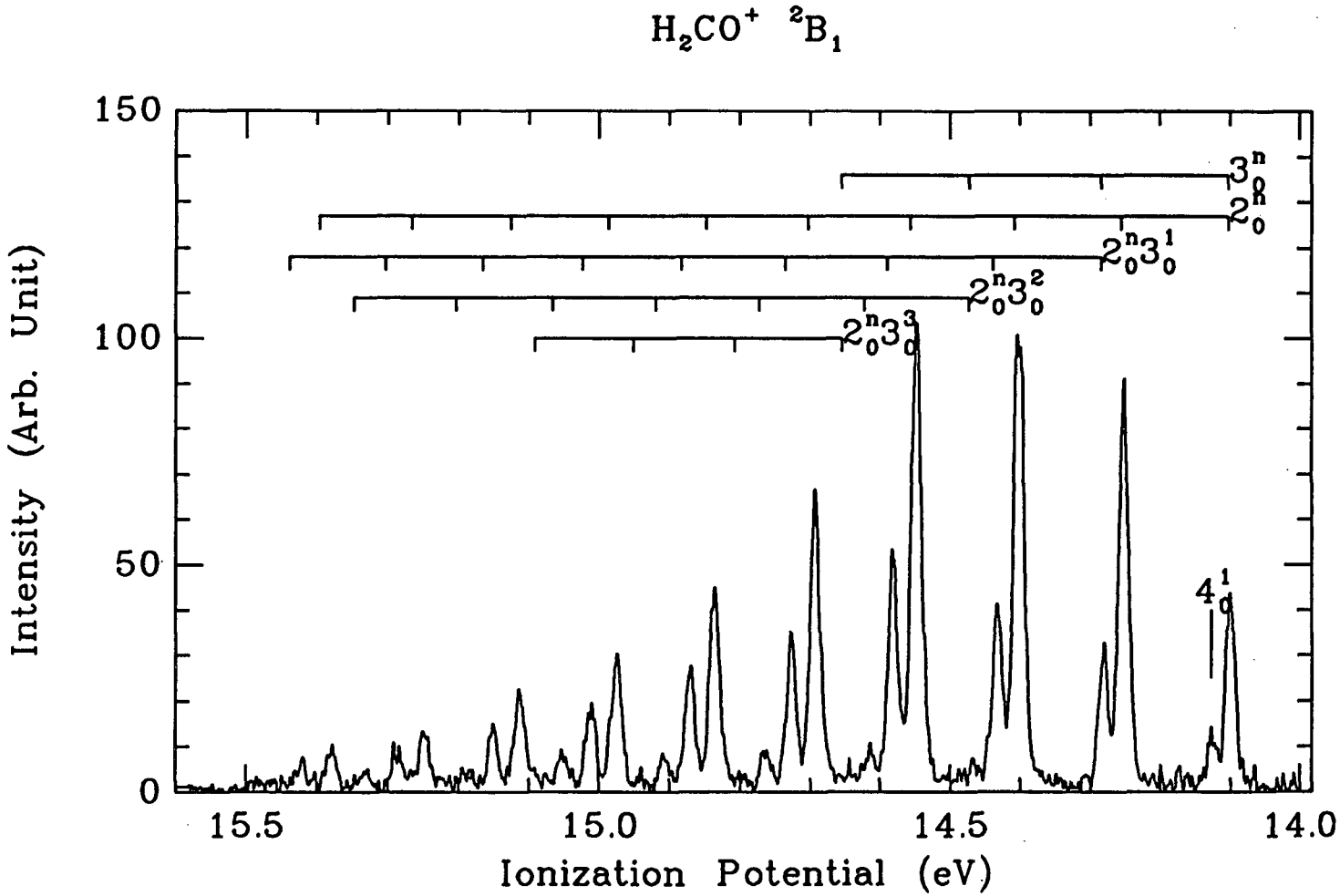
H_2CO^+ $^2B_1$
150
100
50
0
Intensity (Arb. Unit)
15.5
15.0
14.5
14.0
Ionization Potential (eV)
3_0^n
2_0^n
$2_0^n3_0^1$
$2_0^n3_0^2$
$2_0^n3_0^3$
4_0^1

Figure 7

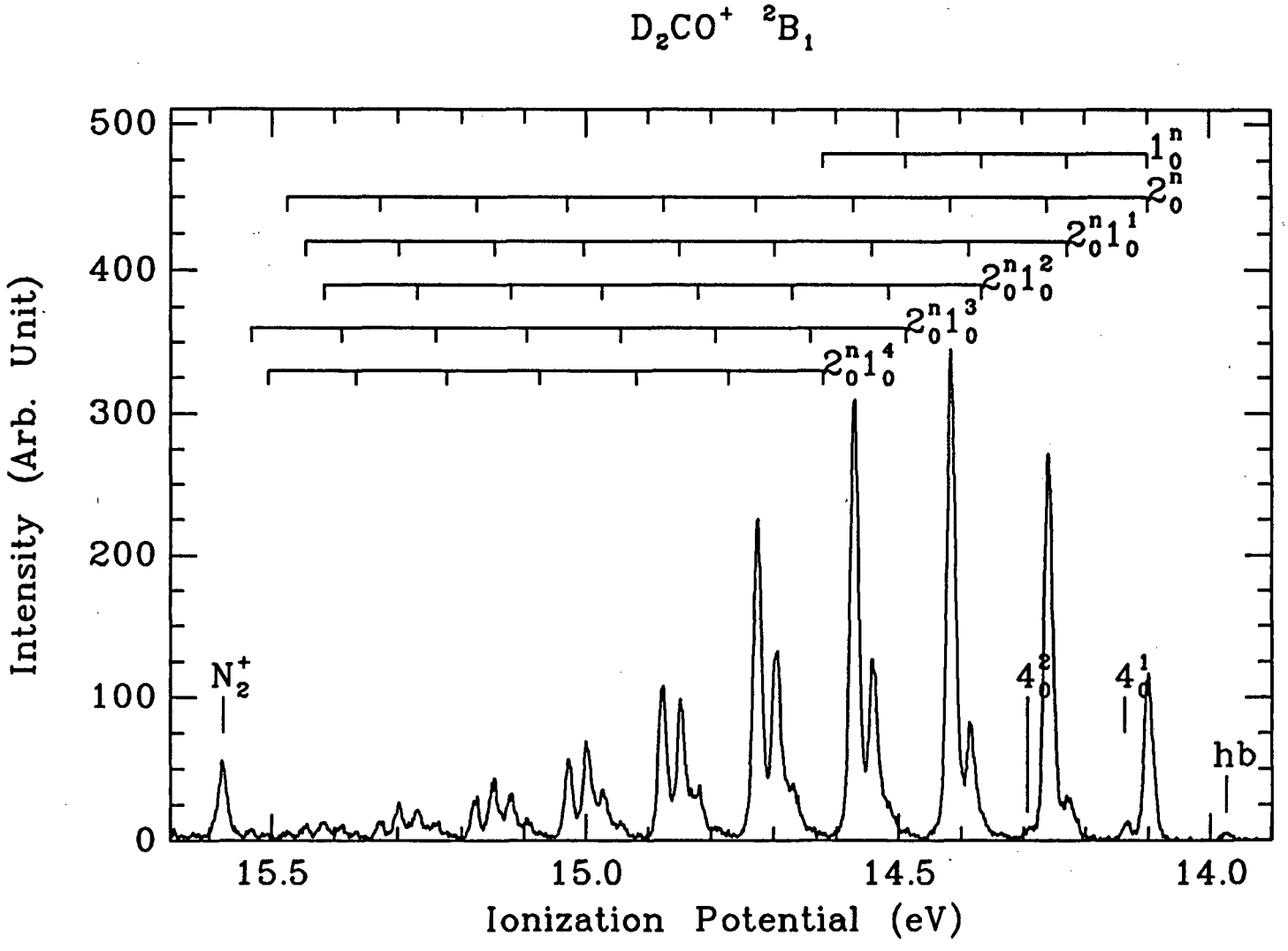
D_2CO^+ $^2B_1$
Intensity (Arb. Unit)
500
400
300
200
100
0
15.5
15.0
14.5
14.0
Ionization Potential (eV)
1_0^n
2_0^n
$2_0^n 1_0^1$
$2_0^n 1_0^2$
$2_0^n 1_0^3$
$2_0^n 1_0^4$
N_2^+
4_0^2
4_0^1
hb

Figure 8

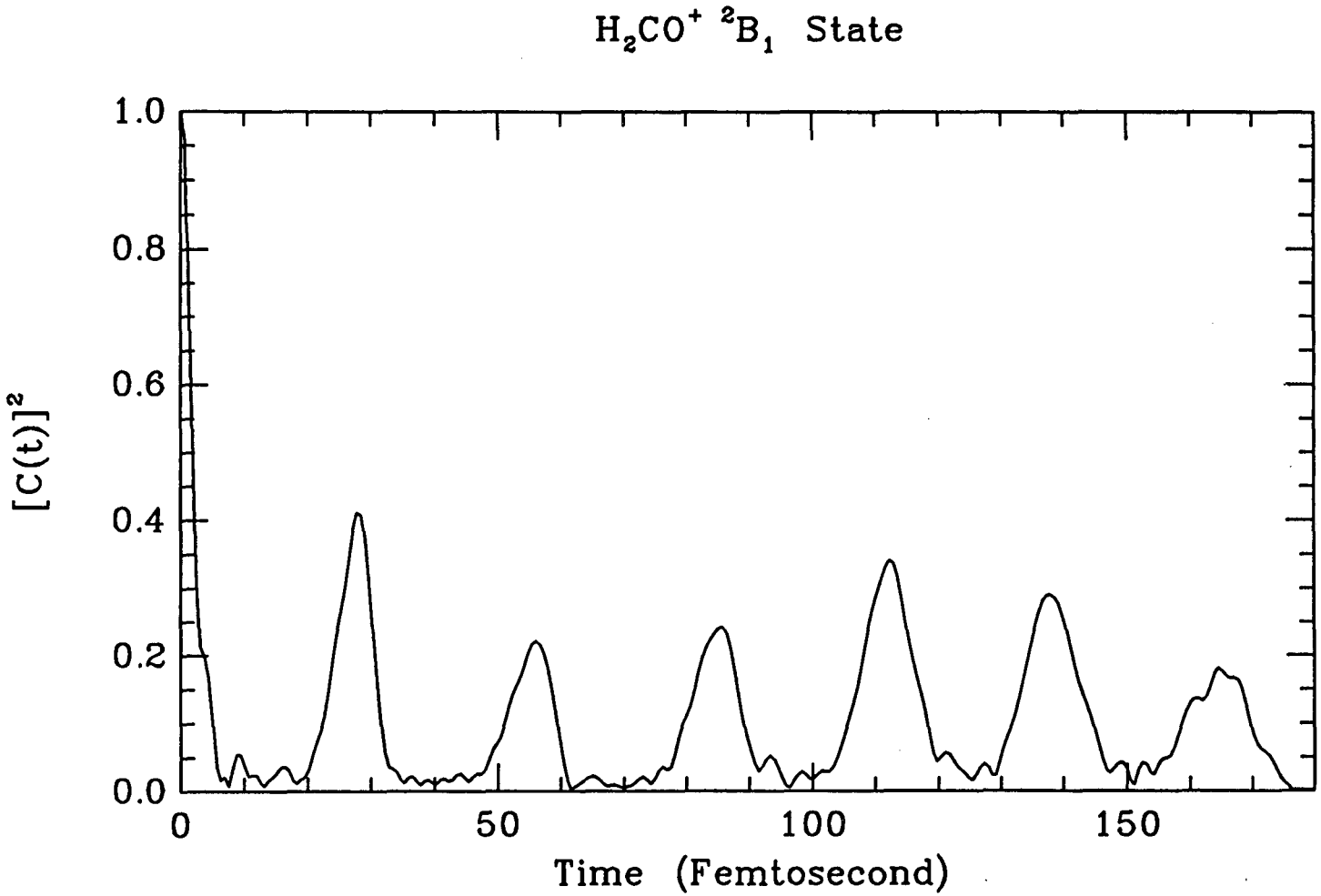
H_2CO^+ $^2B_1$ State
1.0
0.8
0.6
0.4
0.2
0.0
$[C(t)]^2$
0
50
100
150
Time (Femtosecond)

Figure 9 (top)

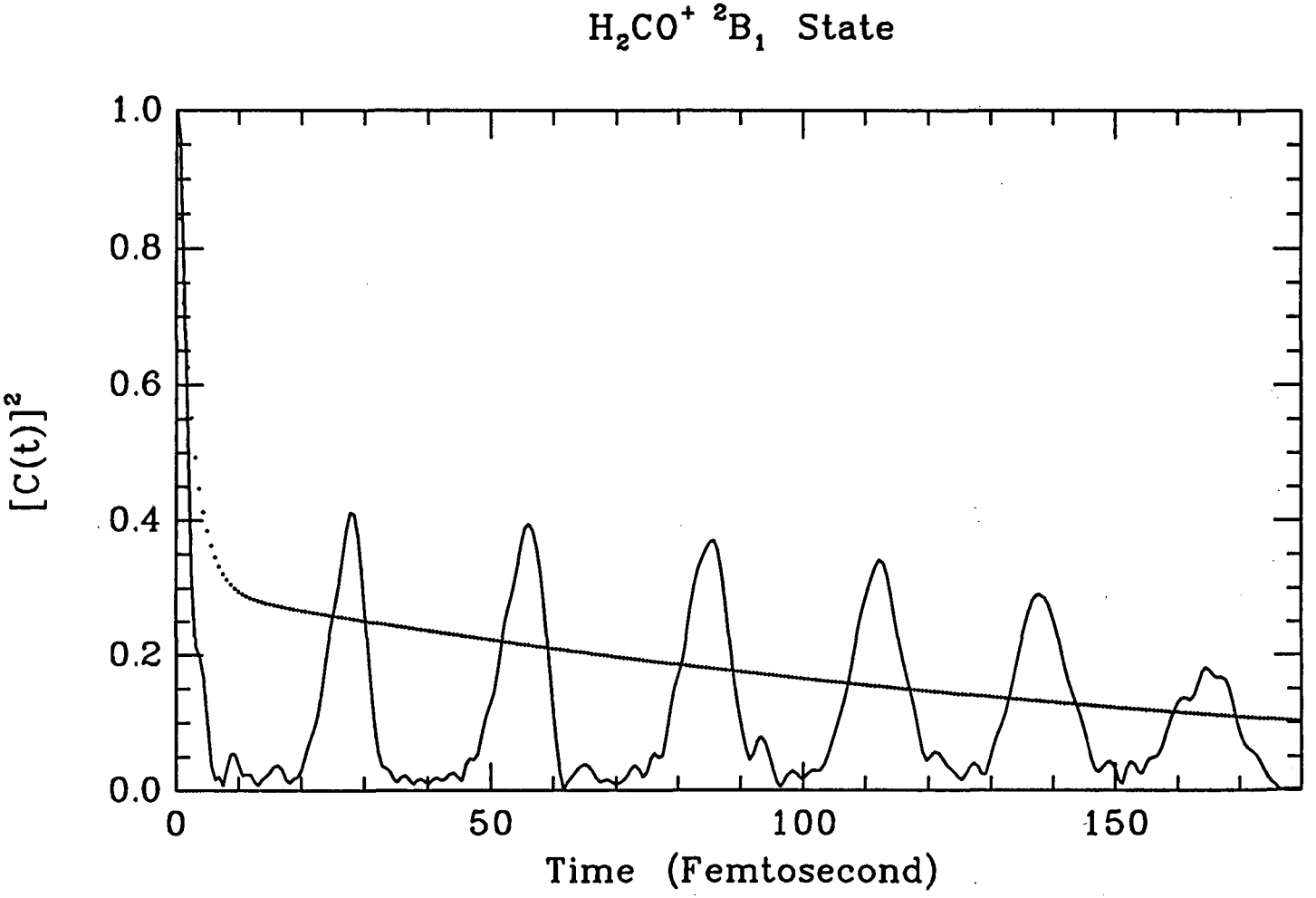

Figure 9 (bottom)

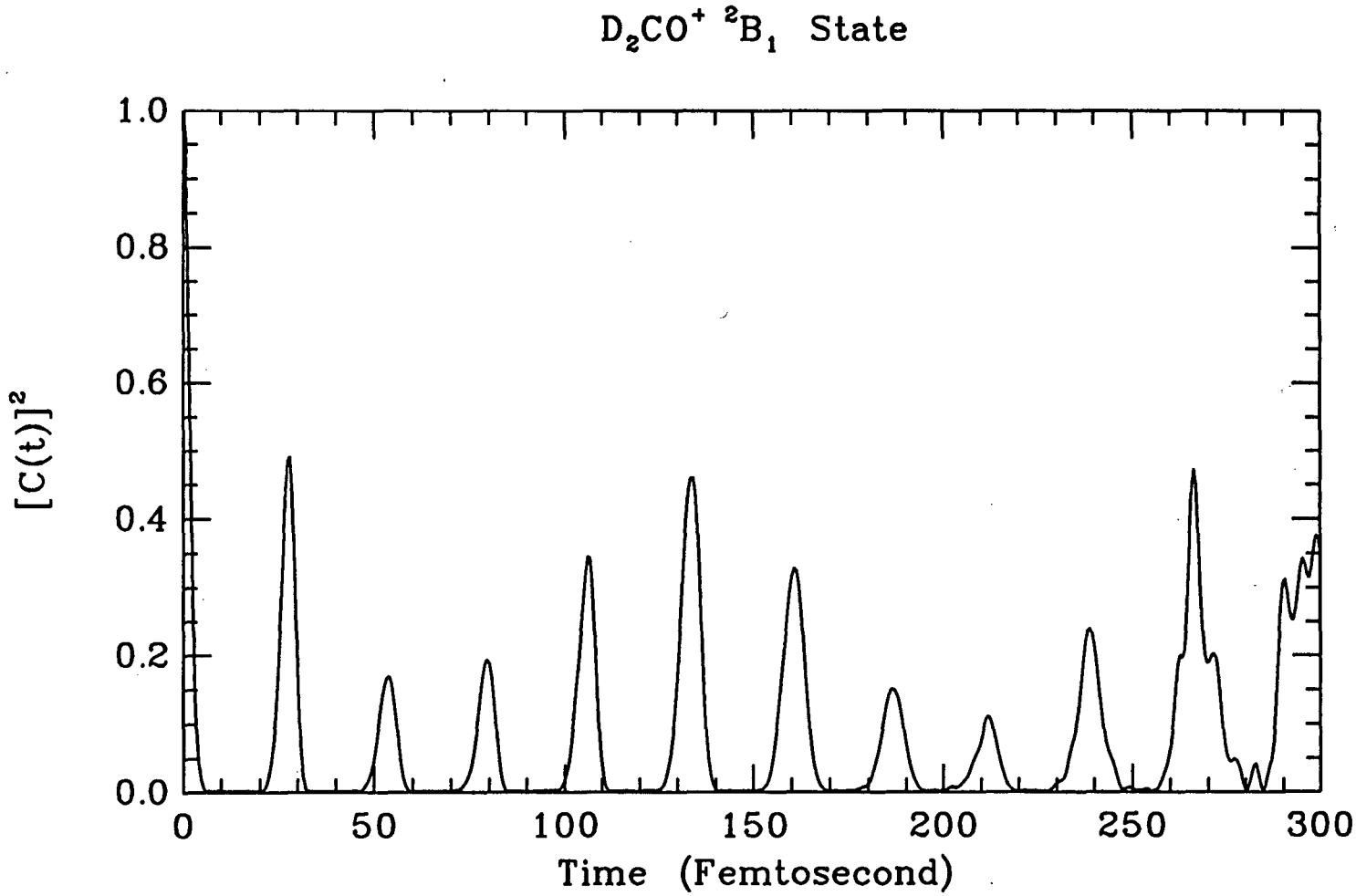

Figure 10 (top)

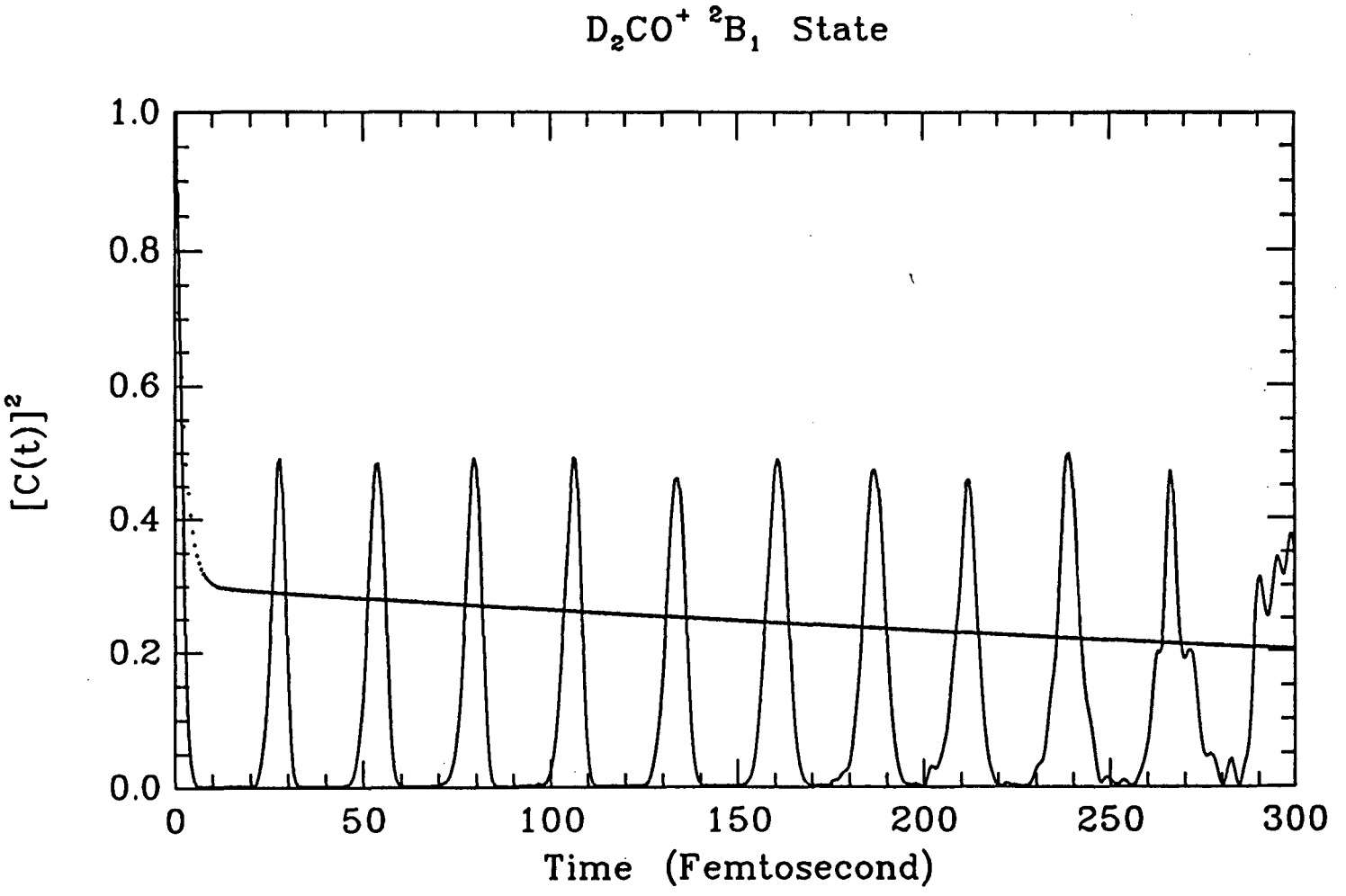

Figure 10 (bottom)

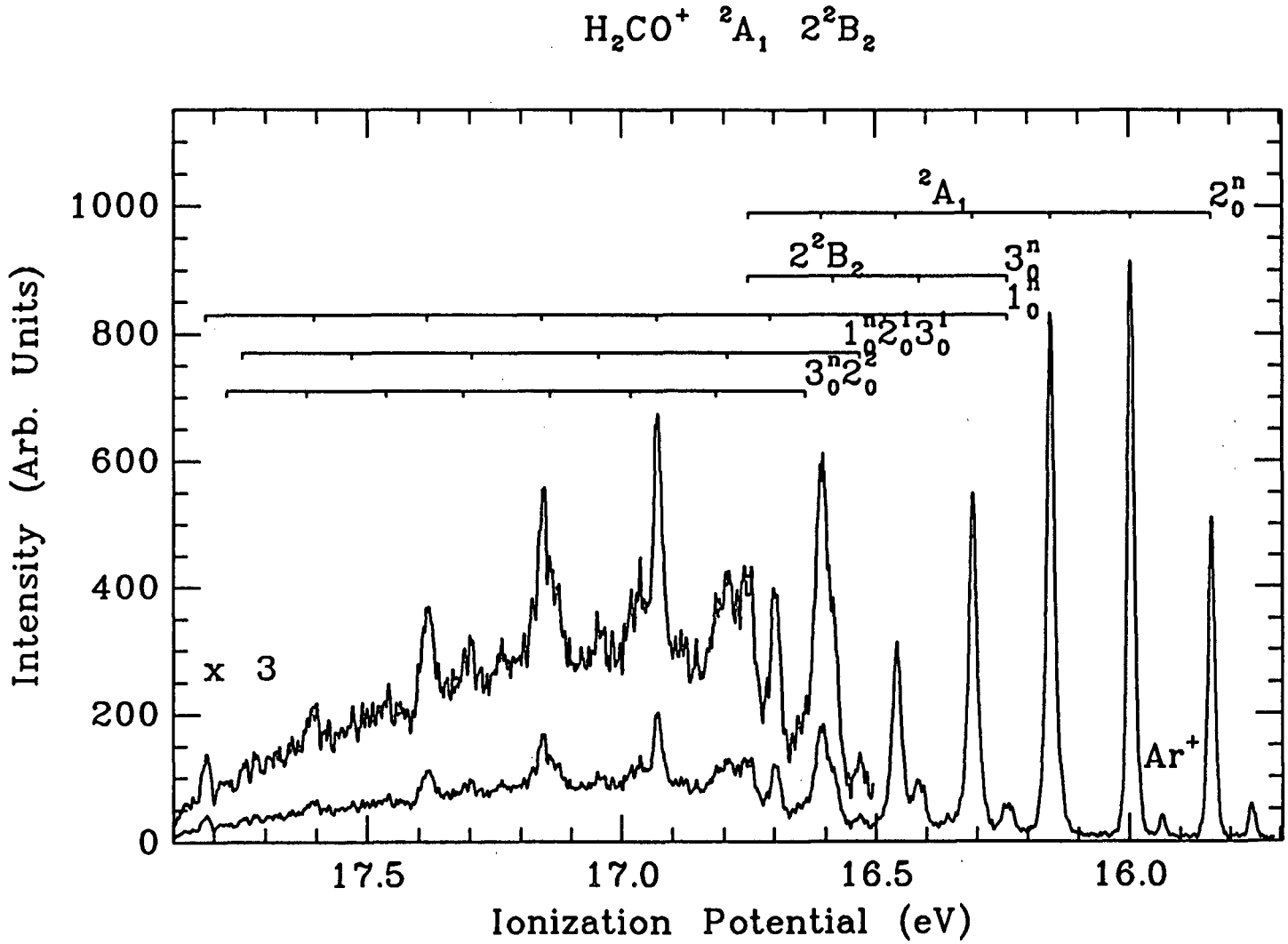
H_2CO^+ $^2A_1$ 2^2B_2
$^2A_1$
2^n_0
2^2B_2
3^n_0
1^n_0
$1^n_0 2^1_0 3^1_0$
$3^n_0 2^2_0$
x 3
Ar^+
Intensity (Arb. Units)
1000
800
600
400
200
0
17.5
17.0
16.5
16.0
Ionization Potential (eV)

Figure 11

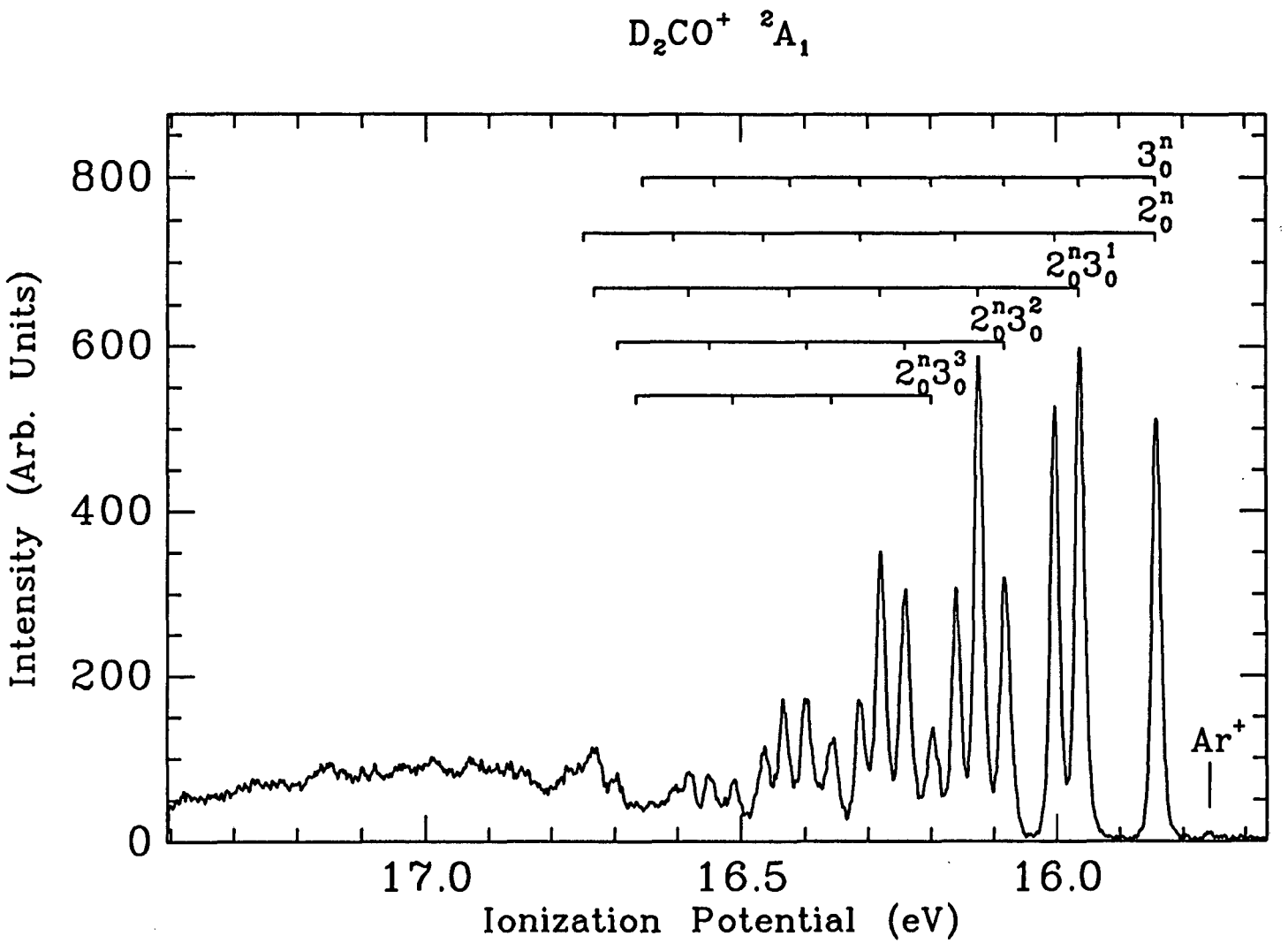
D_2CO^+ $^2A_1$
800
600
400
200
0
Intensity (Arb. Units)
17.0
16.5
16.0
Ionization Potential (eV)
3_0^n
2_0^n
$2_0^n3_0^1$
$2_0^n3_0^2$
$2_0^n3_0^3$
Ar^+

Figure 12

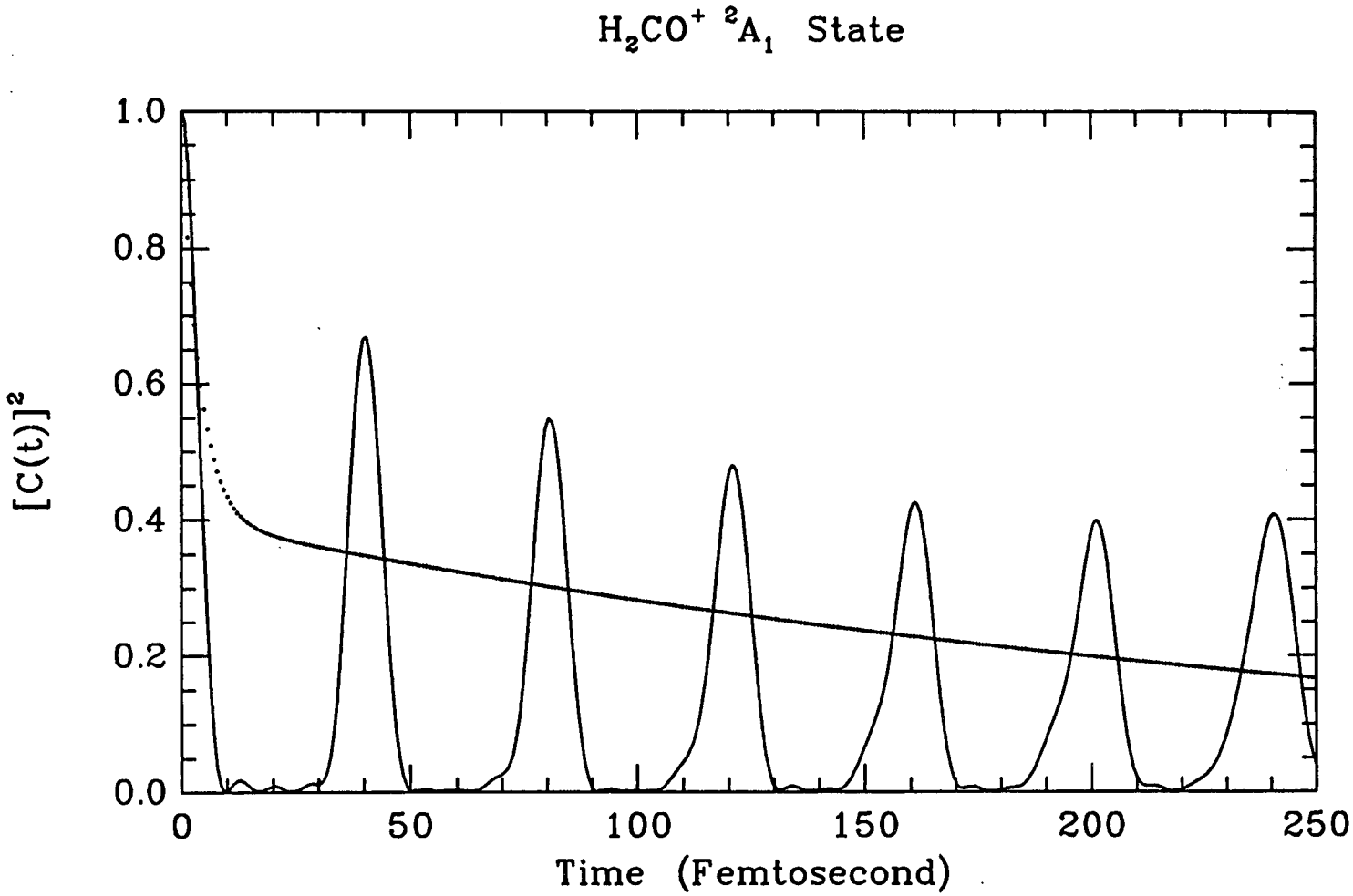
H_2CO^+ $^2A_1$ State
1.0
0.8
0.6
0.4
0.2
0.0
$[C(t)]^2$
0
50
100
150
200
250
Time (Femtosecond)

Figure 13

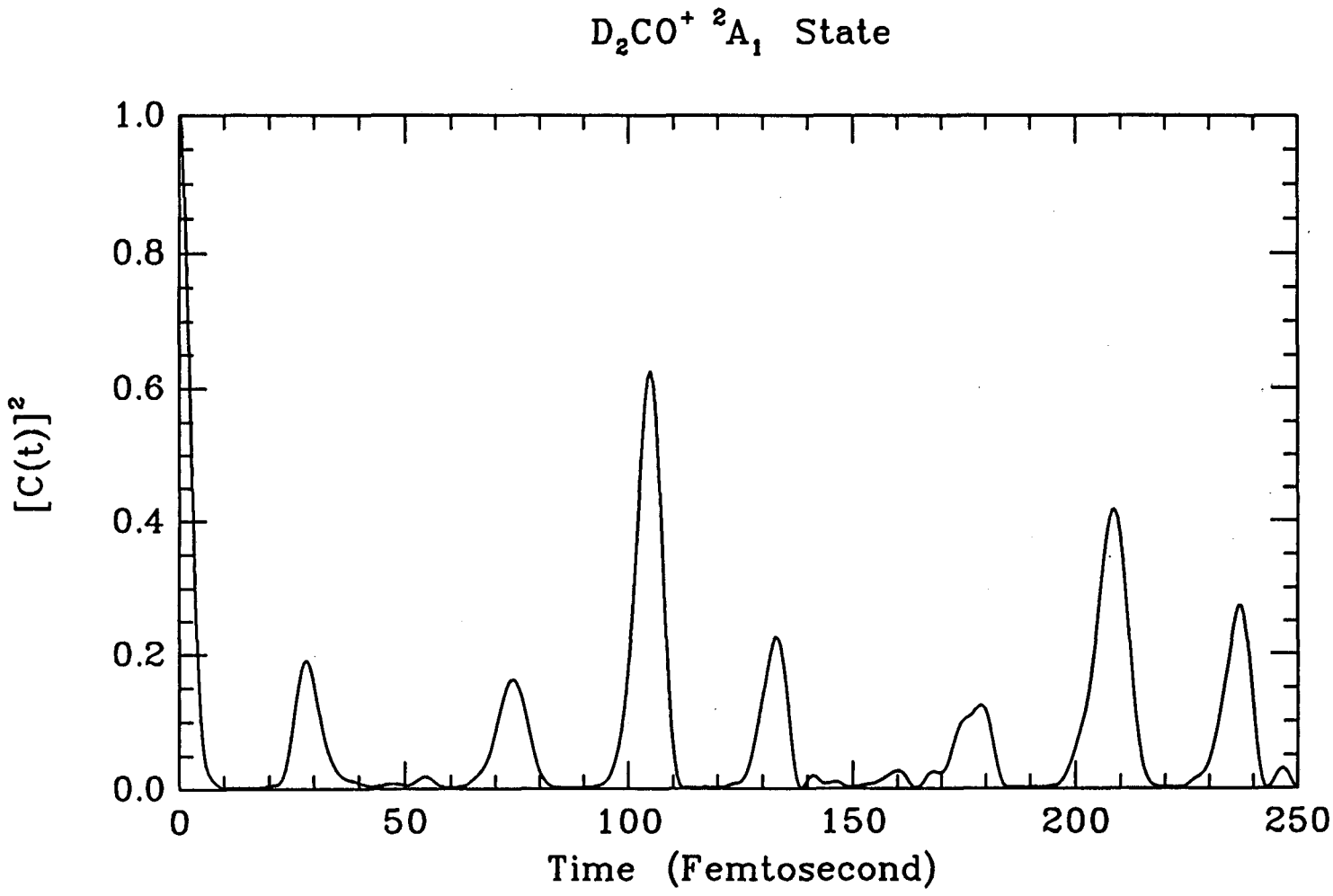
D_2CO^+ $^2A_1$ State
1.0
0.8
0.6
0.4
0.2
0.0
$[C(t)]^2$
0
50
100
150
200
250
Time (Femtosecond)

Figure 14

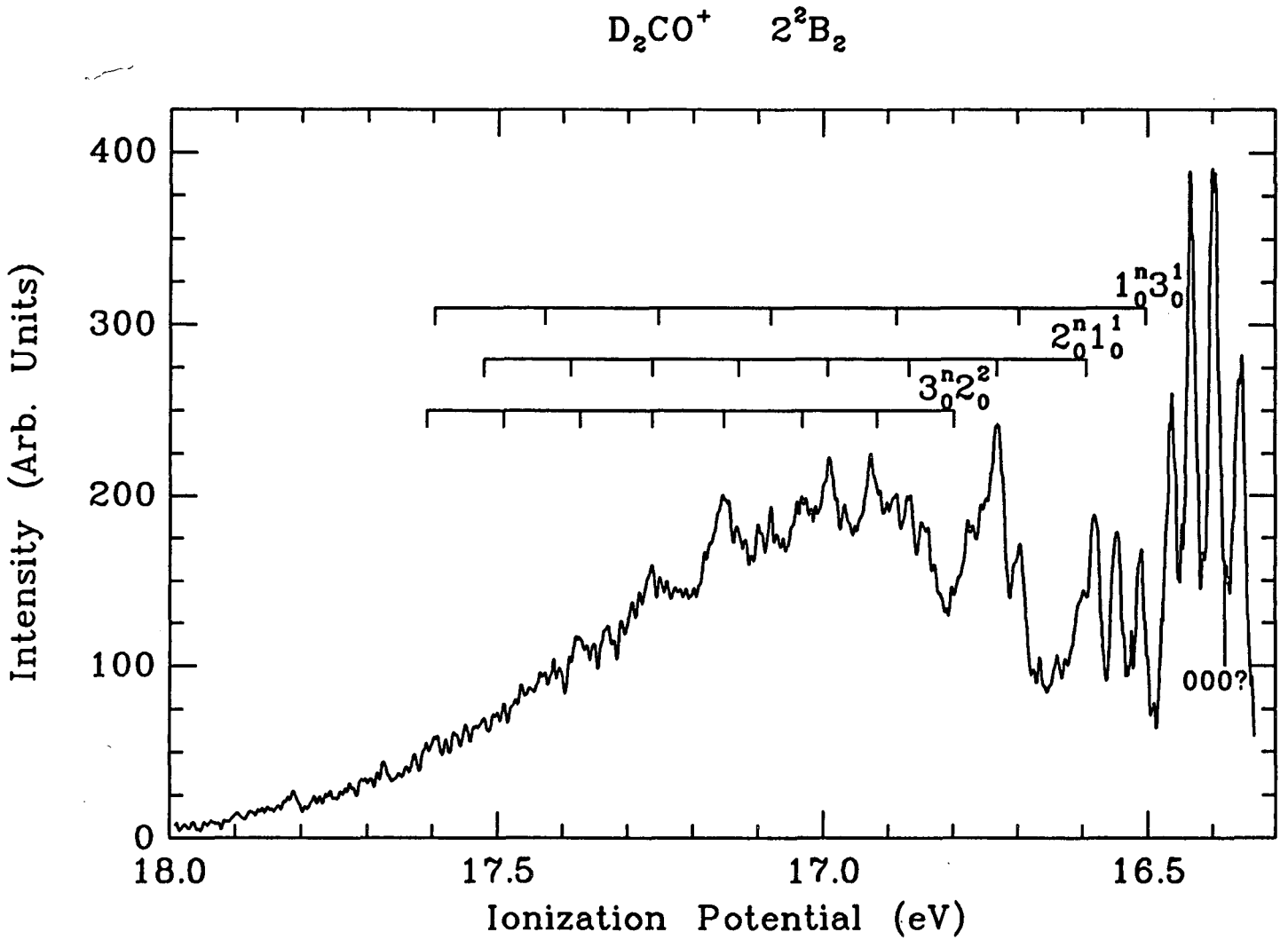
D_2CO^+ 2^2B_2
Intensity (Arb. Units)
400
300
200
100
0
18.0
17.5
17.0
16.5
Ionization Potential (eV)
$1_0^n 3_0^1$
$2_0^n 1_0^1$
$3_0^n 2_0^2$
000?

Figure 15

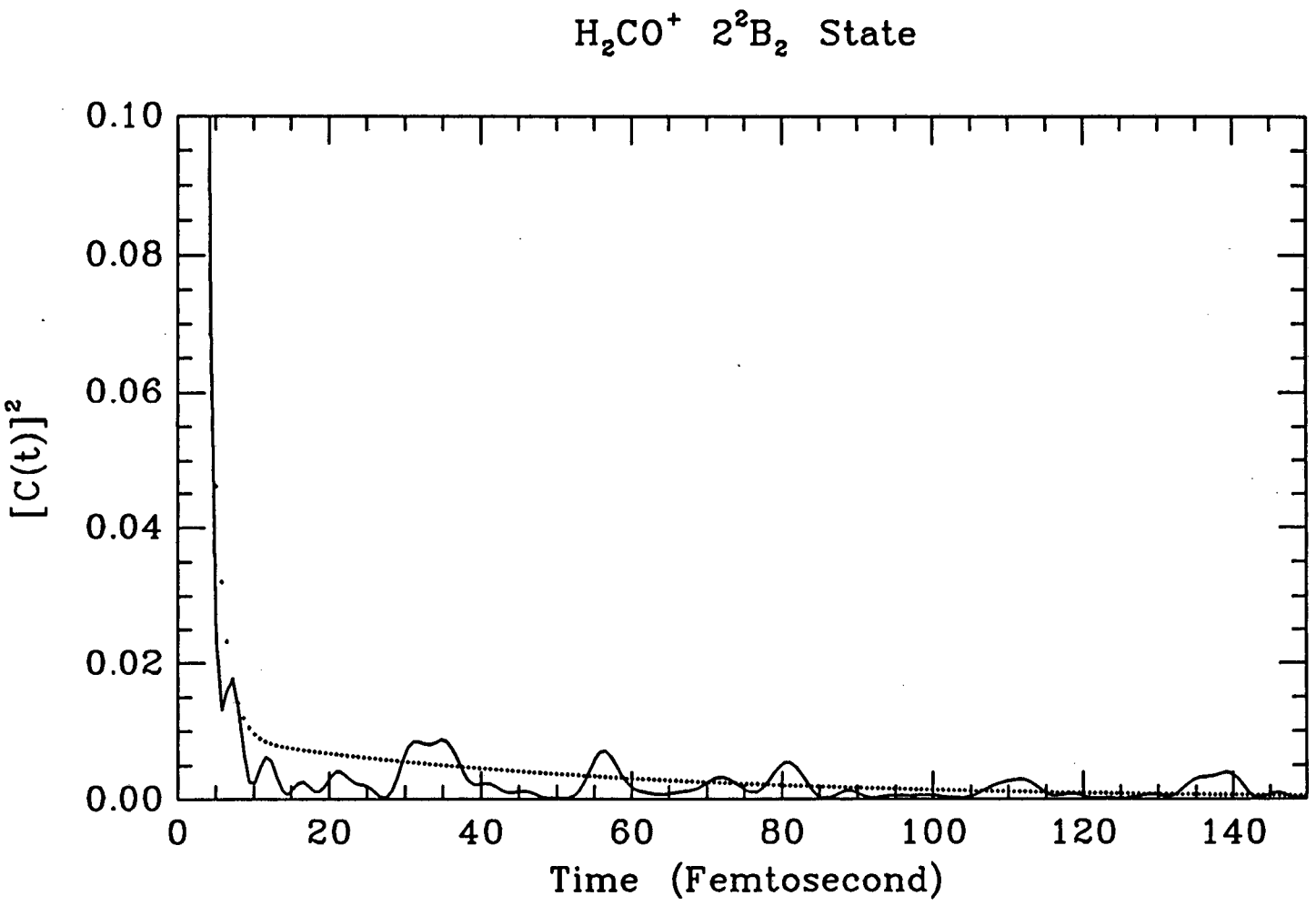
H_2CO^+ 2^2B_2 State
0.10
0.08
0.06
0.04
0.02
0.00
$[C(t)]^2$
0
20
40
60
80
100
120
140
Time (Femtosecond)

Figure 16

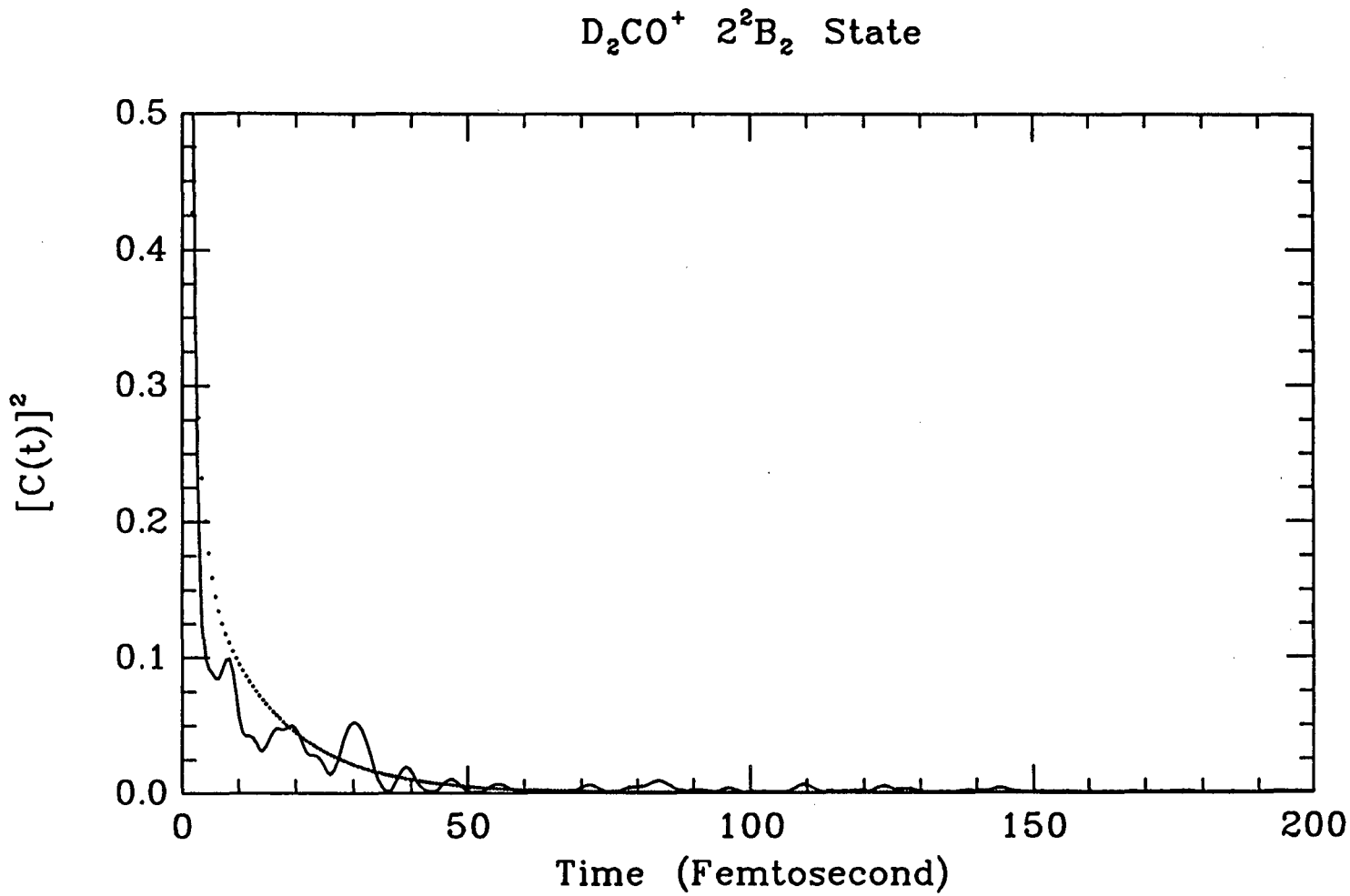
D_2CO^+ 2^2B_2 State
0.5
0.4
0.3
0.2
0.1
0.0
$[C(t)]^2$
0
50
100
150
200
Time (Femtosecond)

Figure 17

Chapter Four: High Resolution Photoelectron Spectroscopy and Femtosecond Intramolecular Dynamics of H_2CCO^+ and D_2CCO^+

A. Introduction

The photoelectron spectra of ketene and deuterated ketene have been the subject of extensive experimental and theoretical studies. [1-5] Baker et al. [1] was the first group to obtain the helium Iα (21.21732 eV) resonance line photoelectron spectrum of ketene and D_2-ketene. The vibrational fine structures unveiled in this study were partially explained by the then-available theoretical calculations. Hall et al. [4] studied the ketene and D_2-ketene photoelectron spectrum using both helium Iα and helium IIα (40.81369 eV) resonance lines. The assignments of the adiabatic ionization energies (AIE), the vertical ionization energies (VIE), and some vibrational fine structure analysis were also given. [1-5] The theoretical works have been largely based on these two experimental studies. Very recently, in an ***ab initio*** study of ketene and D_2-ketene, Takeshita [6] has given a detailed theoretical analysis on the photoelectron spectra of ketene and D_2-ketene and the vibrational analysis of the fine structures observed in the experimental studies of Baker and Hall. However, the disparity between the experimental and theoretical results is substantial. Especially in the second band (the ionic first excited $\tilde{A}\ 1^2B_2$ state), the sharp onset observed in the photoelectron spectrum can not be reproduced by the theoretical calculation. Hall et al. proposed that the complexity of this band might be due to the predissociation of ketene. Takeshita, on the other hand, showed that ketene cation in the $\tilde{A}\ 1^2B_2$ state is stable. He suggested that the complexity might be caused by the superposition of peaks associated with the $\tilde{X}\ 1^2\Pi_g$ band of CO_2^+ and with the second excited $\tilde{B}\ 2^2B_1$ state of ketene. The simplicity of the theoretical band compared with the experimental one was attributed to the near degeneracy of vibrations (**Fermi** resonances), $\nu_2 \approx 2\nu_4$, and

$\nu_2 \approx \nu_3 + \nu_4$, and might also be attributed to the inadequacy of the theoretical calculation caused by the neglecting of the anharmonicity and the couplings among the vibrations. There were clearly disagreements between the vibrational progression length observed in the experiments and the theoretical calculations. There are extensive studies [45] on the photochemistry and unimolecular dissociation dynamics on the neutral ketene molecule. The photochemistry and unimolecular dynamics of ketene cations have not attracted much attention so far.

In this work, we report the high resolution (FWHM 11.5 meV) helium Iα photoelectron spectra of H_2CCO and D_2CCO. Improved resolution and effective cooling of the sample by supersonic expansion enabled us to determine the adiabatic ionization potentials for the states accessible by the helium Iα resonance line (21.21732 eV) to a much higher accuracy and to give new interpretations of the vibration structures observed. The results compared very favorably with the very recently ***ab initio*** calculation by Takeshita, although, there are clearly some disagreements between the theoretically calculated spectra and the experimentally observed ones. Using the autocorrelation function formalism first discussed by Heller [7-10] for electronic photon absorption and emission, later by Lorquet et al. [11-14] and by Ruščić [13] for photoelectron spectroscopy, and modified by Pollard et al. [15] and Reutt et al.; [16,17] the femtosecond ultrafast intramolecular dynamics of the ketene cation in its various ionic states is discussed.

The details of the experiments are described in section B of this chapter. The vibronic coupling and isotope effects on vibronic coupling are discussed briefly in section C. A description and the method for calculating the vibrational autocorrelation function are presented in section D. Spectroscopic results and the dynamic interpretations based on the vibrational autocorrelation function are discussed for each of the electronic states of H_2CCO^+ and D_2CCO^+ in section E. The major conclusions are summarized in Section F.

B. Experiment

The molecular beam photoelectron spectrometer used for this study has been described in great detail by Pollard et al. [18,19] and by Reutt et al. [20] Briefly, it consists of a differentially pumped supersonic molecular beam source for the introduction of the sample into the main chamber where ionization takes place; a differentially pumped windowless helium discharge lamp optimized to produce only the helium Iα resonance line with minor contamination from higher resonances lines; a differentially pumped quadrupole mass spectrometer (QMS) to characterize the beam composition; a differentially pumped high resolution electron energy analyzer consisting of a 90° spherical sector prefilter, a 180° hemispherical analyzer equipped with a multichannel detector, and associated electron optics; and a dedicated microcomputer (LSI-11/73) for data acquisition and control. The electrons are collected at a 90° angle with respect to the incident photon beam and the supersonic molecular beam and the intensity is uncorrected for angular distribution effects, since there are no ketene ß values for helium Iα photons available.

Approximately 300 torr of ultra high purity helium (99.9999 %, Matheson) was first passed through a U tube maintained at LN_2 temperature to remove trace amounts of water and other impurities in the carrier gas line, then bubbled through liquid monomer H_2CCO or D_2CCO maintained at Hexane/LN_2 slush temperature (- 96 °C) with vapor pressures about 50 torr and 45 Torr as measured with an MKS model 122AA-2000 Baratron. The monomer H_2CCO or D_2CCO was prepared following a literature procedure [21-23] by thermodecomposition of acetic anhydride and d_6-acetic anhydride(**Aldrich**, 99.5% D-atom) at approximately 550 °C, trapping the acetic acid byproduct at - 78 °C using dry ice/acetone slush and trapping ketene at LN_2 (-195.8 °C) temperature. Ketene prepared in this way was vacuum distillated once from a hexane/LN_2 slush temperature to LN_2 temperature to remove trace amounts of acetic acid left and carbon dioxide, the primary byproduct from ketene decomposition. Purified ketene and D_2-ketene were kept in

the dark at LN_2 temperature under continuous pumping until the photoelectron measurements started.

The He/H_2CCO or He/D_2CCO mixture with a total pressure of approximately 400 Torr was expanded through a 70 μm diameter converging molybdenum nozzle held at room temperature, skimmed by a 0.858 mm diameter, 6.4 mm tall conical stainless steel skimmer, D_{ns} = 6.4 mm. The beam source chamber pressure was 6×10^{-5} torr, and the main chamber pressure was 3×10^{-6} torr during the experimental measurements. All gas inlet lines were minimized and extensively baked (200 °C) under vacuum (10^{-7} torr) to remove trace amounts of water. Beam compositions were checked by the quadrupole mass spectrometer. No polymers of H_2CCO or D_2CCO or CO_2 decomposition byproduct were found in the beam under these experimental conditions. The rotational temperature in the beams was estimated to be ≈ 5 Kelvin as shown by **LIF** measurements under similar conditions. [24-26]

The complete photoelectron spectrum of each isotopic species was obtained as five sequential scans of the electron kinetic energy. Each scan was preceded and immediately followed by an argon calibration scan. To enhance statistics, four complete sets of spectra of H_2CCO were scanned and summed. Thus the reported photoelectron bands each represent the summation of four such scans. Individual scans were made within a time period of less than two hours. The presented D_2CCO photoelectron spectra were the summation of four such sets of scans as well. Restricting the length of each scan limits the total drift in the electron kinetic energy scale to ≤ 1 meV. The linearity of the kinetic energy scale was determined by obtaining the N_2^+ photoelectron spectrum and comparing the N_2^+ $\tilde{X}$ $^2\Sigma_g^+$ v=0 and $\tilde{B}$ $^2\Sigma_u^+$ v=0 splitting with the accurate literature value of 3.16981 eV available from N_2^+ optical emission spectroscopy. [27] At higher kinetic energies, the linearity of the energy scale was checked by the photoelectron spectra of argon and xenon. The ionization potentials of these rare gases (I.P. Ar $^2P_{3/2}$ = 15.75975 eV, and Xe $^2P_{3/2}$ = 12.13000 eV)

have been precisely determined from optical spectroscopy.[28] The linearity of the molecular beam spectrometer is within ±1.0 meV over this entire energy range. The combination of the drift and the linearity of the energy scale errors limit the accuracy at which the absolute ionization potentials may be reported to ± 3.0 meV. Other spectroscopic constants, however, are obtained as line splittings and may be reported to a much higher accuracy of ± 0.5 meV.

C. Vibronic Coupling and Isotope Effects on Vibronic Coupling

In photoelectron spectroscopy, the vibronic coupling effect , that is the interaction of the electronic and nuclear (vibrational) motion, is often invoked to explain the observations that there are vibrational progressions in modes that are not allowed by the selection rules based on the **Born-Oppenheimer** approximation; [29] that the observed vibrational frequencies are very low; and that odd quanta of non totally symmetric vibrations get excited. There are other couplings and resonances effects that can also cause similar effects, like vibrational-rotation coupling, rotation-electronic couplings and **Fermi** resonances. In general, these effects are much smaller than the vibronic coupling effect and are much easier to identify.

The vibronic coupling effects are usually treated as perturbations to the **Born-Oppenheimer** approximation; that is, the adiabatic Hamiltonian $\mathcal{H}_0$. [30] We can expand the molecular Hamiltonian $\mathcal{H}(q;Q)$, which is a function of the electronic q and the nuclear (normal) Q coordinates, in a Taylor series in the normal coordinates of vibration Q near the equilibrium configuration Q_0:

$$\mathcal{H} = \mathcal{H}(q;Q)_{Q_0} + \sum_{r=1}^{\infty} \left| \frac{1}{r!} \frac{\partial^r \mathcal{H}(q;Q)}{\partial Q^r} \right|_{Q_0} Q^r + \cdots \tag{4.1}$$

The first term in equation (3.1), $\mathcal{H}(q;Q)_{Q_0}$, is called the zero-order Hamiltonian, that is the **Born-Oppenheimer** adiabatic Hamiltonian, and is usually expressed as $\mathcal{H}_0$. Applying the total Hamiltonian $\mathcal{H}$ on the molecular wave function Ψ yields:

$$<\Psi|\mathcal{H}|\Psi> = E_0 + E_1 + E_2 + \ldots \tag{4.2}$$

Where E_0 is the non-perturbed energy, and E_1, E_2 are the perturbation energies resulting from the linear and quadratic expansion terms in equation (4.1) respectively. The coupling of two wave functions Ψ_k and Ψ_j can be expressed according to the matrix elements:

$$<\Psi_k|\mathcal{H}\,|\Psi_j> \tag{4.3}$$

which can be expanded with the Hamiltonian $\mathcal{H}$ of equation (4.1),

$$<\Psi_k|\mathcal{H}\,|\Psi_j> = <\Psi_k|\mathcal{H}_0\,|\Psi_j> + \sum_r Q_r \langle\Psi_k\left|\frac{\partial\mathcal{H}}{\partial Q_r}\right|\Psi_j\rangle +$$

$$+\frac{1}{2!}\sum_r Q_r^2 \langle\Psi_k\left|\frac{\partial^2\mathcal{H}}{\partial^2 Q_r^2}\right|\Psi_j\rangle + \frac{1}{2!}\sum_{rs} Q_r Q_s \langle\Psi_k\left|\frac{\partial^2\mathcal{H}}{\partial Q_r \partial Q_s}\right|\Psi_j\rangle + \ldots \tag{4.4}$$

The first term in equation (4.4) is always zero by the orthogonality relationship. Thus the necessary condition for the vibronic coupling effects to perturb the electronic states involved is that at least one term in equation (4.4) has a nonzero value that is not too small compared with the zero-order electronic states' energy separations.

The total Hamiltonian $\mathcal{H}$ of equation (4.1) always possesses the full symmetry of the molecular point group and transforms as Γ_1. This is also true for $\mathcal{H}_0$, the Hamiltonian for the zeroth-order unperturbed molecule. For the coupling operators in equation (4.4):

$\partial\mathcal{H}/\partial Q_r$ transforms as the irreducible representation of the normal coordinate Q_r, $\Gamma(Q_r)$; $\partial^2\mathcal{H}/\partial^2 Q_r$ always has at least one component that transforms as Γ_1, the full symmetry of the molecular point group; and $\partial^2\mathcal{H}/\partial Q_r\partial Q_s$ transforms as $\Gamma(Q_r)\otimes\Gamma(Q_s)$. The linear coupling integral in equation (4.4) will be finite if the product of the representations of all species in the integral contains the totally symmetric representation, Γ_1, that is:

$$\Gamma(\Psi_k)\otimes\Gamma(\Psi_j)\otimes\Gamma(\partial\mathcal{H}/\partial Q_r) \subset \Gamma_1. \tag{4.5}$$

This will enable the Q_r normal vibrational mode to couple and mix the Ψ_k and Ψ_j electronic states. If Ψ_k and Ψ_j are degenerated states, then Q_r is the asymmetric vibrational mode that will remove the degeneracy. We can discuss the two quadratic terms in equation (4.4) similarly. The linear terms are usually much larger than the quadratic terms, and the quadratic terms are normally neglected when the linear terms are nonzero. In a polyatomic molecule, there could be more than one normal mode Q_r that satisfies the condition of equation (4.5). Those normal modes that satisfy equation (4.5) are called vibronically active modes. When there are more than one mode that are vibronically active, multimode vibronic coupling effects will occur. In general, these are more complicated to deal with. Multimode vibronic effects and their influence on spectroscopy have been reviewed in detail by Köppel et al. [31]

It can be seen from equation (4.4) that both the linear and quadratic vibronic couplings depend on the normal coordinates that are mass-dependent. It is expected that the couplings will be different for isotope-substitued compounds in the same electronic state. One important consequence of this effect is that it is possible for different vibration modes to be excited to a different extent for isotope-substituted compounds. This will cast new difficulties in the interpretation of photoelectron spectra of isotopic compounds.

Theoretical calculations have shown that this effect appears in isotope-substituted compounds. [32,33] The H_2CCO^+ and D_2CCO^+ photoelectron spectra have shown this kind of behavior, and they will be discussed further in section E of this chapter.

D. The Correlation Function

The autocorrelation function formalism description of the intramolecular dynamic process gives complementary information to time-dependent measurements. Lorquet et al.. [11-14] first demonstrated how this can be done for photoelectron bands using the formalism of Heller. [7-10] A variation on the method of Lorquet et al. was used by Pollard et al., [15] and by Reutt et al. [16,17] to study the dynamic characteristics of intramolecular processes using supersonic molecular beam photoelectron spectroscopy. Ruščić [28b] has also given the analytical form of the vibrational autocorrelation function for photoelectron bands under the harmonic approximation for vibrational motions.

Very recently, Remacle et al. [14] have suggested that there exists a relationship between the vibrational autocorrelation function C(t) and the population decay function **P**(t) of a particular electronic state. They defined an average population decay curve $\mathbf{P}_{av}(t)$ valid in a particular time period and $C_{av}(t)$, the average correlation function, obtained from C(t). It was pointed out by the authors that for a specific excitation, the exact initial rate of decay of $\mathbf{P}_{av}(t)$ (valid up to the dephasing time T_1) is equal to the initial rate of decay of $|C(t)|^2$, and the subsequent time evolution of $\mathbf{P}_{av}(t)$ can be obtained from $|C_{av}(t)|^2$ values that are derived by averaging $|C(t)|^2$ over its oscillation. To a good approximation, the average population decay curve $\mathbf{P}_{av}(t)$ can be obtained by multiplying $|C_{av}(t)|^2$ with an appropriate constant: i.e., the slopes of the two curves are the same.

The autocorrelation function can be expressed as

$$C(t) = |\langle\phi(0)|\phi(t)\rangle|. \tag{4.6}$$

Here $\phi(0)$ is the initial nuclear wavefunction, and $\phi(t)$ is the time evolution of this wavefunction on the excited state potential-energy surface. C(t) represents the probability amplitude that at time t the system remains in the initially prepared state. It must be noted that the correlation function is the measure of the time evolution of the initial wave packet on the excited-state potential energy surface and not a measure of the excited state population. But, as mentioned in the preceding paragraph, the initial decay rate of C(t), through $|C(t)|^2$, is the same as the average population $P_{av}(t)$ initial decay rate. It is dominated by the dephasing of the initial wave packet due to the different shape of the excited-state potential energy surface. Only at times greater than a vibrational period will radiationless decay processes appear in the correlation function time evolution. The derivation of the autocorrelation function C(t) from photoelectron spectroscopy experimental data has been reported; [12] only the principal points will be outlined here. The form of photoionization cross section under the strict **Franck-Condon** approximation [34] can be expressed as

$$\sigma(E) \propto \left| |M_{el}(Q,E)|^2 |\langle \Psi'' | \Psi' \rangle|^2 \right| \tag{4.7}$$

Here $M_{el}(Q, E)$ is the pure electronic transition moment that is a function of the nuclear coordinates Q and electron kinetic energy E, and Ψ'' and Ψ' are the initial- and final-state vibrational wave functions. The electronic transition moment varies slowly over the photoelectron band. In lieu of any arbitrary approximation, a constant value was used in calculating the correlation functions reported here.

Applying the completeness conditions of a set of eigenstates Ψ'' of the molecular Hamiltonian and invoking the analytical form of the Dirac δ function, it has been shown [12] that the cross section for photoionization becomes

$$\sigma(E) \propto \frac{1}{2\pi} \int_{-\infty}^{+\infty} e^{iEt/\hbar} \langle \Psi'' | e^{-i\mathcal{H}t/\hbar} | \Psi'' \rangle \, dt \tag{4.8}$$

Here $\mathcal{H}$ is the molecular Hamiltonian, Ψ'' is identified as the initial nuclear wave function $\phi(0)$, and $e^{-i\mathcal{H}t/\hbar}|\Psi''\rangle$ is the nuclear wave function at time t: $\phi(t)$. This gives

$$\sigma(E) \propto \frac{1}{2\pi} \int_{-\infty}^{+\infty} e^{iEt/\hbar} \langle \phi(0) | \phi(t) \rangle \, dt \tag{4.9}$$

and the correlation function can be obtained by a **Fourier** transformation of the cross section

$$C(t) = |\langle \phi(0) | \phi(t) \rangle| \propto \frac{1}{2\pi} \int_{-\infty}^{+\infty} \sigma(E) \, e^{-iEt/\hbar} \, dt \tag{4.10}$$

It can be seen from this equation that the correlation function can be obtained from the **Fourier** transform of the photoelectron partial cross section $\sigma(E)$. This can be accomplished by deconvoluting the instrument response function $\mathbf{I}(E)_{ir}$, which we determine from the photoelectron spectrum of a rare gas at a kinetic energy comparable to the band of interest, from the quantity $\mathbf{I}(E)$, intensity vs. energy, which we measure in photoelectron spectroscopy. The contributions of the finite rotational temperature in a supersonic molecular beam experiment (typically ~ 5-10 Kelvin) and the rotational excitations contribution to the correlation function were removed by convoluting $\mathbf{I}(E)_{ir}$ with a gaussian function $\mathbf{I}(E)_g$ to generate a rotationally broadened instrument response function. The width of the gaussian function was chosen from the average rotational

constant , $\mathbf{B_{avg}}$, of the molecular ion for the particular electronic state (if available), the finite rotational temperature, and the rotational selection rules for photoionization. Ruščić [13] has taken a different approach to account for all the corrections. However, both methods give essentially the same results in the time window of interest.

The procedure for calculating the correlation function of $\tilde{X}$, $\tilde{A}$, $\tilde{B}$, $\tilde{C}$, $\tilde{D}$, and $\tilde{E}$ states of ketene and d_2-ketene is the following. First, the band of interest was isolated (in the case of $\tilde{A}$ and $\tilde{B}$ states, they were digitally separated to remove the overlapping of these two bands. The heavy overlapping of the $\tilde{C}$ and $\tilde{D}$ states, however, renders such separation impractical, and was not attempted), and the empirically determined background, plus any constant background was then removed. The resulting band was then normalized (area = 1) and **Fourier** transformed using a discrete **FFT** algorithm. [35] The instrument response function was similarly normalized and convoluted with a Gaussian of 3 meV (FWHM). The resulting function was **Fourier** transformed and divided into that of the data. Finally, the modulus of the previous result was calculated which gave the correlation function. The procedure can be summarized by the following equation:

$$C^{vib}(t) = |\langle\phi(0)|\phi(t)\rangle| = \left| \int_{-\infty}^{+\infty} \mathbf{I}(E)\, e^{-iEt/\hbar}\, dE \right| \div \left| \int_{-\infty}^{+\infty} \mathbf{I}(E)_{ir}\, e^{-iEt/\hbar}\, dE \;\mathrm{X}\; \int_{-\infty}^{+\infty} \mathbf{I}(E)_{g}\, e^{-iEt/\hbar}\, dE \right| \qquad (3.11)$$

Then $|C(t)|^2$ was then calculated, and $|C_{av}(t)|^2$ was evaluated by fitting $|C(t)|^2$ with an exponential curve of the form Ae^{-ikt} for both the initial drop and the subsequent decay after the first 'vibrational' period.

E. Results and Discussions

The full photoelectron spectra of H_2CCO^+ and D_2CCO^+ obtained by combining four separate scans with a resolution of 11.5 meV FWHM (as measured with Ar $^2P_{1/2}$, $^2P_{3/2}$) are shown in Figure 1 and Figure 2, respectively. Table I summarizes the measured spectroscopic constants together with results reported in the literature. [38-40]

1. First Band, $\tilde{X}\ 1^2B_1$ State

The ground states of both H_2CCO^+ and D_2CCO^+ showed well-resolved vibrational fine structures, as presented separately in Figure 3 and Figure 4. Observed spectroscopic results are presented in Table II. In the present work, effective rotational cooling of the sample by supersonic expansion permits all of the observed vibrational levels to be determined with much improved accuracy, and the mean energies of these transitions were determined by the following least-squares fitting procedure. The adiabatic transitions (or the most intense feature) were first determined by fitting these features to Gaussians. The adiabatic peaks were then isolated and used as empirical functions to fit the successive levels. This procedure allows the values of the peak splittings to be determined to an accuracy of $\leq \pm 0.0005$ eV. The mean transition energies located through this procedure are listed for each of the bands observed. The vibrational levels for each normal mode were then least-squares fitted to the standard energy level expression of a Morse oscillator [36,37]

$$G_i^0(V) = \omega_i^0(V) - \omega_i^0 x_i^0(V)^2 \tag{4.12}$$

with the zero point energy being set to zero, ω_i^0 and $\omega_i^0 x_i^0$ are related to ω_i and $\omega_i x_i$ in the following ways: $\omega_i = \omega_i^0 + \omega_i^0 x_i^0$; $\omega_i x_i = \omega_i^0 x_i^0$. Here ω_i is the fundamental vibration frequency, and $\omega_i x_i$ is the quadratic anharmonicity constant for the ith normal vibration mode.

The result shows that at least two vibrational modes are strongly excited in this state of H_2CCO^+, and for D_2CCO^+ there are additional fine structures in one of the vibrational progressions which is not apparent from the H_2CCO^+ spectrum, indicating that there are more than two modes that are excited strongly. The abnormality in the intensity of the third peak of the $\tilde{X}\ 1^2B_1$ state of H_2CCO^+ and D_2CCO^+ was not explained in the original Baker paper and was not discussed in the study by Hall et al. either. Takeshita attributed this intensity abnormality to the superposition of the two possible vibrational levels, $\nu_2 = 1$ and $\nu_4 = 2$. The present study supports the theoretical calculation by noticing that $\nu_2 \approx 2\nu_4$, but the two peaks are not exactly superimposed. Instead, the abnormality of the intenstity of this peak was attributed to a **Fermi** resonances, in which one peak "borrows" intensity from its nearby neighbor. The weak excitation of the ν_3 mode in H_2CCO^+ was further established by the D_2CCO^+ spectrum, where a reduction in frequency was apparent for the excitation of the ν_3 mode which accounts for the doublet-like structure in the second, the fourth , and the sixth peaks in the D_2CCO^+ spectrum. This observation also indicates that the vibronic couplings of the two isotopic molecules in this state are different. This accounts for the strong excitation of the ν_3 mode in D_2CCO^+ compared with that of H_2CCO^+. In other words, the potential energy surfaces of the $\tilde{X}\ 1^2B_1$ state for H_2CCO^+ and D_2CCO^+ are different, especially along the Q_3 normal coordinate in the **Franck-Condon** region. The strong excitation of ν_2 and ν_3, ν_4 modes in the $\tilde{X}\ 1^2B_1$ state of H_2CCO^+ and D_2CCO^+ and the intensity of the adiabatic peak indicate that the electron being ejected is mostly from the non-bonding oxygen lone pair.

The vibrational autocorrelation functions calculated from the $\tilde{X}\ 1^2B_1$ state of each ion are shown in Figure 5 and Figure 6. Very similar oscillatory patterns are evident for each isotopic species. The beat pattern results from the phase relationship of a stable two-mode anharmonic oscillator system with $\nu_2 \geq 2\nu_4, 2\nu_3$. At shorter times a dephasing of the wave packet, due to the differences in the ionic and neutral potential energy surfaces,

dominates the correlation functions. After 10.4 fs for H_2CCO^+ (10.5 fs for D_2CCO^+) the fastest components of the wave packet return to the initial positions on the ionic potential energy surfaces and a reduced maximum of the correlation functions of 0.38 (0.42 for D_2CCO^+) is achieved. This corresponds very closely to one period of ν_2 vibration motion. The slower components of the wave packet, which must also travel along the ν_3, ν_4 coordinates, are expected to return to the initial position on the ionic potential energy surfaces after approximately one period of ν_4/ν_3 vibration motion. The observed maximums in the correlation functions of 0.78 at 30.5 fs and 0.83 at 30.8 fs for H_2CCO^+ and D_2CCO^+, respectively, are mainly attributed to this return. The small shifts in times of the observed peaks in the correlation functions arise from the spreading of the wave packet on the anharmonic potential energy surfaces and the relative phase relationships between the ν_2 and ν_3, ν_4 normal modes.

High correlation is maintained at longer times (> 0.3 at 200 fs), which indicates that the initially prepared wave packet is fairly stable regarding deformations along the Q_2 and Q_3/Q_4 normal coordinates. Relatively shallow minimums observed in the correlation function are the characteristics of the wave packet prepared through a predominately adiabatic transition. The initially prepared wave packet is mostly localized around the minimum of the upper potential energy surfaces along the Q_2 and Q_3/Q_4 normal coordinates, and weakly oscillates around this region, retaining substantially high level correlation at all times.

The isotope effect is also noticeable in the correlation functions, referring to Figure 7, where the correlation functions of the $\tilde{X}\ 1^2B_1$ state of H_2CCO^+ and D_2CCO^+ are plotted together. At shorter times it can be seen that the over all shapes and trends in the correlation function for both isotopic species are almost identical, indicating that the predominate characters of the normal vibration modes involved have very little contribution

from the CH_2 or CD_2 groups. At longer times, however, the differences between the correlation functions of the isotopic species are apparent. This can be attributed largely to the differences in the ionic potential energy surfaces between the isotopic species as indicated by the different anharmonicity constants for each normal mode.

2. The Second Band, $\tilde{A}\ 1^2B_2$ State

The second band of ketene for both isotopic species, which showed well-resolved vibrational fine structures albeit overlapped strongly with the third band $\tilde{B}\ 2^2B_1$ state, are presented in Figure 8 and Figure 9, which show the $\tilde{B}\ 2^2B_1$ state of both isotopic species as well. Observed spectroscopic constants for these states are summarized in Table III. In the present work, effective rotational cooling and the very high resolution achieved unveiled the details of the vibrational progressions in the $\tilde{A}\ 1^2B_2$ state for both isotopic species for the first time. The vibrational assignments for the $\tilde{A}\ 1^2B_2$ state are well established in the present study based on the ***ab initio*** calculation by Takeshita, except for the possible excitation of one other 'soft' mode which causes the doublet-like structures observed in the first few vibrational progressions of this band for both isotopic species. Hall et al. [4] explained the complexity of this band in terms of predissociation of the cation in this state, quoting no detectable emission from this state as an indication for the short life-time implied. Takeshita, however, in an ***ab initio*** calculation, showed that the cation in this state is stable, and the C_{2V} geometry is a true equilibrium configuration. He attributed the complexity of this band to the possible contamination from the $CO_2^+\ \tilde{X}\ ^2\Pi_g$ band near 13.8 eV and from the $\tilde{B}\ 2^2B_1$ state of ketene above 14.6 eV.

We can first eliminate the possibility of the $CO_2^+\ \tilde{X}\ ^2\Pi_g$ band contamination from the present spectrum of this band. The $CO_2^+\ \tilde{X}\ ^2\Pi_g$ band **AIE** is 13.7778 eV [41], and the 20 meV spin-orbital splitting present in the band would have been evident if there were any contributions from the $CO_2^+\ \tilde{X}\ ^2\Pi_g$ band. Also, experiments performed at hexane LN_2

slush (-96 °C) temperature (CO_2 vapour pressure ≤ 100 torr) and at acetone/dry ice slush (-78 °C) temperature (CO_2 vapour pressure ≥ 760 torr) showed no sign of changes in relative intensities for this band. This and the **QMS** diagnosis results establish that the ketene sample used for this study had not been contaminated by the dissociation of ketene by-product CO_2. The contributions from the $\tilde{B}\ 2^2B_1$ band of the ketene cation can be rejected, because the very distinct long vibrational progressions observed for the $\tilde{B}\ 2^2B_1$ band in both isotopic species cannot possibly broaden nor complicate the vibrational progressions of the $\tilde{A}\ 1^2B_2$ state. We attribute the complexity of this band to the possible predissociation of this band by another close-lying repulsive state or the possibility of vibrational predissociation of this band above 14.5 eV. The tail of this band extends all the way to the next observed band, the $\tilde{B}\ 2^2B_1$ state. The relatively short vibrational progressions observed in this ($\tilde{A}\ 1^2B_2$) band for both isotopic species supports the predissociation mechanism. The major vibrational progression observed is attributed to the excitations of the ν_2 and ν_4 modes. The apparent insensitivity to isotope substitution of the vibrational progressions implies that the ν_2 and ν_4 modes are predominately C=C=O stretching motions. The differences in the observed vibrational frequencies excluded the validity of the relationships: $\nu_2 \approx 2\nu_4$ and $\nu_2 \approx \nu_3 + \nu_4$ shown in the calculated vibrational frequencies by Takeshita. The doublet-like structures observed in the first few vibrational progressions indicate that at least one 'soft' mode has been excited along with the excitation of the ν_2 and ν_4 modes. The large reduction in the splittings among the doublet-like structure upon deuteration (~460.54 cm^{-1} in the $\tilde{A}\ 1^2B_2$ state of H_2CCO^+ vs. ~299.32 cm^{-1} of D_2CCO^+, calculated from the first doublet structure in this band for both isotopic species) implied that this mode might have involved the CH_2 and CD_2 group in the molecular ions. Following the convention of Duncan et al. [38,39], Allen and Schaefer [42-44] of orienting the molecule on the yz plane, this is most likely the ν_5 mode, which is characterized by the CH_2 group out of plane wagging motion, that is excited. Without supporting evidence from other

measurements, especially rotationally resolved spectroscopic studies on the cation in this state, the assignment of the ν_5 mode could only be regarded as very tentative at best. Further theoretical characterization of the potential energy surface of this state would be extremely helpful in this regard. The strong couplings among vibrational modes revealed by the high-resolution optical studies of Duncan et al. on the neutral $\tilde{X}\ ^1A_1$ ground state of ketene showed the complexity of the vibrational modes in ketene. The same or even more complex couplings among vibrational modes can be expected for the ketene cations, as shown in this study for this band.

The correlation functions calculated for this state in both isotopic species, by digitally removing the $\tilde{B}\ 2^2B_1$ state, are shown in Figure 10 and 11. The most striking feature of the correlation functions is the loss of correlation strength on a very short time scale. After only 6.2 fs in H_2CCO^+ and only 7.5 fs in D_2CCO^+ the correlation functions reached only 0.15 and 0.01, respectively. Thereafter, the correlation functions never regained their initial strengths, and there were no recognizable major oscillations. The ultra fast loss of correlation stength indicates that the initially prepared wave packet was displaced substantially from the minimum of the upper potential energy surface. The absence of the return of major oscillations strength implied that the wave packet never got back to its initial position on the upper potential energy surfaces and never regained its initial shape. Adopt the method of Remacle et al., [14] the initial and subsequent drops of the correlation functions ($[C(t)]^2$) were fitted to the exponential form of $A{\cdot}e^{-kt}$. We got k=0.95 (fs^{-1}) and 0.01 for H_2CCO^+, and k=0.70 and 0.01 for D_2CCO^+. This led to the extremely fast population decay rate on the order of 1.1 fs and 1.4 fs for the initial, 100 fs for the subsequent decaying for ketene cations. The 100 fs decaying could only be regarded as an order of magnitude, since the correlation strengths were very weak in both isotopic species after the initial decay. As discussed by Remacle et al., the initial drops in correlation functions calculated from photoelectron spectra are very sensitive to the 'wings'

in the photoelectron spectra. The experimental control of the wings was extremely difficult due to the low signal-to-noise ratio. Thus the calculated initial population-decay rate constants could only be used as indications of the order of magnitude involved. The extremely fast initial decay of the population, as manifested by the correlation function of this state on the order of a few femtosecond, implied upper potential energy surfaces very different from the neutral ground state ones according to the theoretical treatment of Ruščić. [13] The absence of any detectable emissions from this state implied that ultra-fast intramolecular processes are important in the decay of the cation from this state. This also supports the argument presented above that ketene cation in the $\tilde{A}\ 1^2B_2$ state might have been predissociated in the **Franck-Condon** region.

3. Third Band, $\tilde{B}\ 2^2B_1$ State

The third bands of ketene for both isotopic species, with fully resolved vibrational fine structures, are presented in Figure 8 and 9. The observed spectroscopic constants are summarized in Table IV. The adiabatic ionization energy was clearly established by the present study to be 14.6089(8) and 14.6106(5) eV for H_2CCO and D_2CCO. Takeshita [6] has placed the **AIE** for this band around 14.38 eV, based largely on his **FCF** calculations. Regarding the H_2CCO^+ spectrum of this band, however, if the **AIE** were lower than 14.609 eV, we would have seen another sharp peak in the spectrum near 14.50 eV that would stand out compared with contributions from the $\tilde{A}\ 1^2B_2$ state. The observed abnormality in intensity in the fifth peak of the H_2CCO^+ spectrum might be attributed to a **Fermi** resonances. In addition to the main vibrational progression, which we assigned as the ν_4 mode, there was another much weaker progression with similar spacing. The splitting between the two progressions observed is 346.7±8 cm^{-1} which, as in the $\tilde{A}\ 1^2B_2$ state, might be assigned to another 'soft' mode ν_6, that may be characterized as the

C=C=O skeleton out-of-plane bending, based largely on the insensitivity of this splitting to deuteration as discussed below.

For the D_2CCO^+ spectrum, the present high-resolution study revealed more fine structure than observed previously by both Baker et al. and Hall et al.. The additional vibrational progressions present in D_2CCO^+ beyond those present in the H_2CCO^+ spectrum seemed to be the combination of exciting the ν_4 mode together with one quantum of the ν_3 mode. This assignment was largely based on the ***ab initio*** calculation on this band by Takeshita, [6] although the calculated spectrum appeared to be very simple and has much less fine structure due to the inadequacy inherent in the calculation. The excitation of four vibrational modes in this band makes the definitive assignment of this band extremely difficult especially regarding the assignment of the excitation of ν_6, just as in the H_2COO^+ spectrum of this band. Nonetheless, the present study can be expected to spur theoretical interests to perform high level, multimode calculations to further our understanding on the structure and spectroscopy of ketene cation in the $\tilde{B}\ 2^2B_1$ state in the near future. And again, the differences in vibrational excitations and length of the progressions observed in D_2CCO^+ implied that the ionic potential energy surface in the **Franck-Condon** region and the vibronic couplings, are different for isotopic molecules, as discussed in section C of this chapter.

The correlation functions calculated for this band for both isotopic species, are shown in Figures 12 and 13. The fast initial drop in correlation strength and the deep valleys in the correlation function indicated a substantially different upper potential energy surface than the neutral ground state one for both isotopic species in the **Franck-Condon** region. The initial position of the wave packet was displaced from the equilibrium geometry, which is consistent with the observed extensive vibrational progressions. The wave packet oscillated with rather large amplitude on the upper potential energy surface, mostly along the Q_4 normal coordinate. After 35.1 fs for H_2CCO^+ (35.2 fs for D_2CCO^+)

the wave packet returned to the initial position on the ionic potential energy surfaces and a reduced maximum of C(t) 0.86 (0.79) was achieved. This corresponded very closely to one period of ν_4 vibrational motion, and the major oscillation in the correlation function for both isotopic species had a period close to the ν_4 normal mode. The ionic potential energy surface thus is strongly bound along the Q_4 normal coordinate. The slow decaying of the major oscillation of the correlation function was attributed to the spreading of the wave packet due to the anharmonicity of the potential energy surfaces and the weak excitations of other normal modes. The calculated $[C(t)]^2_{av}$ indicated a population decay rate on the order of 100 fs for both isotopic species. The multiplet-like structures in the photoelectron spectrum of D_2CCO^+ of this band, however, induced additional spreading of the wave packet, which accounted for the loss of correlation to noise level for this band after 74 fs. The stability of this state also supported the assignment of the $\tilde{A}\ 1^2B_2$ state proposed in the preceding section: that the $\tilde{A}\ 1^2B_2$ state might be predissociated. The gradually rising 'background' observed in the $\tilde{B}\ 2^2B_1$ state of the ketene cation spectrum was caused mainly by the overlapping tail of the $\tilde{A}\ 1^2B_2$ state.

4. The Fourth and Fifth Bands, $\tilde{C}\ 2^2B_2$ and $\tilde{D}\ 1^2A_1$ States

The photoelectron spectra of these two bands, as show in Figure 14 and 15, overlapped heavily, and they will be discussed together here. Observed spectroscopic constants are tabulated in Table V for the $\tilde{C}\ 2^2B_2$ state, and in Table VI for the $\tilde{D}\ 1^2A_1$ states. The $\tilde{C}\ 2^2B_2$ states of both isotopic species had well characterized vibrational progressions and are very similar in appearance. The major vibrational progression, upon deuteration, had a significant reduction in frequency and was assigned to the ν_3 mode, supporting the assignment of Hall et al..[4] Takeshita,[6] however, favored the assignment of this progression to the ν_4 mode. As discussed for the $\tilde{X}\ 1^2B_1$ state, the strong coupling and mixing among different vibrational modes in ketene made the assignment only tentative

without rotationally resolved studies. The gradually rising 'background' towards higher IEs of the $\tilde{C}\ 2^2B_2$ state were mostly attributed to the contributions by the overlapping, dissociative $\tilde{D}\ 1^2A_1$ state. The AIE of the $\tilde{D}\ 1^2A_1$ state listed in Table V thus can only be regarded as the best estimate along in the same spirit, because of the completely dissociative nature of this band in the **Franck-Condon** region. The ***ab initio*** calculation results, however, gave spacings among vibrational progressions on the order of 40 meV for the $\tilde{D}$ 1^2A_1 state with strong excitation of the ν_4 normal mode along with weak excitations of the ν_1 and ν_3 normal modes. Thus it was rather unexpected that the present high resolution study did not unveil these progressions fully. The qualitative disagreements between the calculated and the experimental spectra for the $\tilde{D}\ 1^2A_1$ state thus indicated that the potential energy surfaces of the cation in the **Franck-Condon** region must be very different from the neutral ground state and have a large anharmonicity constant in disagreement with the theoretical calculated spectrum based on harmonic potentials. Further high level calculations, and possible rotationally resolved studies by other spectroscopic means, would be very helpful in solving this difficulty.

The heavy overlapping of these two states precluded any simple means of separating them. No attempt was made to calculate the correlation functions for these two states. However, the overall FWHM of 12.5 meV for most of the peaks observed in the $\tilde{C}$ 2^2B_2 state and the shapes of the peaks indicated that the $\tilde{C}\ 2^2B_2$ state was bound in the **Fracnk-Condon** region. The rather broad and complicated band shape of the $\tilde{D}\ 1^2A_1$ state, on the other hand, indicated that the $\tilde{D}\ 1^2A_1$ state might be repulsive over part of the potential energy surface probed by photoelectron spectroscopy. The full nature of the potential energy surface for this state awaits further theoretical and experimental investigations.

5. The Sixth Band, $\tilde{E}\ 2^2A_1$ State

The photoelectron spectra of this band for both isotopic species are shown in Figures 16 and 17. The measured spectroscopic information is summarized in Table VII. Earlier experimental studies on this band had been impeded by the presence of CO_2 impurity and by the possible overlapping from the $CO_2^+\ \tilde{B}\ ^2\Sigma_u^+$ state. The present spectrum showed essentially no contamination from the $CO_2^+\ \tilde{B}\ ^2\Sigma_u^+$ state as discussed above with the $\tilde{A}\ 1^2B_2$ state of ketene and d_2-ketene. Even with the present high resolution and the effective rotational cooling, the width of the adiabatic peak for both isotopic species was much broader than the instrumental resolution and cannot be accounted for by invoking rotational broadening. The width, almost 40 meV FWHM for the adiabatic peaks, and the asymmetric shapes of the peaks, as well as the absence of any major vibrational progression, implied that other intramoleclular processes were at play.

The correlation function calculated for this state is shown in Figures 18 and 19 for H_2CCO^+ and D_2CCO^+, respectively. The ultra fast loss of correlation strength and the absence of the any major oscillation in the correlation function indicates lifetime broadening. The population decay rates calculated are τ (1/k) equal to: 3 and 4 fs for the initial drop; and 22.2 and 28.5 fs for the late decay for H_2CCO^+ and D_2CCO^+, respectively. These clearly imply that the $\tilde{E}\ 2^2A_1$ state potential energy surface is highly repulsive in the region reached by the photoionization excitation process. There are no available theoretical calculations on the potential energy surface of this state. The details of intramolecular dynamics of this state must also await further high level theoretical exploration involving multimode coupled vibronic and anharmonic effects.

F. Conclusions

A high resolution photoelectron spectroscopy study has been performed on supersonic molecular beams of H_2CCO and D_2CCO. The combination of high resolution and effective rotational cooling by supersonic expansion, as well as a least-squares fitting data reduction procedure, have enabled spectroscopic constants of much improved accuracy to be determined for the $\tilde{X}\ 1^2B_1$, $\tilde{A}\ 1^2B_2$, $\tilde{B}\ 2^2B_1$, $\tilde{C}\ 2^2B_2$, and $\tilde{E}\ 2^2A_1$ states. The complex nature and the strong overlap with other bands left the $\tilde{D}\ 1^2A_1$ state much less well characterized. Most of the spectroscopic constants of the ionic states are obtained here for the first time. This should prompt further theoretical calculations to be performed on a high level. The discrepancies in the observed and calculated spectra in the first and second excited states for the ketene cations pointed out the need to improve the theoretical sophistication to match the currently available experimental results. The present studies on such a complex system as ketene represents a major challenge to the present level of theoretical sophistication to tackle the structure, spectroscopy and dynamics of polyatomic molecules and ions. The first excited state in this regard will be particularly interesting to follow the points implied from the present study are studied thoroughly in the near future by theoretical calculations. Multimode coupled vibronic calculations on the spectra, together with multidimensional calculations on the ionic potential energy surfaces, would be extremely important to push forward our understanding on the spectroscopy, structure, and dynamics of polyatomic ions.

Vibrational autocorrelation functions were calculated from the photoelectron bands for all but two electronic states of the ketene cations. The ground $\tilde{X}\ 1^2B_1$ state correlation functions displayed oscillatory patterns, which were characteristic of the virtually undisplaced wave packets composed mainly of two oscillators. The wave packets oscillated with small amplitude around the initial position on the ionic potential energy surface with little spreading, indicated a fairly stable state in the **Franck-Condon** region.

In the calculated $\tilde{A}\ 1^2B_2$ state correlation functions, an ultra fast decay of the wave packets were observed. This effect was attributed largely to the possible predissociating nature of this state near the initially populated potential energy surface, which fervently awaits further theoretical characterization. The correlation functions of the $\tilde{E}\ 2^2A_1$ state showed ultra fast decay of the initial prepared wave packet on the ionic potential energy surface on a time scale of a few femtoseconds. This implied that dissociation and ultra fast intramolecular dynamic processes were among the important decay pathways for the initially prepared wave packet around the **Franck-Condon** region on the ionic potential energy surface for this state.

References:

1. A. D. Baker, and D. W. Turner, **Chem. Comm.**, 480(1969).
2. D. W. Turner, Phil. Trans. R. Soc., London Ser., A7, 268(1970).
3. D. W. Turner, A. D. Baker, and C. R. Brundle, Molecular Photoelectron Spectroscopy, John Wiley & Sons, London (1970) p139.
4. D. Hall, J. P. Maier, and P. Rosmus, Chem. Phys., 373, 24(1977).
5. D. P. Chong, Theoretical Chim. Acta., 181, 50(1978).
6. K. Takeshita, J. Chem. Phys., 96(2), 1199(1992).
7. E. J. Heller, *ibid*, 68, 2066(1978).
8. E. J. Heller, E. B. Stechel, and M. J. Davis, *ibid*, 73(10), 4720(1980).
9. E. J. Heller, Acc. Chem. Res., 14, 368(1981).
10. E. J. Helller, R. Sundberg, and D. Tanner, J. Chem. Phys., 76, 1822(1982).
11. B. Layh-Nihaut, and J. C. Lorquet, *ibid*, 88(9), 5606(1988).
12. A. J. Lorquet, J. C. Lorquet, J. Delwiche, and M. J. Hubin-Franskin, *ibid*, 76(10), 4692(1982).
13. B. Ruščić *ibid*, 85(7), 3776(1986).
14. F. Remacle, M. Desoute-Leconmte, and J. C. Lorquet, *ibid*, 91(7), 4155(1989).
15. J. E Pollard, D. J. Trevor, J. E Reutt, Y. T. Lee, and D. A. Shirley, J. Chem. Phys., 81(2), 5302(1984).
16. J. E. Reutt, L. S. Wang, J. E. Pollard, D. J. Trevor, Y. T. Lee, and D. A. Shirley, *ibid*, 84(6), 3022(1986).
17. J. E. Reutt, L. S. Wang, Y. T. Lee, and D. A. Shirley, *ibid*, 85(12), 6928(1986).
18. J. E. Pollard, D. J. Trevor, Y. T. Lee, and D. A. Shirley, Rev. Sci. Instrum., 52, 1837(1981).
19. J. E. Pollard, Ph.D. Thesis, Department of Chemistry, The University of California at Berkeley, 1982.

20. J. E. Reutt, Ph.D. Thesis, Department of Chemistry, The University of California at Berkeley, 1986.

21. Williams and Hurd, J. Org. Chem., **5**, 122(1940).

22. G. J. Fisher, A. F. Maclean, and A. W. Schwizer, J. Org. Chem., 1055(1952).

23. B. I. Sonobe, and R. N. Rosenfeld, JACS., **105**, 7528(1983).

24. H. Bitto, D. R. Guyer, W. F. Polik, and C. B. Moore, Faraday Trans. Dis. Chem. Soc., **81**, 149(1986).

25. I-Chia Chen, W. H. Green, Jr., and C. B. Moore, J. Chem. Phys., **89(1)**, 314(1988).

26. I-Chia Chen, and C. B. Moore, J. Phys. Chem., **94**, 263,269(1990)

27. A. Lufthus, and P. H. Krupenie, J. Phys. Chem. Ref. Data, **6**, 113(1977).

28. C. E. Moore, ed., Atomic Energy Levels, **Vol. I**, (National Bureau of Standards, Washington D. C., 1958).

29. M. Born, and J. R. Oppenheimer, Ann. Phyz. (Lepzig), **84**, 457-487(1927).

30. J. W. Rabalais, **Principles of Ultraviolet Photoelectron Spectroscopy**, John Wiley & Sons, NY (1979).

31. H. Köppel, W. Domcke, and L. S. Cederbaum, Adv. Chem. Phys., **Vol. LVII**, p59-246(1984).

32. L. S. Cederbaum, and W. Domcke, J. Chem. Phys., 64(2), 603(1976).

33. W. Domcke, and L. S. Cederbaum,*ibid*, 64(2), 612(1976).

34. S. B. O'Neil, and W. P. Reinhardt, *ibid*, 69, 2126(1978).

35. E. Oran. Brighan, **The Fast Fourier Transform**, (Prentice-Hall, Englewood Cliffs), p164(1974).

36. J. I. Steinfeld, **An Introduction to Modern Molecular Spectroscopy**, 2nd. ed., The MIT Press, Cambridge, MA, p133(1985).

37. G. Herzberg, Molecular Spectra and Molecular Structures, I. Spectra of Diatomic Molecules, Van Norstrand Reinhold Com., NY, P93(1950).

38. J. L. Duncan, A. M. Ferguson, J. Harpper, and K. H. Tonge, J. Mol. Spectr., 125, 196-213(1987)

39. J. L. Duncan, A. M. Ferguson, J. Harpper, and K. H. Tonge, *ibid*, 122, 72-93(1987).

40. C. B. Moore, and G. Pimentel, J. Chem. Phys., 38(12), 2816(1963).

41. L. S. Wang, J. E. Reutt, Y. T. Lee, and D. A. Shirley, J. Elect. Spectr. and Related Phenomena, 47, 167-186(1988).

42. W. D. Allen, and H. F. Schaeffer III, J. Chem. Phys., 84, 2212(1986).

43. W. D. Allen, and H. F. Schaeffer III, *ibid*, 87, 7076(1987).

44. W. D. Allen, and H. F. Schaeffer III, *ibid*,, 89, 2329(1988).

45. R. A. Marcus, Science, Vol. 256, p1523, 12 June1992.

46. E. R. Lovejoy, S. K. Kim, and C. B. Moore, ibid, Vol. 256, p1541(1992).

Table I. Ionization Potentials & Vibrational Frequencies (cm^{-1}) Observed

Ionic States	AIE[a] (eV)	ν_1	ν_2	ν_3	ν_4	ν_5	ν_6
H_2CCO^b $\tilde{X}\,^1A_1$		3070.4	2152.6	1387.5	1116.0	587.4	528.4
H_2CCO^+ $\tilde{X}\,1^2B_2$	9.6191(4)		2263.4 (4.3)	1378.6 (4.3)	1226.9 (4.3)		
$\tilde{A}\,1^2B_2$	13.7967(3)		1527.9 (4.3)		1164.2 (4.3)	460.7 (4.3)	
$\tilde{B}\,2^2B_1$	14.6089(8)		2001.2 (4.3)		1000.8 (4.3)		346.7 (4.3)
$\tilde{C}\,2^2B_2$	16.0687(8)		1697.1 (4.3)	1086.6 (4.3)			
$\tilde{D}\,1^2A_1$	16.2393(3)[c]		1488.0 (4.3)	1164.3 (4.3)	708.9 (4.3)		
$\tilde{E}\,2^2A_1$	18.0897(10)			1177.4 (4.3)	670.6 (4.3)		396.9 (4.3)

(a) The absolute AIEs are accurate to ± 3 meV as discussed in the main text. Other spectroscopic constants, however, were obtained as line splittings, and can thus be reported to a much higher accuracy, ±0.5 meV (±4.3 cm^{-1}). (b) From ref. 38-40. (c) Best estimate only. (d) From the splitting in the first two peaks of the $\tilde{A}\,1^2B_2$ state. Numbers in parenthese indicate the uncertainties in the last digit.

TABLE I. Continued

Ionic States	AIE[a] (eV)	ν_1	ν_2	ν_3	ν_4	ν_5	ν_6
D_2CCO^b $\tilde{X}\,^1A_1$		2267.3	2120.5	1225.1	924.7	541.2	434.7
D_2CCO^+ $\tilde{X}\,1^2B_2$	9.6130(3)		2285.6 (4.3)	1090.9 (4.3)	924.7 (4.3)		
$\tilde{A}\,1^2B_2$	13.8366(8)		2140.4 (4.3)		1006.6 (4.3)	299.3 (4.3)	105.8 (4.3)
$\tilde{B}\,2^2B_1$	14.4942(7)		1732.3 (4.3)	848.4 (4.3)	1056.1 (4.3)		
$\tilde{C}\,2^2B_2$	16.0856(1)		1101.7 (4.3)	799.8 (4.3)			
$\tilde{D}\,1^2A_1$	16.3204(2)[c]	1266.7 (4.3)	1204.0 (4.3)	1168.8 (4.3)			
$\tilde{E}\,2^2A_1$	18.0734(10)	1133.3 (4.3)	834.4 (4.3)				

(a) The absolute AIEs are accurate to ± 3meV as discussed in the main text. Other spectroscopic constants, however, are obtained as line splittings, and can thus be reported to a much higher accuracy, ±0.5 meV (±4.3 cm^{-1}). (b) From ref. 38-40. (c) Best estimate only. (d) From the splitting in the first two peaks of the $\tilde{A}\,1^2B_2$ state. Numbers in parenthese indicate the uncertanties in the last digit.

TABLE II. Vibrational Levels of the $\tilde{X}\ 1^2B_1$ State

IE[a] H_2CCO^+ (eV)	Vibrational Progressions ($\nu_2\nu_3\nu_4$)		
9.6191(4)	000	000	000
9.8954(5)	100		
10.1674(5)	200		
10.4351(3)	300		
9.7465(1)			001
10.0206(6)			101
10.2948(1)			201
10.5646(5)			301
9.7900(7)		010	
10.0672(5)		110	
10.3135(4)		120	
9.84913(2)			002
10.1277(3)			102
10.3959(9)			202

$\omega_0\ (\nu_2)$ = 2263.4 (4.3) cm^{-1}	$\omega_0 x_0$ = 17.4 (4.3) cm^{-1}
$\omega_0\ (\nu_3)$ = 1378.6 (4.3) cm^{-1}	$\omega_0 x_0$ = ?
$\omega_0\ (\nu_4)$ = 1226.9 (4.3) cm^{-1}	$\omega_0 x_0$ = 99.8 (4.3) cm^{-1}

IE[a] D_2CCO^+	Vibrational Progressions ($\nu_2\nu_3\nu_4$)		
9.6130(3)	000	000	000
9.8902(9)	100		
10.1628(6)	200		
10.4336(4)	300		
10.6937(2)	400		

TABLE II. Continued

9.7478(4)	010	
10.0239(2)	110	
10.3050(5)	210	
10.5634(6)	310	
10.8309(7)	410	
9.7272(4)		001
10.0030(3)		101
10.2801(5)		201
10.5439(2)		301
10.8063(6)		401
9.8848(1)	020	
10.1592(4)	120	
10.4295(7)	220	
10.6793(4)	320	
9.8622(8)		002
10.1408(2)		102
10.4152(5)		202
10.6835(7)		302

ω_0 (ν_2) = **2285.6 (4.3) cm^{-1}**	$\omega_0 x_0$ = **20.8 (4.3) cm^{-1}**
ω_0 (ν_3) = **1090.9 (4.3) cm^{-1}**	$\omega_0 x_0$ = **-6.9 (4.3) cm^{-1}**
ω_0 (ν_4) = **924.7 (4.3) cm^{-1}**	$\omega_0 x_0$ = **-82.2 (4.3) cm^{-1}**

a. See footnote in TABLE I.

TABLE III. Vibrational Levels of the $\tilde{A}\ 1^2B_2$ State

IE[a] H_2CCO^+ (eV)	Vibrational Progressions ($\nu_2\nu_4\nu_5$)		
13.7967(3)	000	000	000
13.9829(2)	100		
14.1925(4)	200		
14.4093(4)	300		
13.9349(5)		010	
14.0694(2)		020	
14.1988(3)		030	
14.3213(4)		040	
13.8538(5)			001
14.0700(3)			101
14.2805(5)			201
14.4846(9)			301
13.8822(5)	$000(6_0^1)$		
14.0137(2)	$010(6_0^1)$		
14.1347(7)	$020(6_0^1)$		
14.2627(7)	$030(6_0^1)$		

$\omega_0(\nu_2)$ = **1527.9 (4.3) cm^{-1}**	ω_0x_0 = **-61.7 (4.3) cm^{-1}**
$\omega_0(\nu_4)$ = **1164.2 (4.3) cm^{-1}**	ω_0x_0 = **21.1 (4.3) cm^{-1}**
$\omega_0(\nu_5)$ = **460.7 (4.3) cm^{-1}**	ω_0x_0 = **?**
$\omega_0(\nu_6)$ = **689.8 (4.3) cm^{-1}**	ω_0x_0 = **?**

IE[a] D_2CCO^+ (eV)	Vibrational Progressions ($\nu_2\nu_4\nu_5$)		
13.8366(8)	000	000	000
13.9653(2)		010	

TABLE III. Continued

14.0939(7)		020	
14.2337(4)		030	
14.3648(9)		040	
14.5092(8)		050	
13.8737(9)			001
14.1385(2)			101
14.4019(7)			201
13.9331(6)		$000(6_0^1)$	
14.0605(7)		$010(6_0^1)$	
14.1879(7)		$020(6_0^1)$	
14.3188(3)		$030(6_0^1)$	
14.0049(1)	$001(6_0^1)$		
14.2337(4)	$101(6_0^1)$		
14.4625(8)	$201(6_0^1)$		

$\omega_0(\nu_2)$ = **2140.4 (4.3) cm^{-1}**	$\omega_0 x_0$ = **5.2 (4.3) cm^{-1}**
$\omega_0(\nu_4)$ = **1006.7 (4.3) cm^{-1}**	$\omega_0 x_0$ = **-12.8 (4.3) cm^{-1}**
$\omega_0(\nu_5)$ = **299.3 (4.3) cm^{-1}**	$\omega_0 x_0$ = **?**
$\omega_0(\nu_6)$ = **105.8 (4.3) cm^{-1}**	$\omega_0 x_0$ = **?**

a. See footnote in TABLE I.

TABLE IV. Vibrational Levels of the $\tilde{B}\ 2^2B_1$ State

IE[a] H_2CCO^+(eV)	Vibrational Progressions ($\nu_2\nu_4\nu_6$)		
14.6089(8)	000	000	000
14.7320(6)		010	
14.8531(9)	(100)[b]	020	
14.9743(2)		030	
15.0934(9)	(200)[b]	040	
15.2107(1)		050	
15.3259(8)		060	
15.44191(1)		070	
15.5662(9)		080	
15.6721(4)		090	
15.7820(9)		0(10)0	
14.6519(6)			001
14.7672(3)			011
14.8942(2)			021
15.0114(4)			031
15.1403(8)			041
15.2572(8)			051
15.3670(1)			061
15.4805(1)			071
15.5897(3)			081
15.7004(1)			091
15.8072(2)			0(10)1

TABLE IV. Continued

IE[a] D_2CCO^+(eV)	Vibrational Progressions ($\nu_2\nu_3\nu_4$)		
14.6106(5)	000	000	000
14.7404(6)			001
14.8725(1)			002
15.0023(2)			003
15.1327(7)			004
14.7158(4)		010	
14.8478(9)		011	
14.9732(3)		012	
15.1052(8)		013	
15.2328(5)		014	
15.3787(2)		015	
15.5169(7)		016	
14.8255(1)	100		
14.9530(8)	101		
15.0784(2)	102		
15.2059(9)	103		
15.3358(0)	104		
15.4708(9)	105		
15.0653(6)			110
15.1836(1)			111
15.3089(5)			112
15.4298(0)			113
15.5444(0)			114

TABLE IV. Continued

15.6625(7)	115
15.7767(1)	116
15.8841(4)	117

H_2CCO^+ $\tilde{B}$ 2^2B_1 State Summary:

$\omega_0(\nu_2)$ = 2001.2 (4.3) cm^{-1}	ω_0x_0 = 15.8 (4.3) cm^{-1}
$\omega_0(\nu_4)$ = 1000.8 (4.3) cm^{-1}	ω_0x_0 = 4.8 (4.3) cm^{-1}
$\omega_0(\nu_6)$ = 346.7 (4.3) cm^{-1}	ω_0x_0 = ?

D_2CCO^+ $\tilde{B}$ 2^2B_1 State Summary:

$\omega_0(\nu_2)$ = 1732.3 (4.3) cm^{-1}	ω_0x_0 = ?
$\omega_0(\nu_3)$ = 848.4 (4.3) cm^{-1}	ω_0x_0 = ?
$\omega_0(\nu_4)$ = 1056.1 (4.3) cm^{-1}	ω_0x_0 = 0.5 (4.3) cm^{-1}

(a) See footnote in TABLE I. (b) **Fermi** resonances peaks.

TABLE V. Vibrational Levels of the $\tilde{C}\ 2^2B_2$ State

IE[a] H_2CCO^+(eV)	Vibrational Progressions ($\nu_2\nu_3$)		
16.0687(8)	00	00	00
16.1981(6)		01	
16.3257(5)		02	
16.4567(8)		03	
16.5862(2)		04	
16.7155(5)		05	
16.8365(8)		06	
16.9512(9)		07	
17.0746(8)		08	
16.06878)	00		
16.2790(2)	10		
16.4915(5)	20		
16.7021(8)	30		
16.9121(4)	40		
17.1280(4)	50		
17.3381(9)	60		
16.1721(2)			01
16.3625(6)			11
16.5557(4)			21
16.7443(1)			31
16.9376(7)			41

$\omega_0(\nu_2)$ = 1697.1 (4.3) cm^{-1}	ω_0x_0 = -1.4 (4.3) cm^{-1}
$\omega_0(\nu_3)$ = 1086.6 (4.3) cm^{-1}	ω_0x_0 = 7.8 (4.3) cm^{-1}

Table V. Continued

IE[a] D_2CCO^+(eV)	Vibrational Progressions ($\nu_2\nu_3$)		
16.0856(1)	00	00	00
16.1889(6)	01		
16.2841(8)	02		
16.3828(3)	03		
16.4761(6)	04		
16.5746(9)	05		
16.6744(1)	06		
16.7666(4)	07		
16.2222(0)			10
16.3271(8)			11
16.4326(9)			12
16.5323(1)			13
16.6320(3)			14

$\omega_0(\nu_2)$ = **1101.7 (4.3) cm^{-1}**	$\omega_0 x_0$ = **?**
$\omega_0(\nu_3)$ = **799.8 (4.3) cm^{-1}**	$\omega_0 x_0$ = **2.1 (4.3) cm^{-1}**

a. See footnote in TABLE I.

TABLE VI. Vibrational Levels of the $\tilde{D}\ 1^2A_1$ State

IE[a] H_2CCO^+(eV)	Vibrational Progressions ($\nu_2\nu_3\nu_4$)		
16.2393(3)		000	
16.4438(5)	100		
16.6267(3)	200		
16.8235(4)	300		
17.0279(0)	400		
17.2422(6)	500		
16.4281(1)			100
16.5067(7)			101
16.5913(4)			102
16.6798(3)			103
16.7624(2)			104
16.8450(2)			105
16.9295(8)			106
17.0121(8)			107
17.0869(0)			108
17.1596(6)			109
16.5008(8)		101	
16.6346(0)		111	
16.7781(5)		121	
16.9118(8)		131	
17.0495(4)		141	
17.1793(3)		151	
17.3012(5)		161	

TABLE VI. Continued

IE[a] D_2CCO^+(eV)	Vibrational Progressions ($\nu_1\nu_2\nu_3$)		
16.3204(2)	000	000	000
16.4625(1)	001		
16.5971(3)	002		
16.7367(3)	003		
16.8663(6)	004		
16.9934(9)	005		
16.4774(7)			100
16.6295(4)			110
16.7766(1)			120
16.9162(1)			130
17.0508(3)			140
17.1954(1)			150
17.3399(9)			160
17.4671(3)			170

H_2CCO^+ $\tilde{D}$ 1^2A_1 State Summary:

$\omega_0(\nu_2)$ = 1488.0 (4.3) cm^{-1}	ω_0x_0 = -19.5 (4.3) cm^{-1}
$\omega_0(\nu_3)$ = 1164.3 (4.3) cm^{-1}	ω_0x_0 = 11.5 (4.3) cm^{-1}
$\omega_0(\nu_4)$ = 708.9 (4.3) cm^{-1}	ω_0x_0 = 4.5 (4.3) cm^{-1}

D_2CCO^+ $\tilde{D}$ 1^2A_1 State Summary:

$\omega_0(\nu_1)$ = 1266.7 (4.3) cm^{-1}	ω_0x_0 = ?
$\omega_0(\nu_2)$ = 1204.9 (4.3) cm^{-1}	ω_0x_0 = 8.2 (4.3) cm^{-1}
$\omega_0(\nu_3)$ = 1168.8 (4.3) cm^{-1}	ω_0x_0 = 13.6 (4.3) cm^{-1}

a. See footnote in TABLE I.

TABLE VII. Vibrational Levels of the $\tilde{E}\ 2^2A_1$ State

IE[a] H_2CCO^+(eV)	Vibrational Progressions ($\nu_3\nu_4\nu_6$)		
18.0897(3)[b]	000	000	000
18.2333(5)	100		
18.3697(4)	200		
18.5061(5)	300		
18.6367(5)	400		
18.1739(5)		010	
18.2593(5)		020	
18.3492(2)		030	
18.4281(7)		040	
18.5234(8)		050	
18.1428(2)			001
18.2069(9)			002
18.2719(5)			003
18.1739(5)	010		
18.3158(6)	110		
18.4465(1)	210		
18.5920(5)	310		

$\omega_0(\nu_3)$ = 1177.4 (4.3) cm^{-1}	ω_0x_0 = 15.0 (4.3) cm^{-1}
$\omega_0(\nu_4)$ = 670.6 (4.3) cm^{-1}	ω_0x_0 = -4.3 (4.3) cm^{-1}
$\omega_0(\nu_6)^c$ = 396.9 (4.3) cm^{-1}	$(\omega_0x_0)^c$ = -23.9 (4.3) cm^{-1}

TABLE VII. Continued

IE[a] D_2CO^+ (eV)	Vibrational Levels ($\nu_1\nu_2$)	
18.0734(5)[b]	00	00
18.2101(4)	10	
18.3456(1)	20	
18.4761(5)	30	
18.1768(9)		01
18.3197(5)		11
18.4564(5)		21
$\omega_0(\nu_1)$ = 1133.3 (4.3) cm^{-1}	$\omega_0 x_0$ = 12.4 (4.3) cm^{-1}	
$\omega_0(\nu_2)$ = 834.3 (4.3) cm^{-1}	$\omega_0 x_0$ = ?	

(a) See Table I. footnote. (b) This is only the best estimate ± 10 meV. (c) Tentative values.

Figure Captions:

Figure 1. The full spectrum of ketene with a resolution of 11.5 meV FWHM, the result of five sequential scans each lasting about two hours. Each scan was repeated four times to enhance statistics. The designation of the ionic states assumes that the ions have C_{2V} symmetry.

Figure 2. The full spectrum of d_2-ketene with a resolution of 11.5 meV FWHM, the result of five sequential scans each lasting about two hours. Each scan was repeated four times to enhance statistics. The designation of the ionic states assumes that the ions have C_{2V} symmetry.

Figure 3. The photoelectron spectrum of the $\tilde{X}\ 1^2B_1$ state of ketene, with a resolution of 11.5 meV FWHM. The vibrational progressions are labeled according to the C_{2V} geometry and 2_0^n stands for the transition of

$$M^+ (\nu_2 = n) + e \leftarrow M (\nu_2 = 0) + \hbar\omega$$

following standard spectroscopic notations.

Figure 4. The photoelectron spectrum of the $\tilde{X}\ 1^2B_1$ state of d_2-ketene, with a resolution of 11.5 meV FWHM. The vibrational progressions are labeled according to the C_{2V} geometry, and notations are the same as in the $\tilde{X}$ 1^2B_1 state of ketene.

Figure 5. The vibrational autocorrelation function of the $\tilde{X}\ 1^2B_1$ state of ketene after all corrections were made. The beat pattern results from the phase relationship of a stable two-mode anharmonic oscillator system, with $\nu_2 \geq 2\nu_3, 2\nu_4$. The shallow minima in the correlation function are characteristics of the wave packet prepared through a predominately

adiabatic transition. An essentially non-bonding electron is ejected, and the initially prepared wave packet is localized around the minimum of the upper potential energy surface. It weakly oscillates around this region, retaining a high level of correlation at all time.

Figure 6. The vibrational autocorrelation function of the $\tilde{X}\ 1^2B_1$ state of d_2-ketene after all corrections were made. Essentially the same behavior is observed as in the $\tilde{X}\ 1^2B_1$ state of ketene.

Figure 7. The vibrational autocorrelation functions of the $\tilde{X}\ 1^2B_1$ states of ketene and d_2-ketene. The solid line is ketene and the dotted line is d_2-ketene. Note the isotope effect at longer times.

Figure 8. The photoelectron spectrum of the $\tilde{A}\ 1^2B_2$ and $\tilde{B}\ 2^2B_1$ states of ketene with a resolution of 11.5 meV FWHM. Note the fine vibrational progressions in the $\tilde{A}\ 1^2B_2$ state were resolved here for the first time. The doublet-like structure in the $\tilde{A}\ 1^2B_2$ was due to the excitation of a 'soft' mode, here designated as ν_5. Also, the weaker progression in the $\tilde{B}\ 2^2B_1$ state was due to the excitation of a 'soft' mode, here designated as ν_6, together with the main excitation of ν_4 mode.

Figure 9. The photoelectron spectrum of the $\tilde{A}\ 1^2B_2$ and $\tilde{B}\ 2^2B_1$ states of d_2-ketene with a resolution of 11.5 meV FWHM. Comparing with the spectrum of ketene, a strong isotope effect on the vibrational fine structures is observed.

Figure 10. The vibrational correlation function calculated for the $\tilde{A}\ 1^2B_2$ state of ketene after digitally removing the contributions from the $\tilde{B}\ 2^2B_1$ state, and making all corrections. The most striking feature of the correlation function is the

loss of correlation strength on an ultra fast time scale of a few fs. This implies that ketene cations were prepared on the repulsive side of the upper potential energy surface, and were subject to predissociation and other ultra fast intramolecular dynamic processes.

Figure 11. The vibrational correlation function calculated for the $\tilde{A}\ 1^2B_2$ state of d_2-ketene after digitally removing the contributions from the $\tilde{B}\ 2^2B_1$ state, and making all corrections.

Figure 12. The vibrational correlation function calculated for the $\tilde{B}\ 2^2B_1$ state of ketene after digitally removing the contributions from the $\tilde{A}\ 1^2B_2$ state, and making all corrections. The deep valleys in the correlation function indicate a displaced wave packet from the upper potential energy surface (**PES**) minimum.

Figure 13. The vibrational correlation function calculated for the $\tilde{B}\ 2^2B_1$ state of d_2-ketene after digitally removing the contributions from the $\tilde{A}\ 1^2B_2$ state, and making all corrections. The loss of correlation strength beyond 74 fs was attributed to the spreading of the wave packet due to anharmonicity and the excitation of additional vibrational modes.

Figure 14. The photoelectron spectrum of the $\tilde{C}\ 2^2B_2$ and $\tilde{D}\ 1^2A_1$ states of ketene, with a resolution of 11.5 meV FWHM. The major vibrational progression was attributed to the $\tilde{C}\ 2^2B_2$ state.

Figure 15. The photoelectron spectrum of the $\tilde{C}\ 2^2B_2$ and $\tilde{D}\ 1^2A_1$ states of d_2-ketene with a resolution of 11.5 meV FWHM. The major vibrational progression was attributed to the $\tilde{C}\ 2^2B_2$ state.

Figure 16. The photoelectron spectrum of the $\tilde{E}\ 2^2A_1$ state of ketene with a resolution of 11.5 meV FWHM. The very broad adiabatic peak and the asymmetric line shape imply that ketene cations in the **Franck-Condon** part of the **PES** are subject to lifetime broadening effects.

Figure 17. The photoelectron spectrum of the $\tilde{E}\ 2^2A_1$ state of d_2-ketene with a resolution of 11.5 meV FWHM. The very broad adiabatic peak and the asymmetric line shape imply that this state in the **Franck-Condon** region is subject to lifetime broadening.

Figure 18. The vibrational correlation function calculated for the $\tilde{E}\ 2^2A_1$ state of ketene after all corrections were made. The ultra fast decay of the correlation function implies that ultra fast intramolecular processes dominate the decay of the ketene cations in the **Franck-Condon** part of the **PES**.

Figure 19. The vibrational correlation function calculated for the $\tilde{E}\ 2^2A_1$ state of d_2-ketene after all corrections were made. The ultra fast decay of the correlation function implies that ultra fast intramolecular processes dominate the decay of the ketene cations in the **Franck-Condon** part of the **PES**.

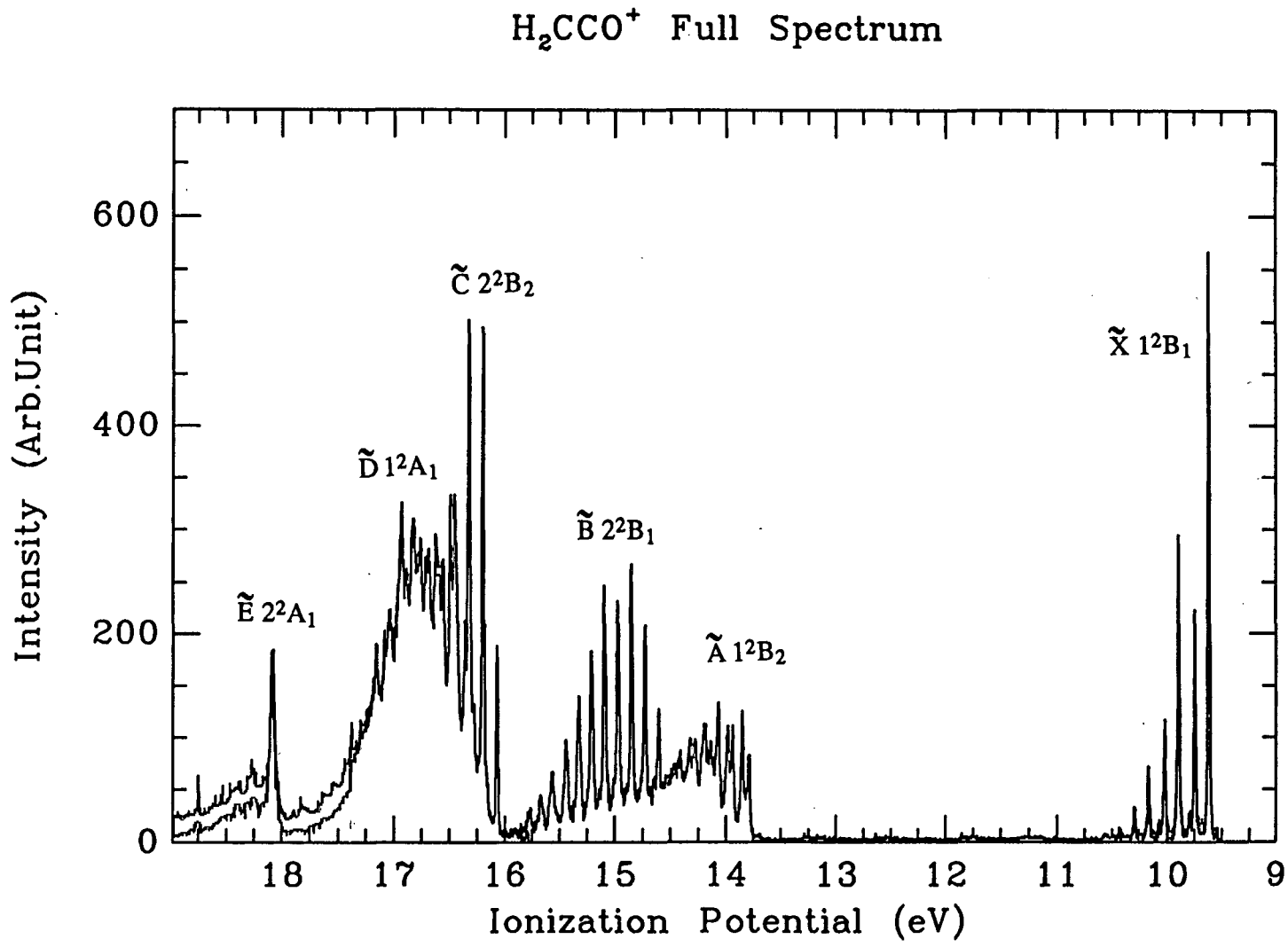
H_2CCO^+ Full Spectrum
Intensity (Arb.Unit)
600
400
200
0
$\tilde{E}\ 2^2A_1$
$\tilde{D}\ 1^2A_1$
$\tilde{C}\ 2^2B_2$
$\tilde{B}\ 2^2B_1$
$\tilde{A}\ 1^2B_2$
$\tilde{X}\ 1^2B_1$
18
17
16
15
14
13
12
11
10
9
Ionization Potential (eV)

Figure 1

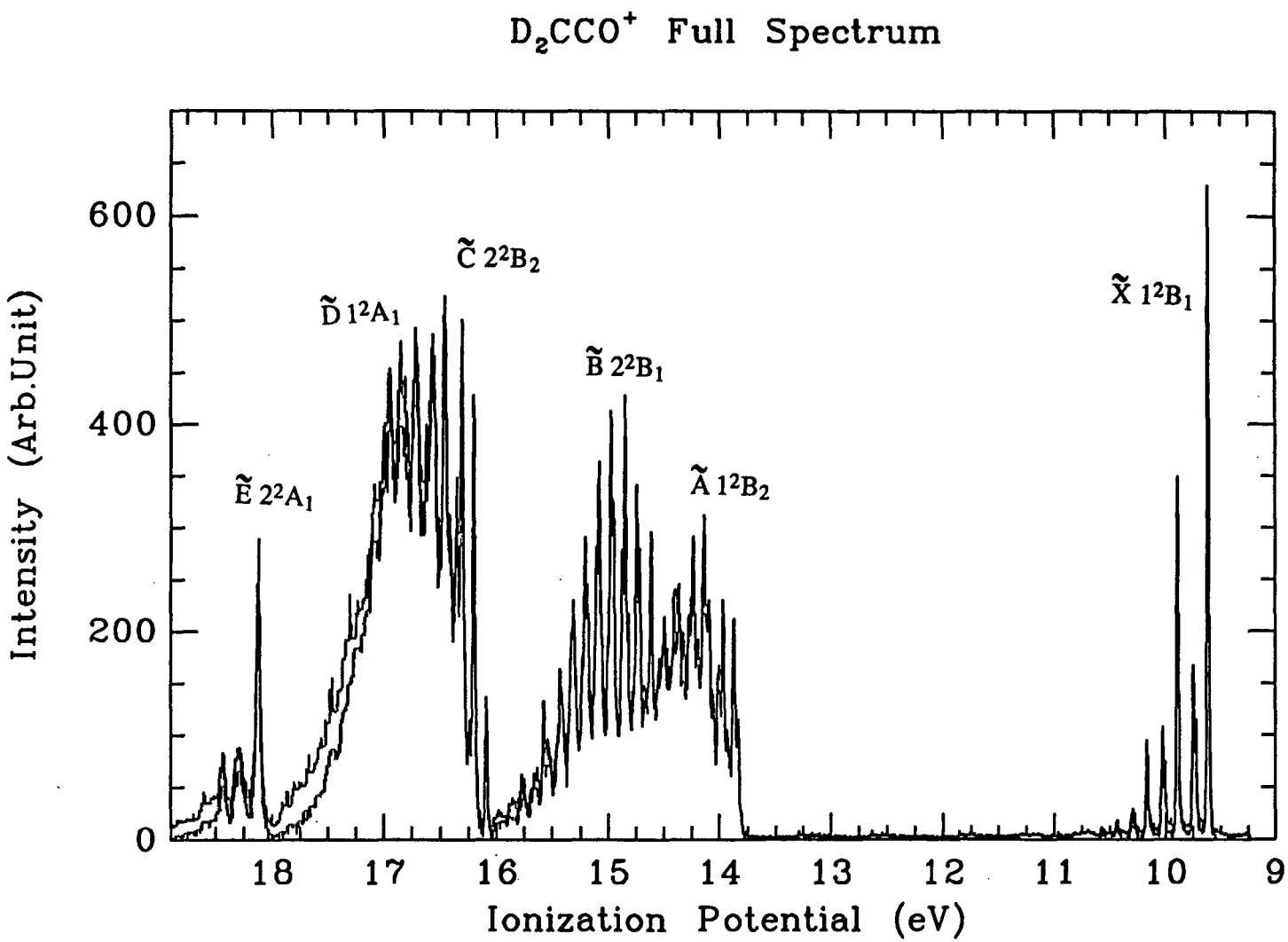
D2CCO+ Full Spectrum
Intensity (Arb.Unit)
600
400
200
0
Ẽ 2²A1
D̃ 1²A1
C̃ 2²B2
B̃ 2²B1
Ã 1²B2
X̃ 1²B1
18
17
16
15
14
13
12
11
10
9
Ionization Potential (eV)

Figure 2

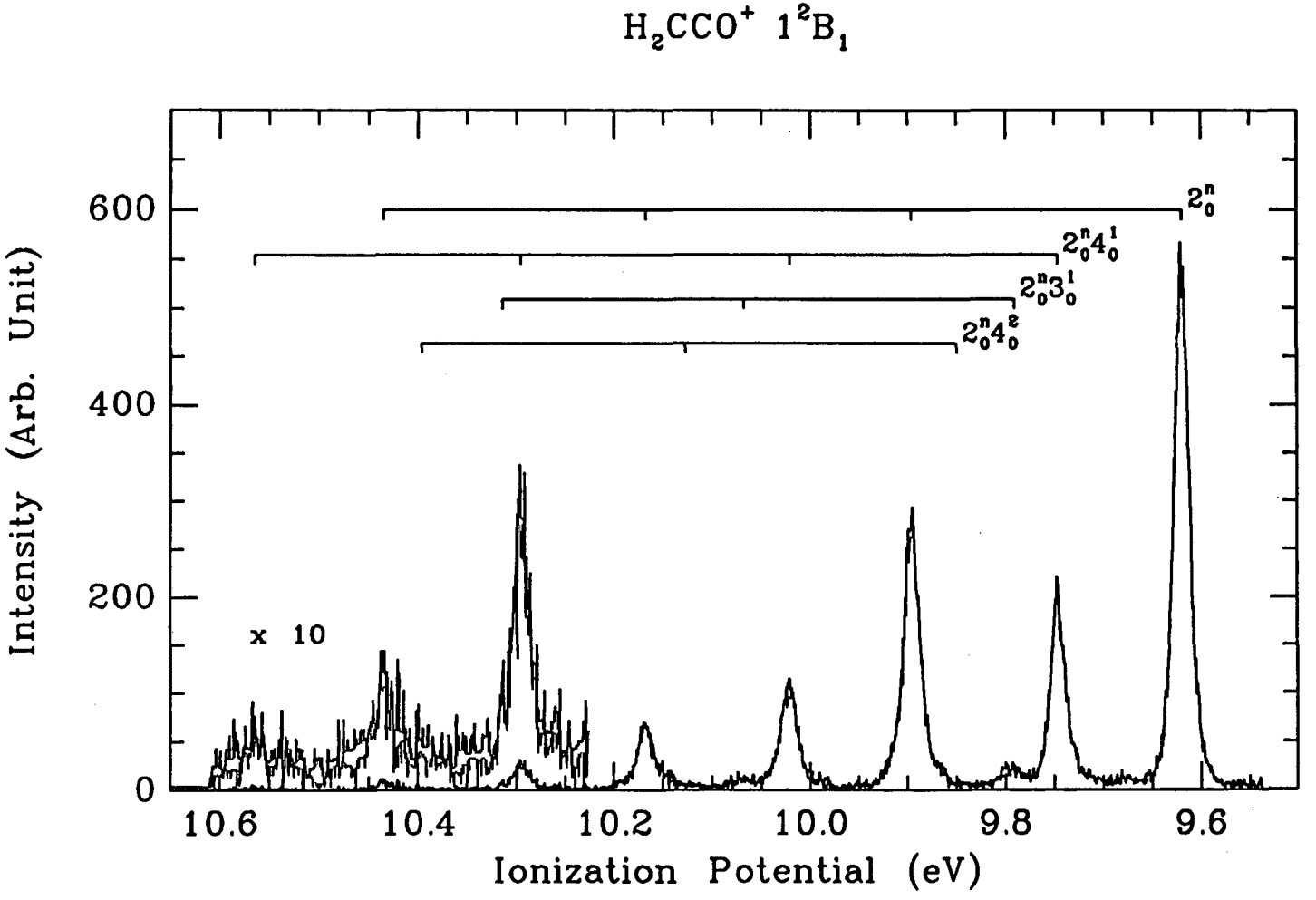
H_2CCO^+ 1^2B_1
Intensity (Arb. Unit)
600
400
200
0
x 10
2_0^n
$2_0^n4_0^1$
$2_0^n3_0^1$
$2_0^n4_0^2$
10.6
10.4
10.2
10.0
9.8
9.6
Ionization Potential (eV)

Figure 3

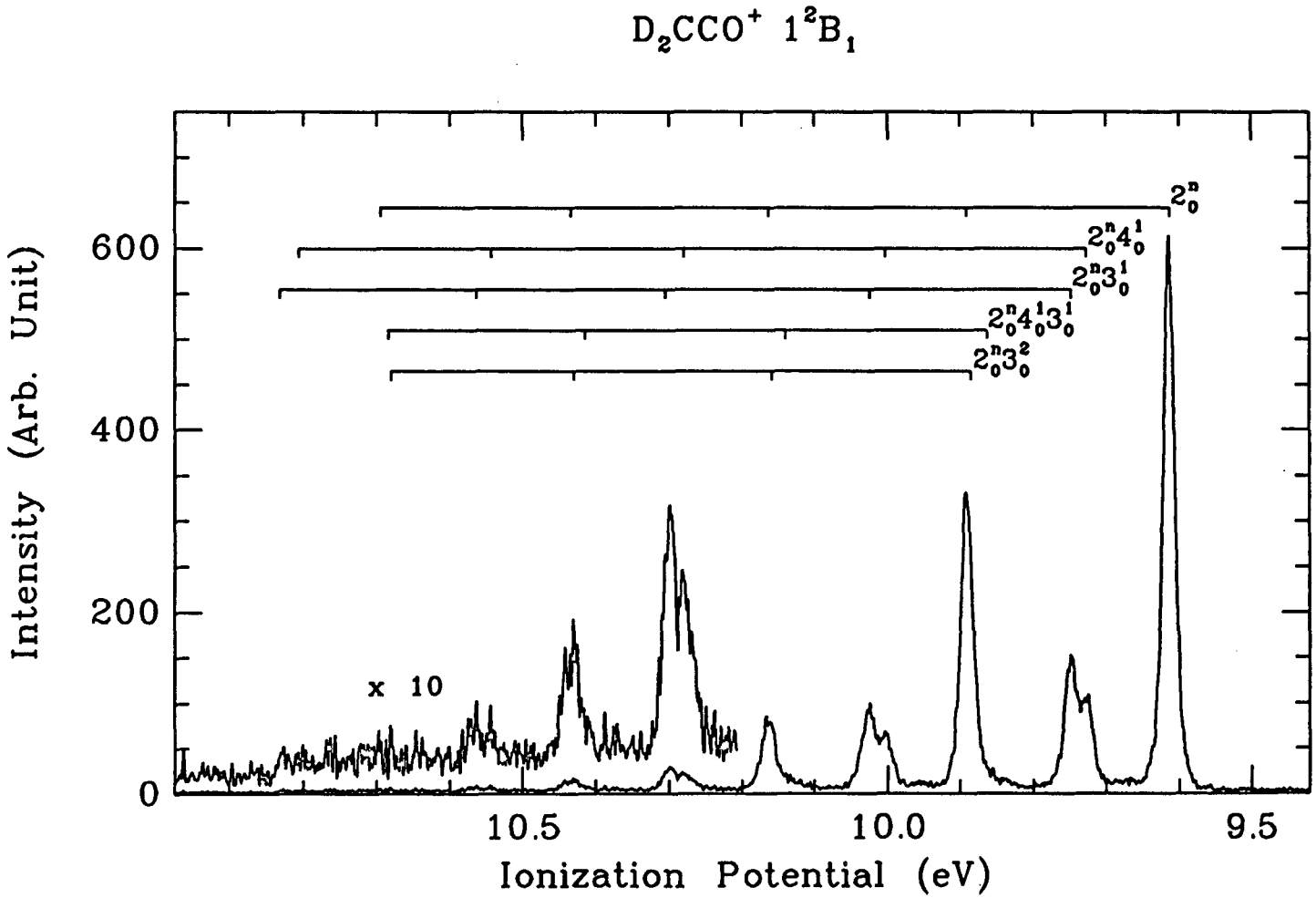
D_2CCO^+ 1^2B_1
Intensity (Arb. Unit)
600
400
200
0
x 10
2_0^n
$2_0^n4_0^1$
$2_0^n3_0^1$
$2_0^n4_0^13_0^1$
$2_0^n3_0^2$
10.5
10.0
9.5
Ionization Potential (eV)

Figure 4

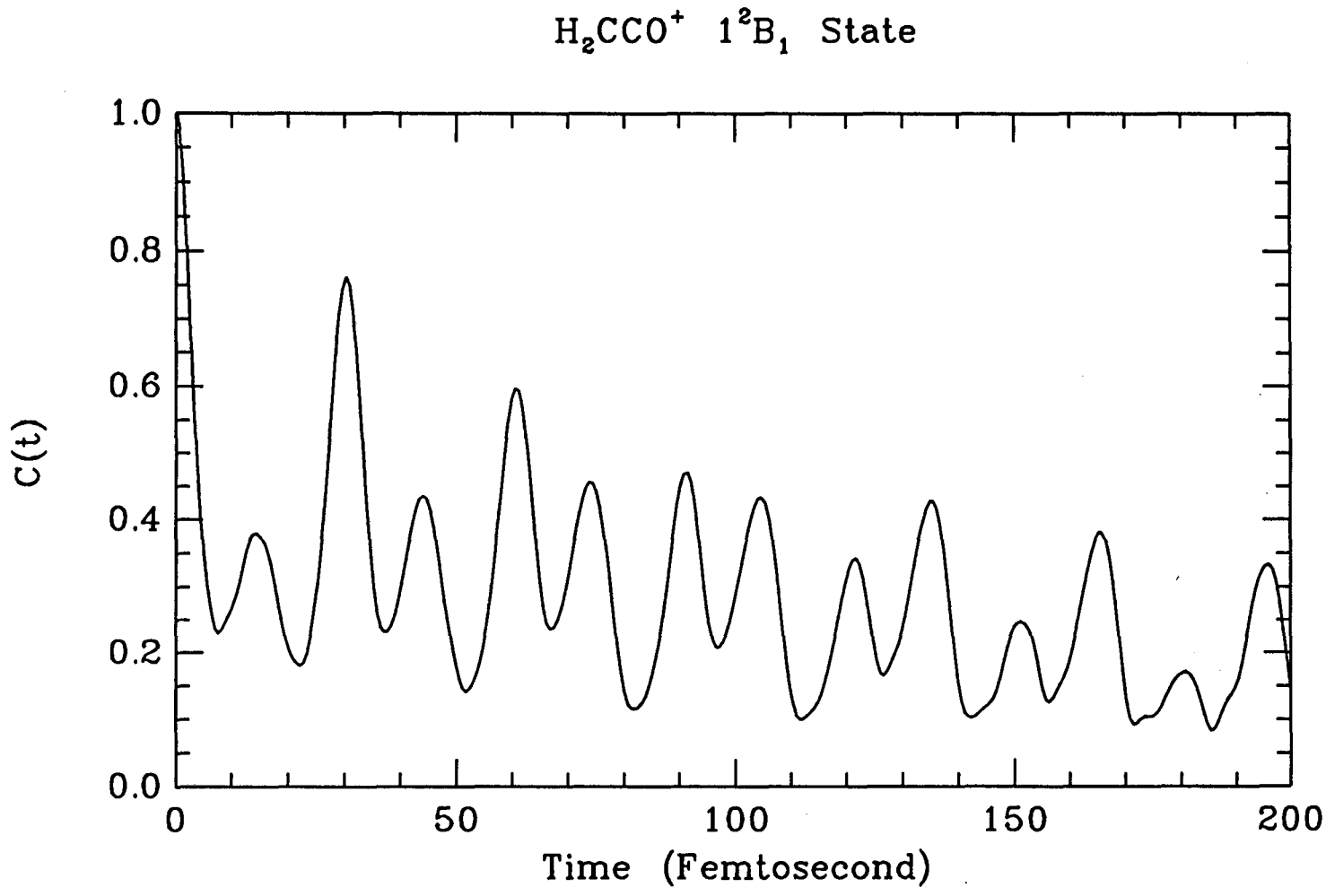
H_2CCO^+ 1^2B_1 State
1.0
0.8
0.6
0.4
0.2
0.0
C(t)
0
50
100
150
200
Time (Femtosecond)

Figure 5

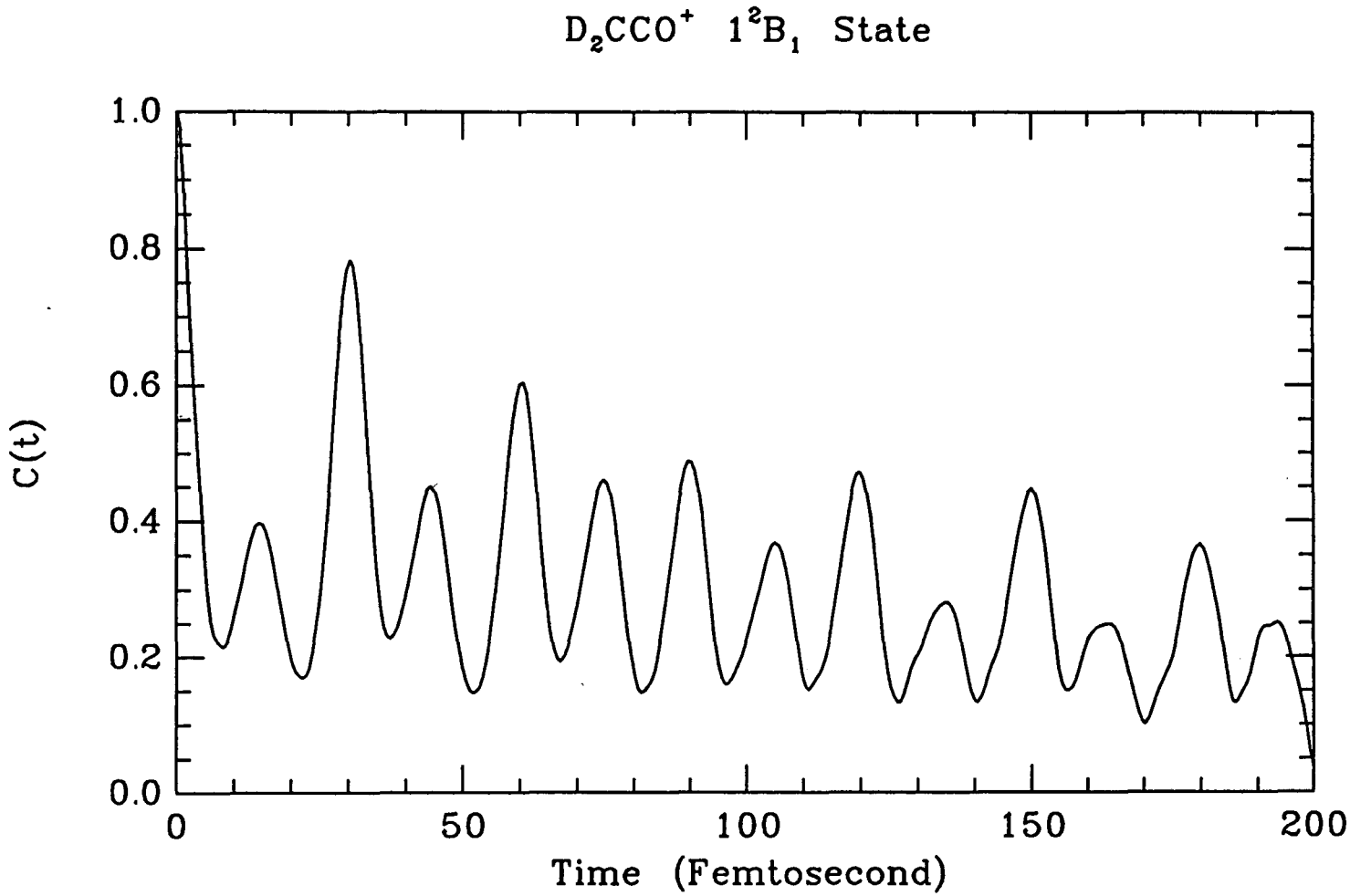
D_2CCO^+ 1^2B_1 State
1.0
0.8
0.6
0.4
0.2
0.0
C(t)
0
50
100
150
200
Time (Femtosecond)

Figure 6

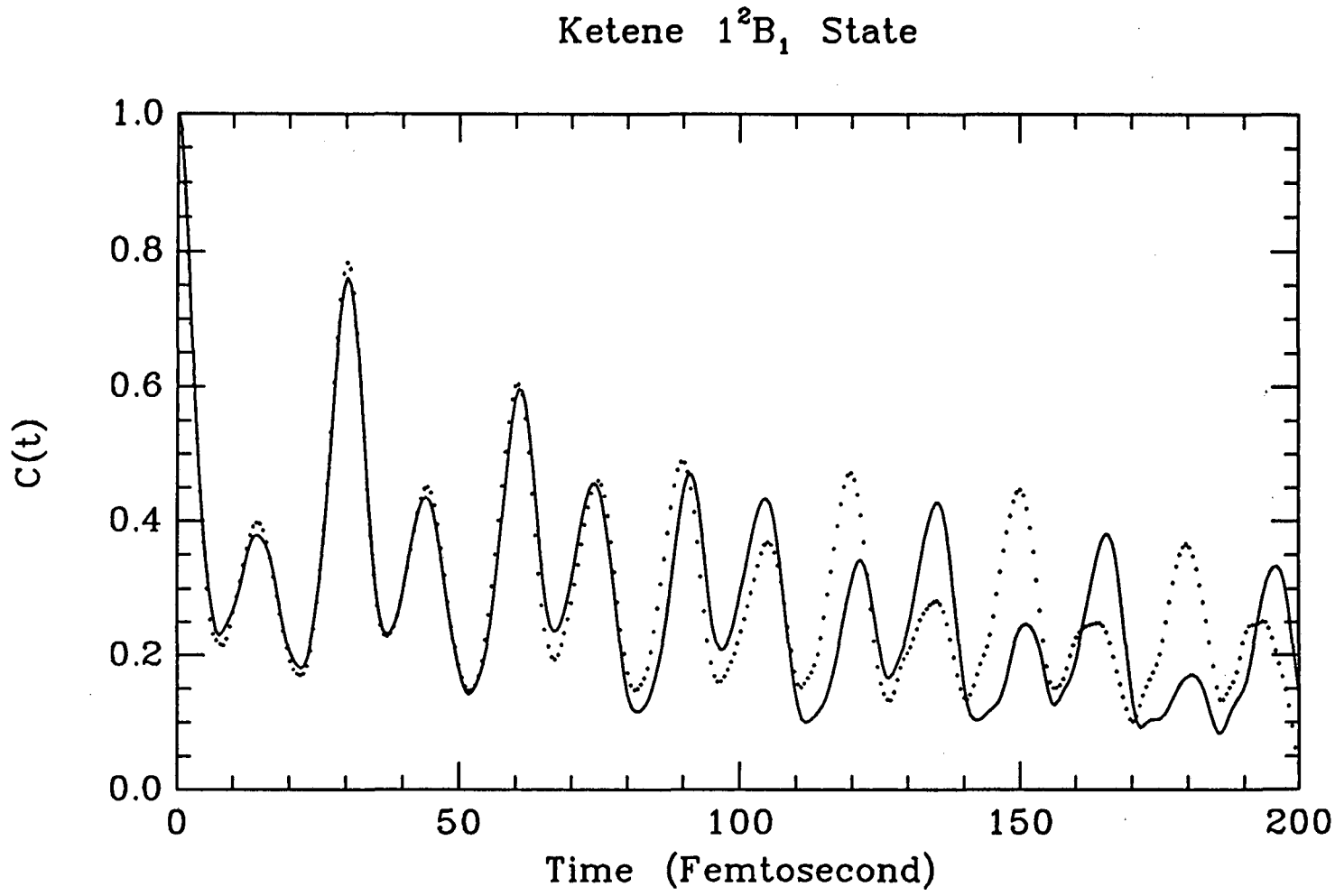
Ketene 1^2B_1 State
1.0
0.8
0.6
0.4
0.2
0.0
C(t)
0
50
100
150
200
Time (Femtosecond)

Figure 7

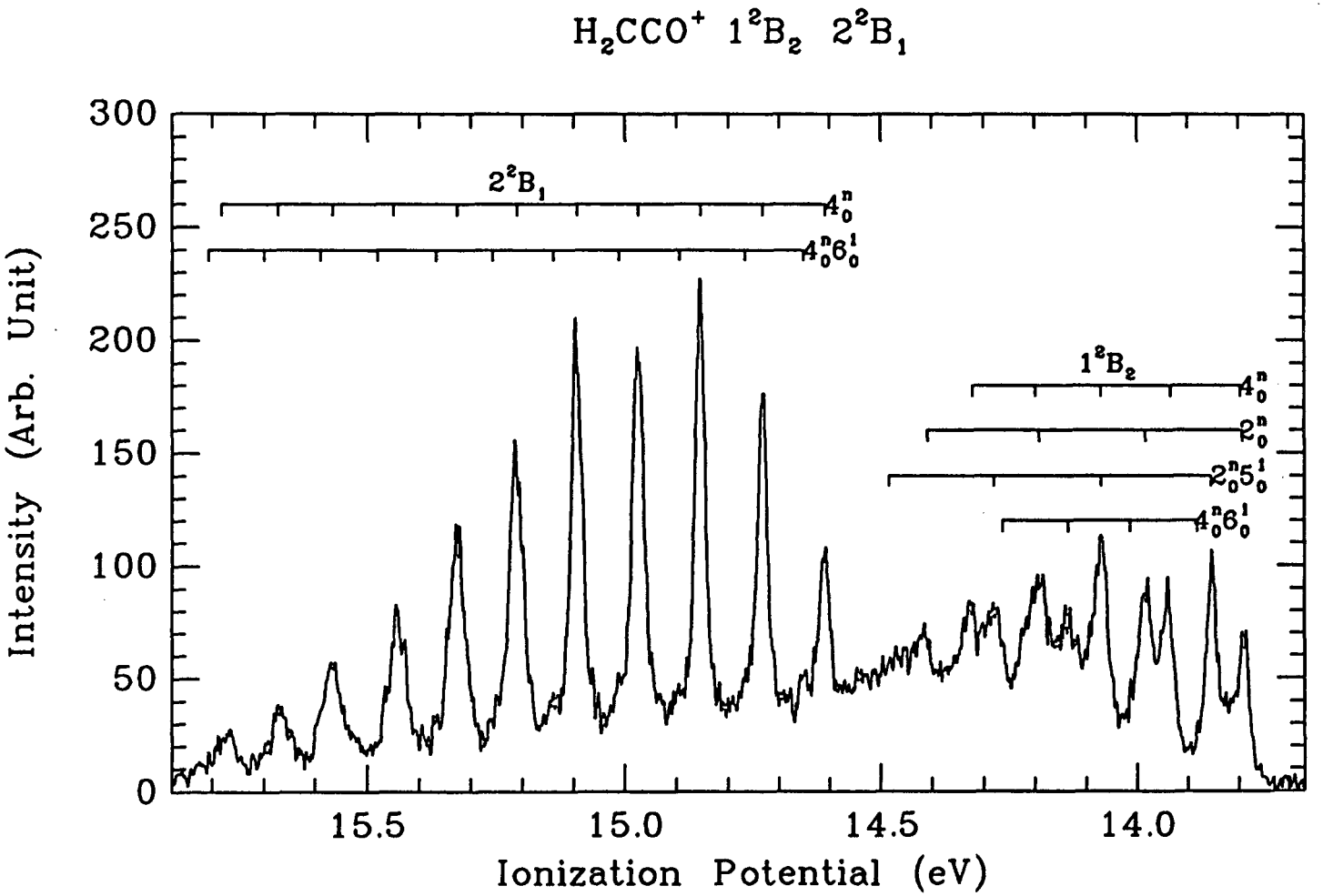
H_2CCO^+ 1^2B_2 2^2B_1
2^2B_1
4_0^n
$4_0^n6_0^1$
1^2B_2
4_0^n
2_0^n
$2_0^n5_0^1$
$4_0^n6_0^1$
Intensity (Arb. Unit)
300
250
200
150
100
50
0
15.5
15.0
14.5
14.0
Ionization Potential (eV)

Figure 8

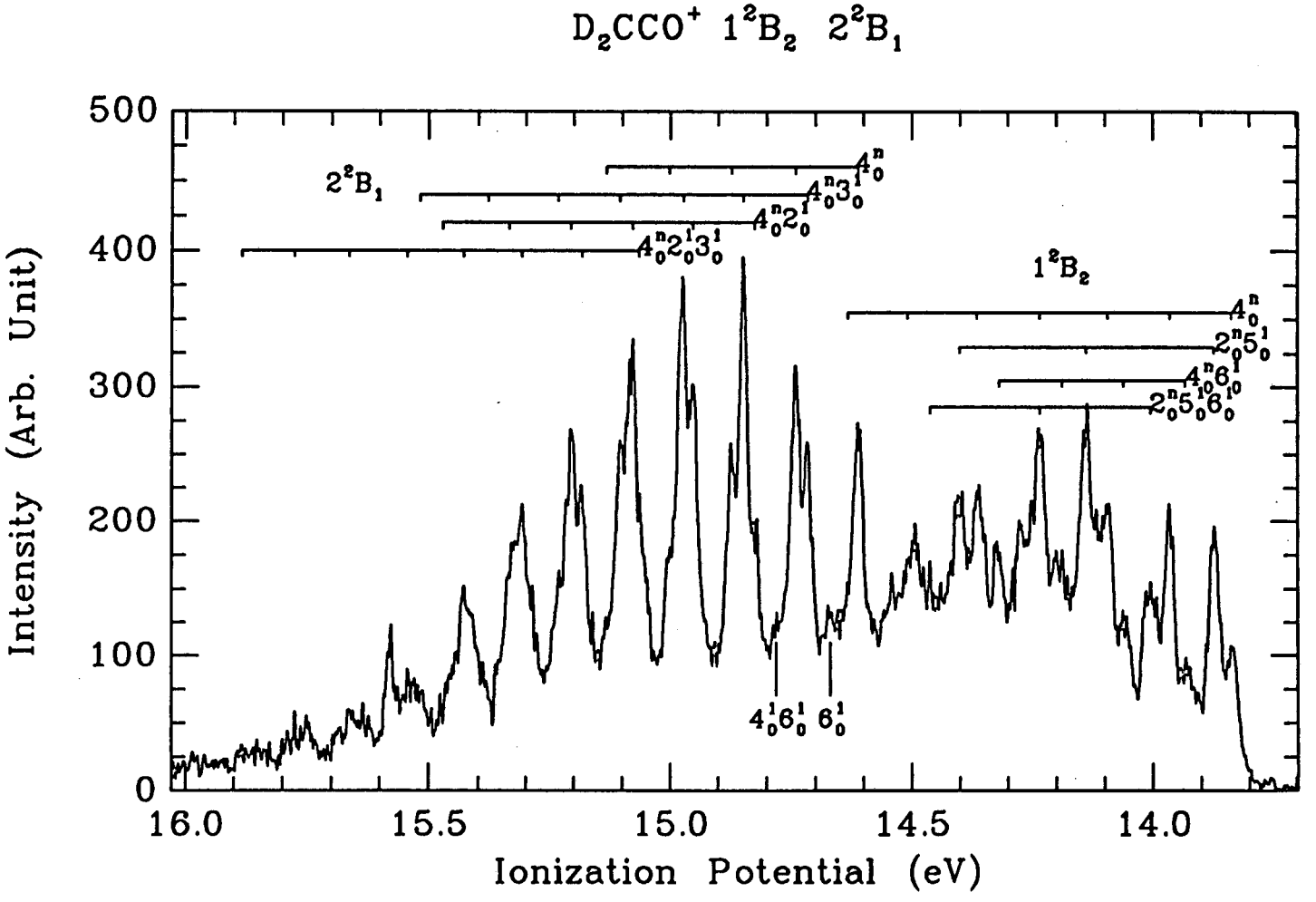
D2CCO+ 1²B2 2²B1
Intensity (Arb. Unit)
Ionization Potential (eV)
500
400
300
200
100
0
16.0
15.5
15.0
14.5
14.0
2²B1
1²B2
4⁰ⁿ
4⁰ⁿ3⁰¹
4⁰ⁿ2⁰¹
4⁰ⁿ2⁰¹3⁰¹
4⁰ⁿ
2⁰ⁿ5⁰¹
4⁰ⁿ6⁰¹
2⁰ⁿ5⁰¹6⁰¹
4⁰¹6⁰¹ 6⁰¹

Figure 9

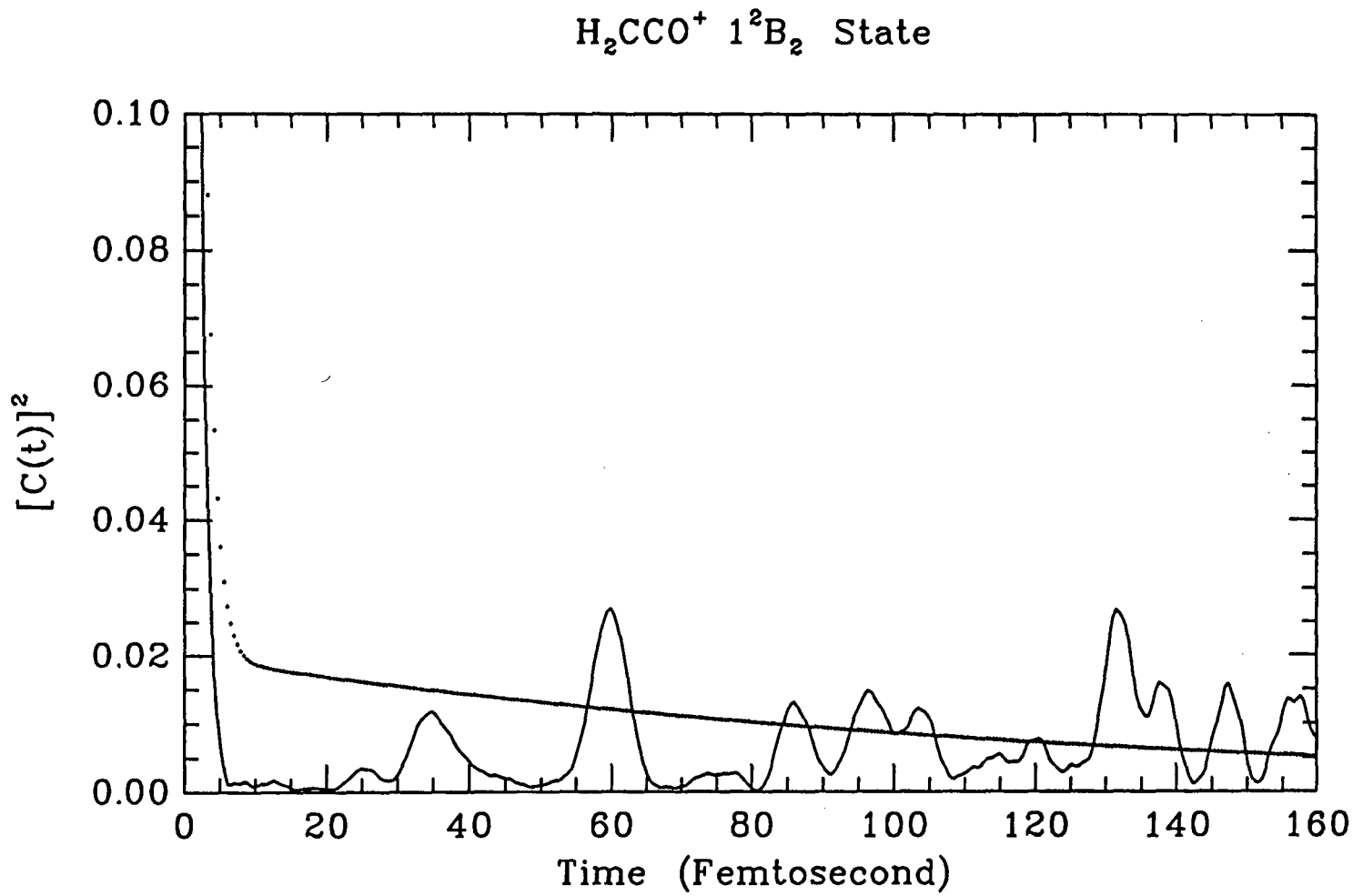
H_2CCO^+ 1^2B_2 State
0.10
0.08
0.06
0.04
0.02
0.00
$[C(t)]^2$
0
20
40
60
80
100
120
140
160
Time (Femtosecond)

Figure 10

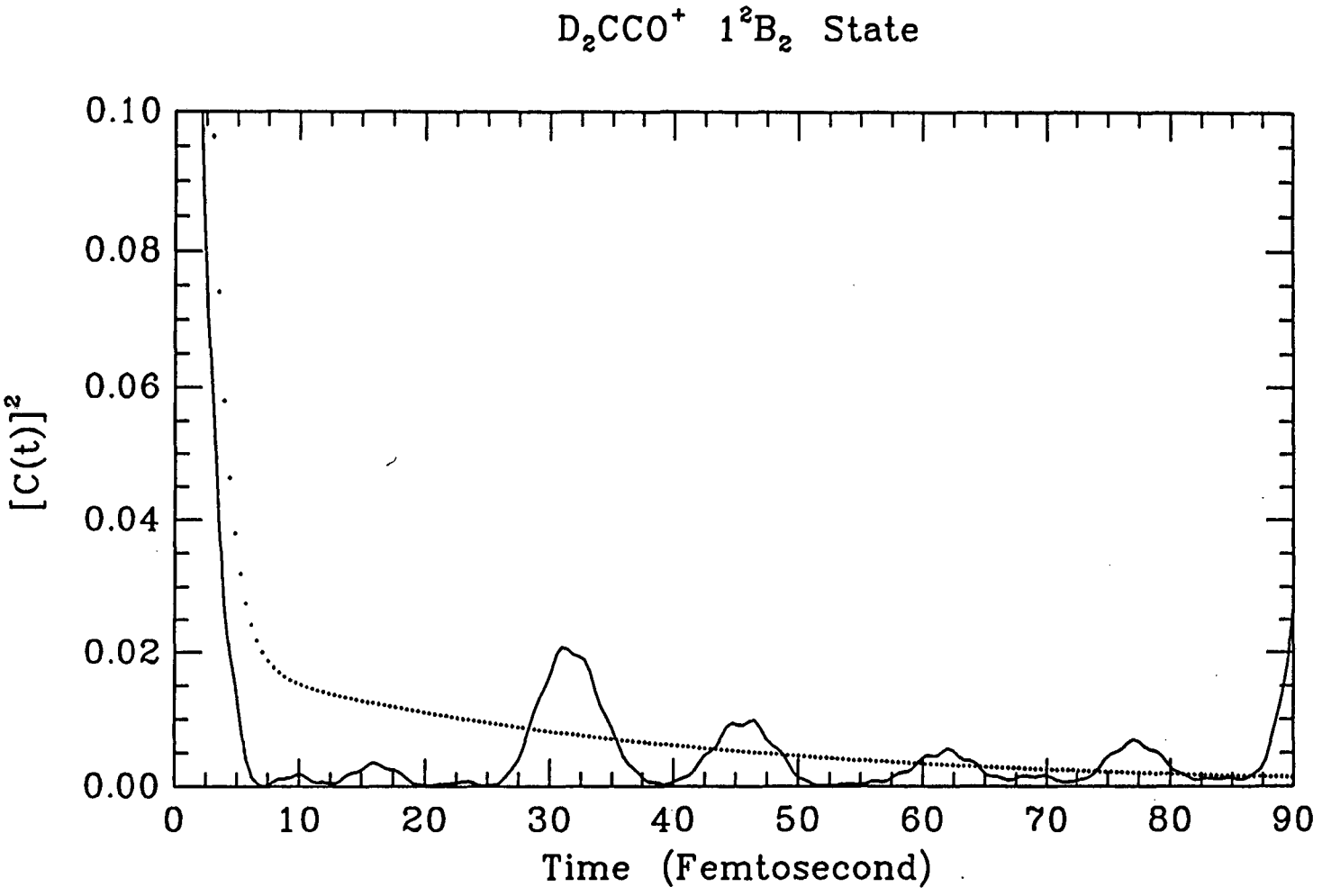
D_2CCO^+ 1^2B_2 State
0.10
0.08
0.06
0.04
0.02
0.00
$[C(t)]^2$
0
10
20
30
40
50
60
70
80
90
Time (Femtosecond)

Figure 11

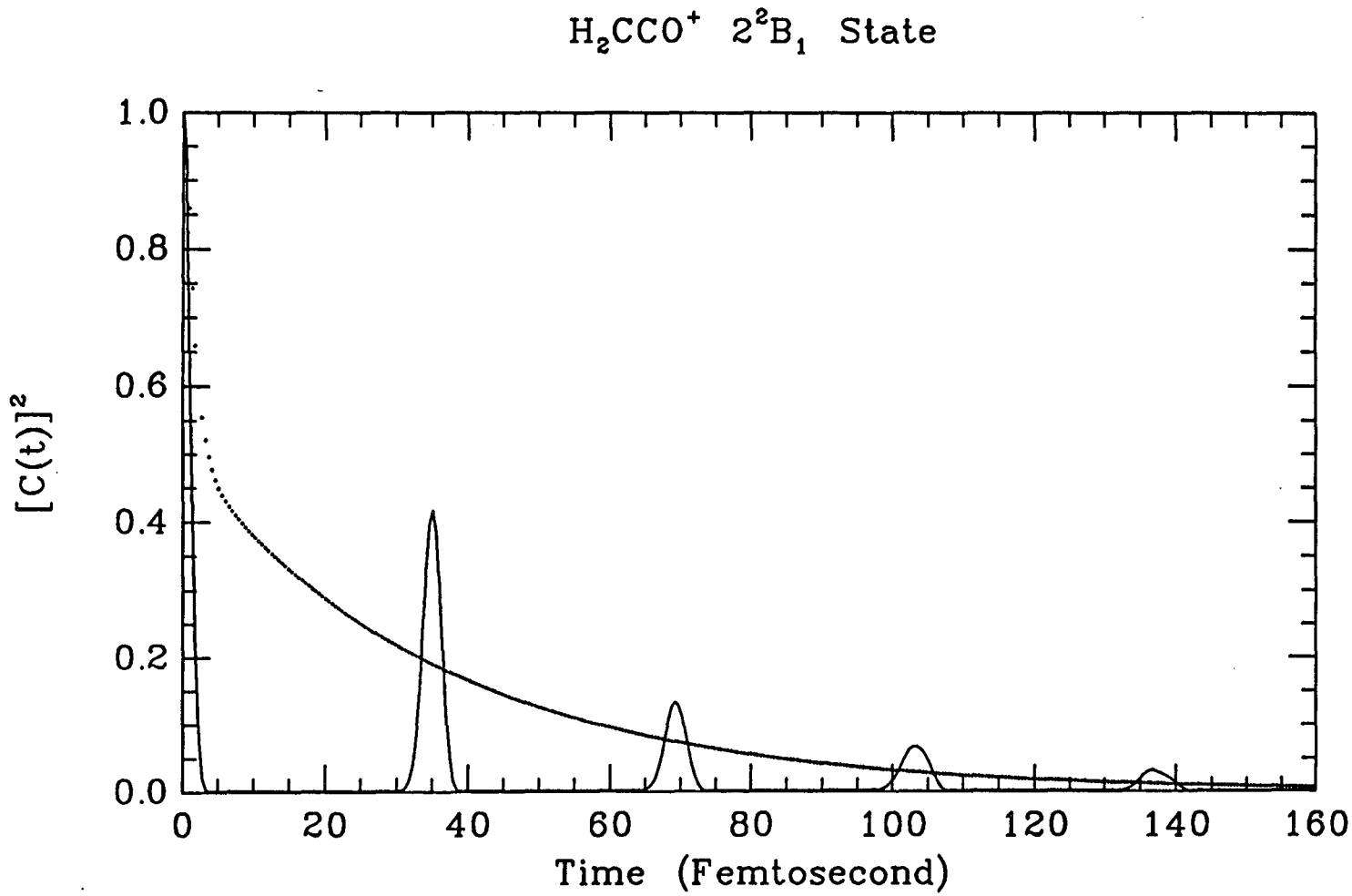
H_2CCO^+ 2^2B_1 State
1.0
0.8
0.6
0.4
0.2
0.0
$[C(t)]^2$
0
20
40
60
80
100
120
140
160
Time (Femtosecond)

Figure 12

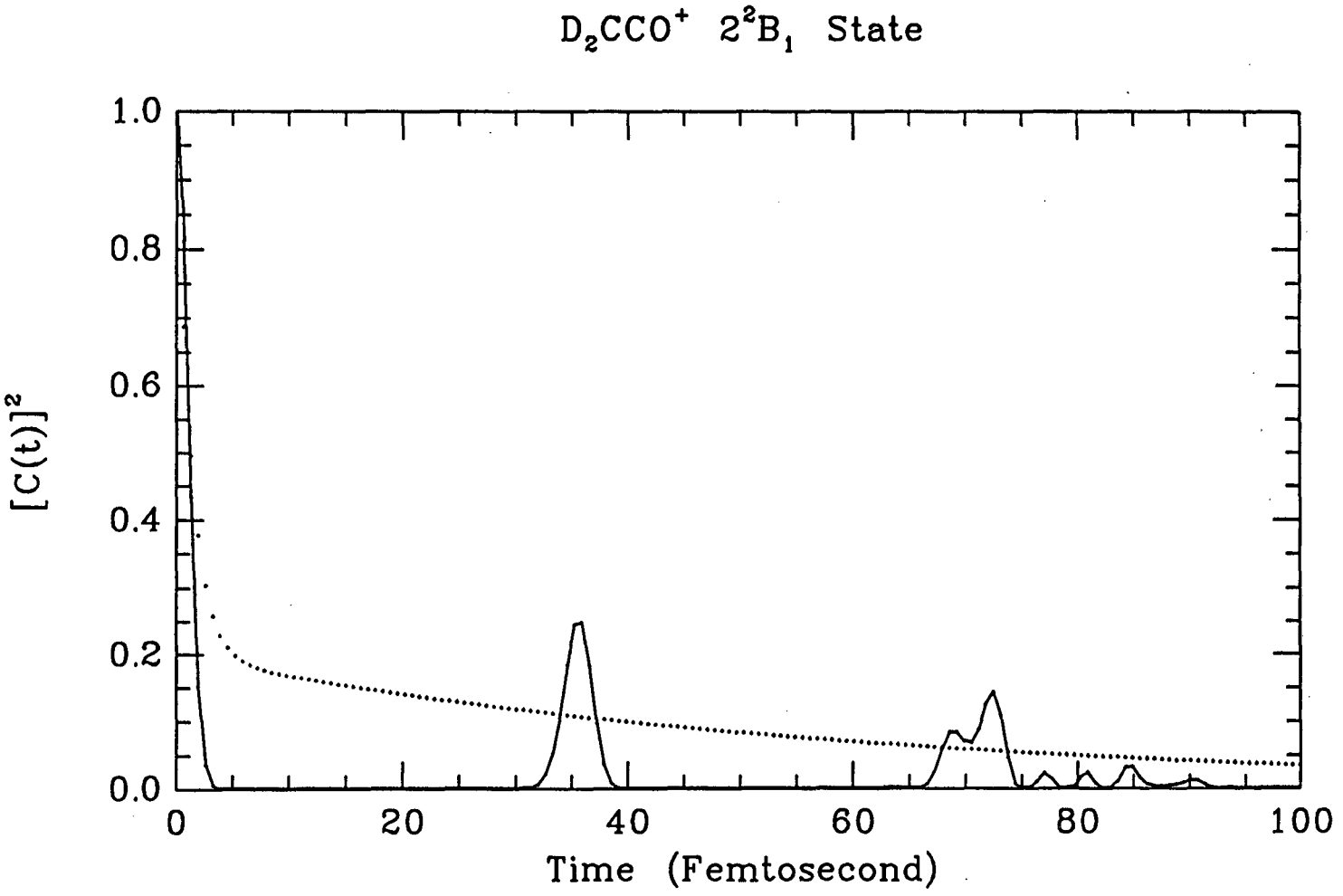
D_2CCO^+ 2^2B_1 State
1.0
0.8
0.6
0.4
0.2
0.0
$[C(t)]^2$
0
20
40
60
80
100
Time (Femtosecond)

Figure 13

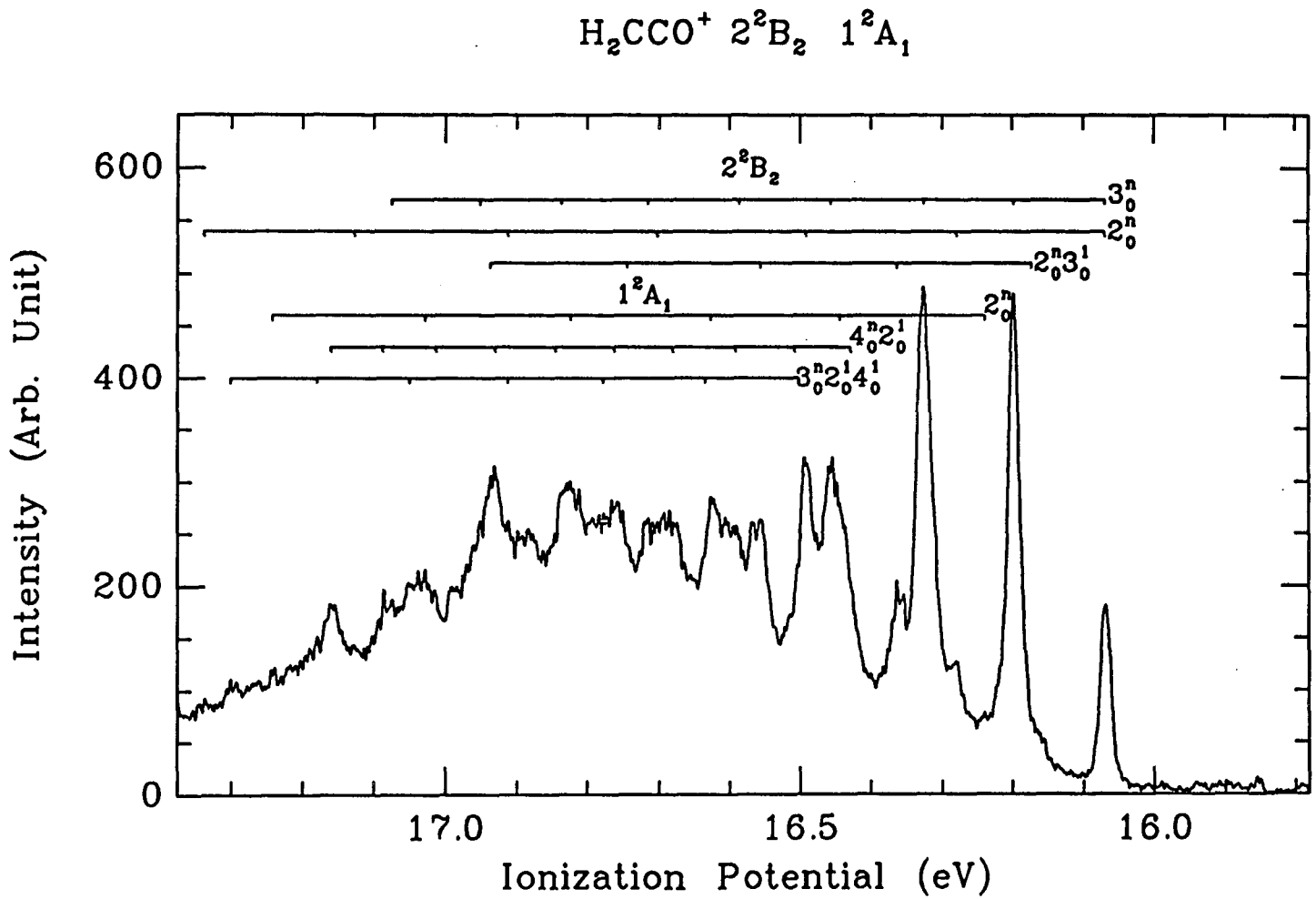
H_2CCO^+ 2^2B_2 1^2A_1
2^2B_2
3_0^n
2_0^n
$2_0^n3_0^1$
1^2A_1
2_0^n
$4_0^n2_0^1$
$3_0^n2_0^14_0^1$
600
400
200
0
17.0
16.5
16.0
Intensity (Arb. Unit)
Ionization Potential (eV)

Figure 14

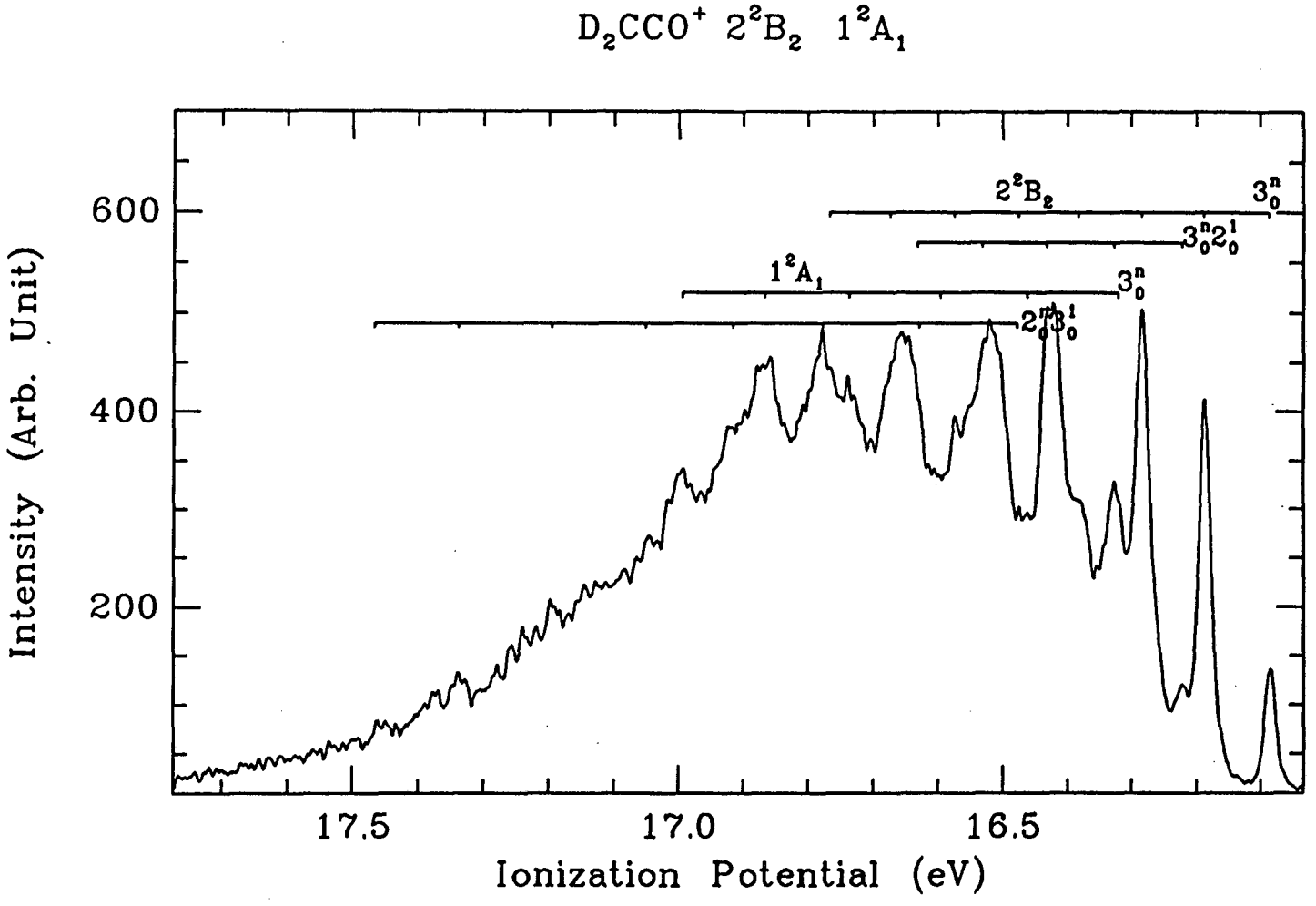
D2CCO+ 2²B2 1²A1
Intensity (Arb. Unit)
600
400
200
17.5
17.0
16.5
Ionization Potential (eV)
2²B2
3ⁿ0
3ⁿ0 2¹0
1²A1
3ⁿ0
2ⁿ0 3¹0

Figure 15

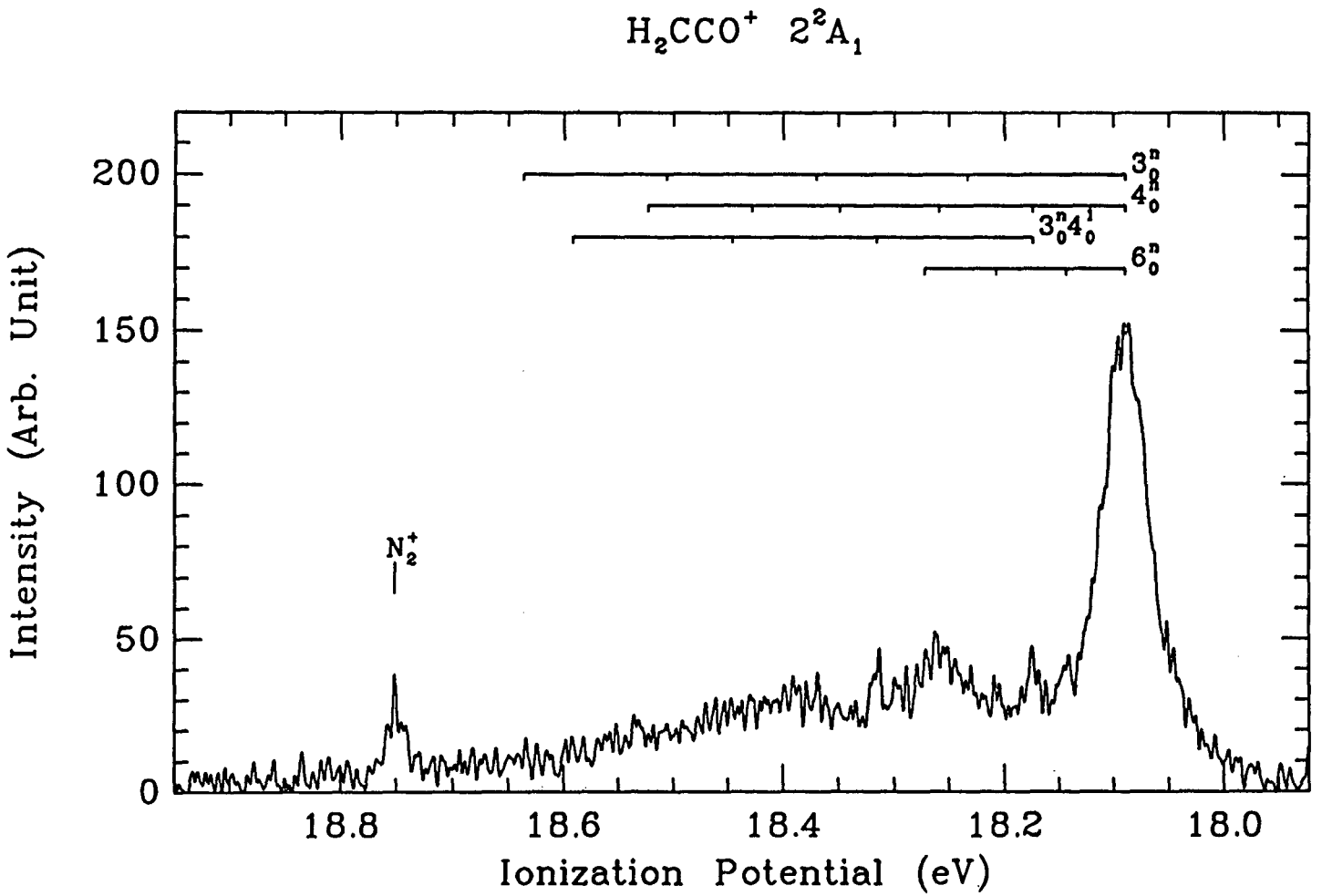
H_2CCO^+ 2^2A_1
Intensity (Arb. Unit)
200
150
100
50
0
18.8
18.6
18.4
18.2
18.0
Ionization Potential (eV)
N_2^+
3_0^n
4_0^n
$3_0^n4_0^1$
6_0^n

Figure 16

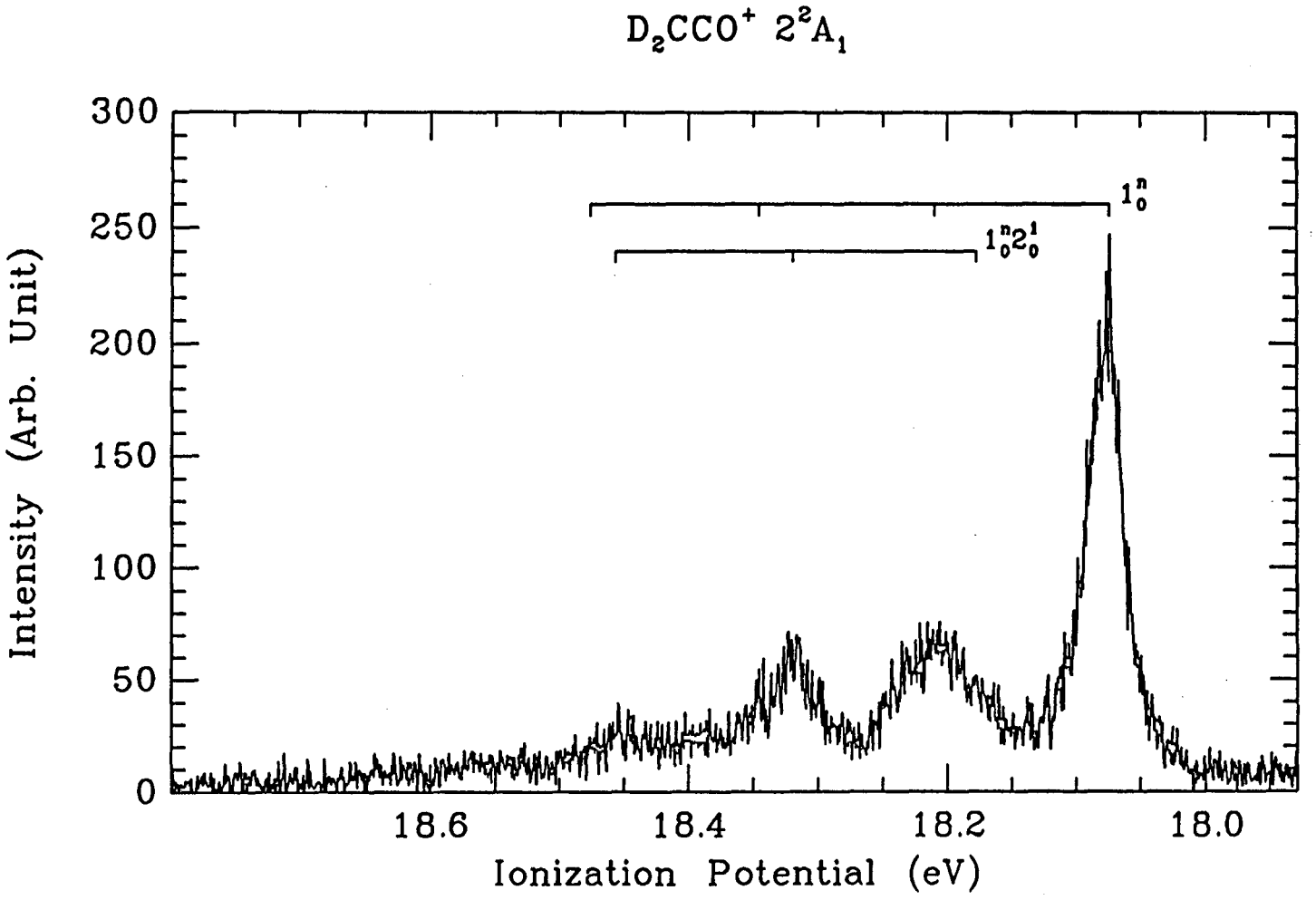
D_2CCO^+ 2^2A_1
300
250
200
150
100
50
0
Intensity (Arb. Unit)
1_0^n
$1_0^n 2_0^1$
18.6
18.4
18.2
18.0
Ionization Potential (eV)

Figure 17

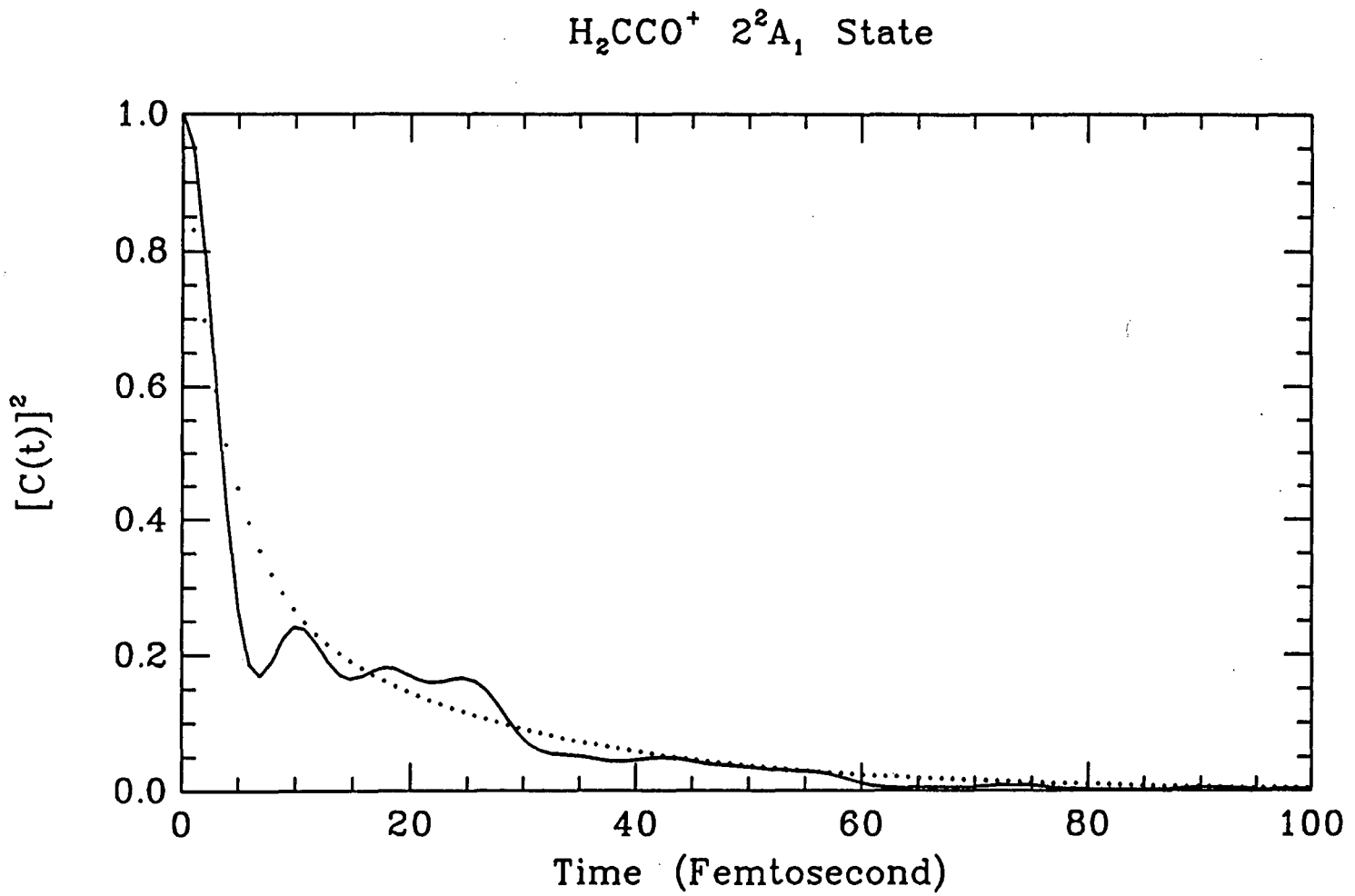
H_2CCO^+ 2^2A_1 State
1.0
0.8
0.6
0.4
0.2
0.0
$[c(t)]^2$
0
20
40
60
80
100
Time (Femtosecond)

Figure 18

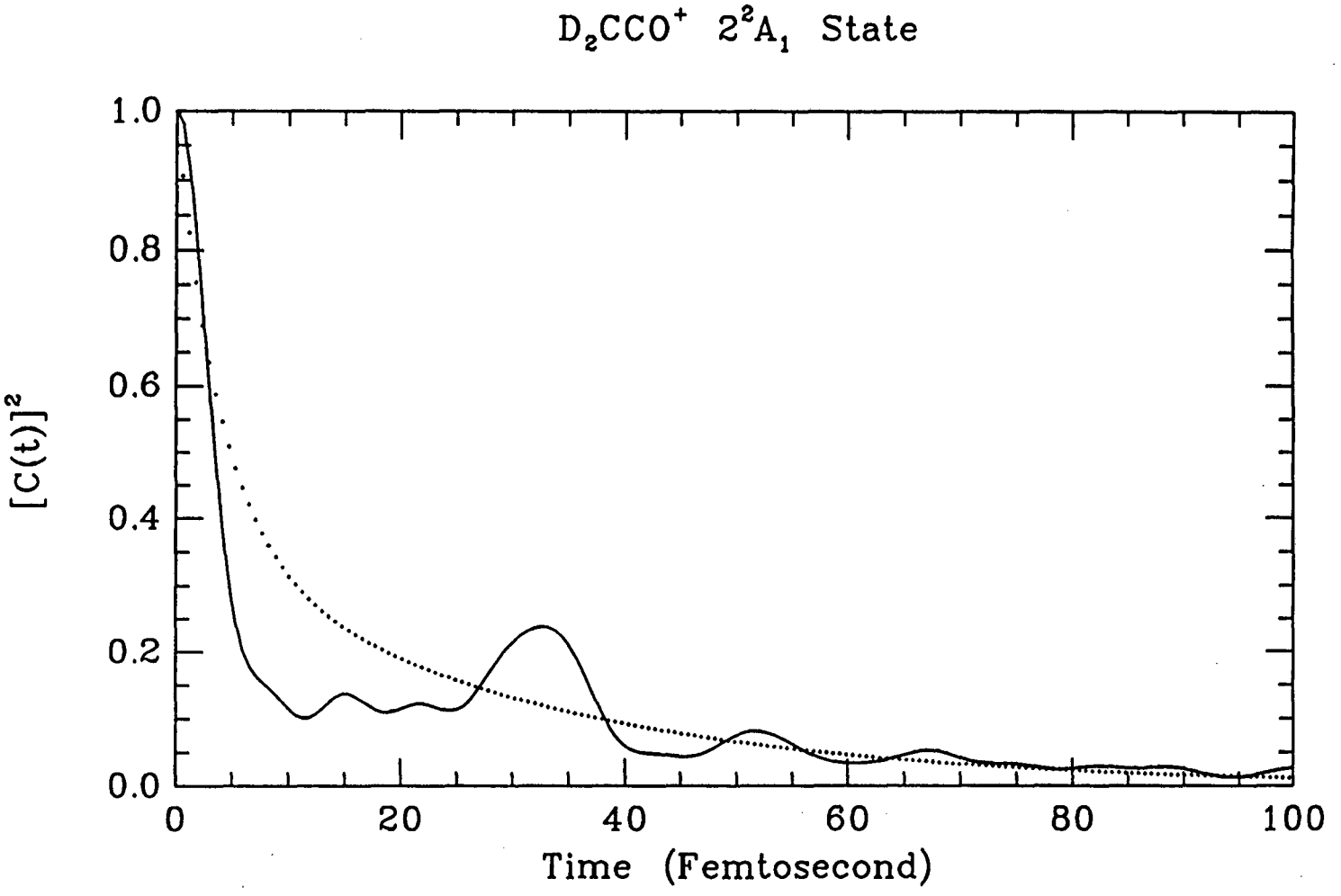
D_2CCO^+ 2^2A_1 State
1.0
0.8
0.6
0.4
0.2
0.0
$[C(t)]^2$
0
20
40
60
80
100
Time (Femtosecond)

Figure 19

Chapter Five: Conclusions, and the Future of Photoelectron Spectroscopy

The electronic structure, spectroscopy and the decay dynamics of polyatomic molecules have proved to be an exciting, ever-growing field where much unknown remains unchallenged even today. The photoelectron spectroscopy and intramolecular dynamics of the two systems studied in this dissertation have shown the rich information we can get from such studies.

The high-resolution spectra reported have resolved some long-standing controversies on the electronic structure of the formaldehyde and ketene cations. In the case of formaldehyde, we have shown positively with experimental evidence that formaldehyde cations in their ground and the first excited states might have non-planar equilibrium geometries. The fine structures on the first excited state of formaldehyde are fully resolved here for the first time. Theoretical works have long predicted that vibronic (vibrational) coupling can be very different for isotopic compounds in the same electronic state. This effect increased the difficulty substantially in the assignment of spectra even with the aid of isotope substitution. We have observed strong isotope effects on the vibronic (vibrational) coupling experimentally. In the second excited state of formaldehyde, very different vibrational progressions are observed for isotopic compounds. We hope the experimental work reported will stimulate much more work on the theoretical front to further our understanding of vibronic couplings and their effects on the spectroscopy and structures of molecules. The present study favors the many-body theoretical calculations that explain the experimentally observed spectra much better than the simple **Hartree-Fock** approach calculations. The vibrational autocorrelation function calculated from the photoelectron spectrum of the first excited state of formaldehyde decays rather slowly compared with the molecular vibrational motion. The decay of the first

excited state of formaldehyde cation thus may not be as simple as we previously thought. The third excited state of formaldehyde cation, on the other hand, decays extremely fast indicating that unimolecular dissociation and other ultrafast intramolecular processes are the main decay pathways.

The photoelectron spectroscopy and intramolecular dynamic studies reported have shed considerable light on the structure and decay dynamics of ketene cations. The high resolution achieved, coupled with very effective rotational cooling by supersonic expansion revealed much more vibrational structure detail in the ground and the first excited states than previously observed. Here, again, the vibrational couplings are different in the isotopic compounds, as is apparent in the present spectra. The **AIEs** of the first and the fifth electronic states are determined unambigously to a much higher accuracy than previously possible. The excitation of a 'soft' mode in the first excited state of ketene cations complicated considerably the complexity of the photoelectron spectrum of this band. Resolving this 'soft' mode here for the first time gives future theoretical work much needed experimental information on this state that will elucidate some of the controversies surrounding this state. The analysis given support this state is predissociative in the **Franck-Condon** part of the upper potential energy surface, which is characterized by the extremely fast decay of the vibrational autocorrelation function calculated from the photoelectron spectrum. The autocorrelation functions calculated for the grounds state of ketene cations shows essentially an undisplaced wavepacket that oscillates with samll amplitude around the minimum of the upper potential energy surface, retaining high levels of correlation strength at all times. The correlation functions calculated for the fifth excited state shows ultra fast decay on the time scale of a few femtoseconds. This, together with the broad peak shapes and very short vibrational progressions observed in the photoelectron spectrum of this band, implies that this state is dissociative in the **Franck-**

Condon region. The intramolecular dynamics of the ketene cations have received relatively little attention previously. The autocorrelation functions calculated can only be regarded as the very beginning of our detailed studies on the intramolecular dynamics of systems with such complexity as ketene cations.

This dissertation also aroused some interesting questions about the structure, spectroscopy and dynamics of the polyatomic molecules that need to be addressed in future theoretical and experimental works. A perspective is in order here. The high resolution achieved and the effectively rotational cooling offered by the MBPES machine are remarkable in many aspects. The coupling of a supersonic beam with the a unique double pass high resolution electron-energy analyzer is essential for this success. However, there are improvements that can be made to enhance substantially the performance of the apparatus. The first one will be the light source. The helium discharge lamp used has been optimized to produce intense, highly monochromatized light. The limit of the helium lamp was evident also. The linewidth was about 2 meV. Any efforts to improve the resolution of the analyzer must improve the performance of the light source first. In this regard, the fast advancing VUV lasers and synchrotron light source should be the primary sources for future high-resolution work. The second aspect is the electron-energy analyzer. The present analyzer succeeds fairly well around 10 meV resolution. The state of the art in electron-energy analyzer (excluding those time-of-flight types) performance is around 1 meV resolution. Thus there is room in improving the performance of the analyzer itself. We believe this can be achieved with a larger hemispherical analyzer operating in the low-pass energy range (2-5 eV). The magnetic shielding problem can be essentially eliminated by careful designing the μ-metal magnetic shielding with as few openings as possible. The magnetic shielding of the MBPES has proved to be very effective in getting the high resolution desired. The residual magnetic field inside the analyzer chamber was measured

to be ~ 5 mGauss which was largely attributed to the field penetration through openings in the μ-metal, and this can be further reduced to less than 1 mGauss without much difficulty. The distance over which electrons travel from the ionization region to the analyzer was almost 100 cm. This was dictated by the requirements of varying the pass energy and installing the prefilter to reduce stray electrons. In practice, the analyzer was operated at fixed pass energy exclusively. Fixed pass energy requires much less sophistication in the design of the lens system, and reduces the length of the lens stacks considerably. If effective pumping of the main chamber can be achieved with better beam catching in the exhaust chamber, the stray electron problem can be minimized. This will simplify considerably the design of the lens system and the μ-metal magnetic shielding. The 8:1 deceleration lens voltages have deviated substantially from the theoretical calculated values. The cause of this deviation was not clear. This affects the stability and the resolution achievable considerably. We believe that a real aperture at the virtual entrance will help stabilize the operation and improve the resolution of the apparatus with little inconvenience. In fact, the best resolution was obtained when we had a real aperture at the virtual entrance of the hemispherical analyzer. Also, it was discovered that the multichannel detector's actually usable area was only about half the active area. This is caused most probably by the stray field and improper termination of the electric field. In this regard, better field termination will increase the detection efficiency considerably. With these improvements, the new generation of MBPES should be operative with resolution in the a few meV ranges just as the present MBPES did in the ~ 10 meV range. The current MBPES apparatus has no trap for the diffusion pump of the beam source, and no isolation valve exists between the beam source and the main chamber. This causes contamination of the main chamber and frequent venting of the analyzer chamber. If a trap can be installed on the beam source diffusion pump, this will reduce considerably the possibilities of contaminating the main chamber.

However, the ultimate resolution achievable in photoelectron spectroscopy depends on the light source linewidth more than the resolution of the analyzer. With the advance of threshold analyzer (time-of-flight) combined with the resolving powers offered by VUV lasers and modern synchrotron radiation source, like the advanced light source now under construction at Lawrence Berkeley Laboratory, photoelectron spectroscopy will eventually have the resolution now enjoyed by optical spectroscopy. This will enable us to study the details of electronic structures, spectroscopy and dynamics of molecular cations in the near future. Rotationally resolved photoelectron spectroscopy is the ultimate goal in this regard, and it is not far from realization.

LAWRENCE BERKELEY LABORATORY
UNIVERSITY OF CALIFORNIA
TECHNICAL INFORMATION DEPARTMENT
BERKELEY, CALIFORNIA 94720